UNIVERSIDADE DE SÃO PAULO
FFCLRP - DEPARTAMENTO DE FÍSICA
PÓS-GRADUAÇÃO EM FÍSICA APLICADA À MEDICINA E BIOLOGIA

ERNESTO EDGAR MAZÓN VALADEZ

Desenvolvimento de uma plataforma teranóstica automatizada combinando magnetoacustografia e hipertermia magnética

Development of an automated theranostic platform combining magnetomotive ultrasound and magnetic hyperthermia

Ribeirão Preto – SP
2023

ERNESTO EDGAR MAZÓN VALADEZ

Desenvolvimento de uma plataforma teranóstica automatizada combinando magnetoacustografia e hipertermia magnética

Development of an automated theranostic platform combining magnetomotive ultrasound and magnetic hyperthermia

Tese apresentada à Faculdade de Filosofia, Ciências e Letras da Universidade de São Paulo em Ribeirão Preto, como parte dos requisitos para a obtenção do título de Doutor em Ciências.

Área de concentração: Física Aplicada à Medicina e Biologia

Orientador: Prof. Dr. Theo Zeferino Pavan

Versão Original

Disponível na FFCLRP-USP

Ribeirão Preto – SP

2023

Mazón Valadez, Ernesto Edgar
Desenvolvimento de uma plataforma teranóstica automatizada combinando magnetoacustografia e hipertermia magnética/ Ernesto Edgar Mazón Valadez; Orientador: Prof. Dr. Theo Zeferino Pavan. Ribeirão Preto - SP, 2023.
93 P.
Tese (Doutorado - Programa de Pós-Graduação em Física Aplicada à Medicina e Biologia) - Faculdade de Filosofia, Ciências e Letras de Ribeirão Preto, Universidade de São Paulo, 2023.

1. Plataforma teranóstica 2. Hipertermia magnética 3. Magnetoacustografia 4. Nanopartícula magnética 5. Ultrassom.

FICHA CATALOGRÁFICA

Name: Ernesto Edgar Mazón Valadez

Title: Development of an automated theranostic platform combining magnetomotive ultrasound and magnetic hyperthermia.

Thesis presented to the Faculty of Philosophy, Sciences, and Literature of the University of São Paulo, as part of the requirements for the degree of Doctor of Sciences.

Approved in: ___/___/___.

Examination Board

Prof. Dr.: _____, Institution: _____

Judgment: _____, Signature: _____

Prof. Dr.: _____, Institution: _____

Judgment: _____, Signature: _____

Prof. Dr.: _____, Institution: _____

Judgment: _____, Signature: _____

Prof. Dr.: _____, Institution: _____

Judgment: _____, Signature: _____

Acknowledgments

I want to express my heartfelt appreciation and gratitude to my parents and brothers for their unwavering support and encouragement throughout this journey. Their belief in me has been a constant source of motivation. I am incredibly fortunate to have a loving and supportive wife by my side. Her unconditional love has inspired me, and her unwavering support has fueled my determination to succeed. To my dear friends, thank you for your companionship and understanding. Your presence has provided much-needed solace during challenging times.

I want to express my sincere gratitude to Prof. Dr. Theo Zeferino Pavan for graciously opening the doors of his laboratory to me four years ago when I embarked on my scientific journey in Brazil. I am deeply grateful for the invaluable teachings, unwavering support, and genuine care he has extended me throughout these years. His mentorship has played a pivotal role in shaping my professional growth, and I genuinely appreciate his significant contribution to my development.

I would also like to extend my heartfelt thanks to Prof. Dr. Antonio A. O. Carneiro for his invaluable guidance during my doctorate. His expertise and insights have been instrumental in shaping my research trajectory, and I am immensely grateful for his mentorship and support.

Additionally, I would like to thank the laboratory technicians for their willingness to assist me whenever I needed their help. Their expertise and dedication have been invaluable in facilitating my experiments and ensuring the smooth progress of my work.

I am truly fortunate to have had the opportunity to work alongside such exceptional individuals. Their support, guidance, and dedication have been fundamental to my academic and professional accomplishments. I am forever grateful for their contributions to my journey.

I acknowledge the financial support of CAPES (scholarship), CNPq, FAPESP, and Universidad de Guadalajara.

Resumo

Abordagens teranósticas, que combinam modalidades diagnósticas e terapêuticas, estão ganhando reconhecimento como um método inovador para aumentar a eficácia de tratamentos médicos. Uma técnica específica nesse campo é a hipertermia magnética (MH), que utiliza campos magnéticos de alta frequência e nanopartículas magnéticas (MNPs) para direcionar e aquecer células cancerígenas. No entanto, o monitoramento em tempo real da temperatura e da localização de MNPs durante a terapia de MH in vivo apresenta desafios significativos. A magnetoacustografia (MMUS) tem mostrado bom potencial para localizar MNPs e, assim, aprimorar o processo de MH. No entanto, um grande desafio é a implementação da alternância automatizada entre os campos magnéticos necessários para MMUS e MH usando uma única bobina de excitação. Esse desafio surge devido aos diferentes requisitos de frequência, com MH operando na faixa de 100-500 kHz e MMUS exigindo campos magnéticos de frequência mais baixa (<100 Hz). Portanto, o objetivo desta pesquisa foi desenvolver uma plataforma teranóstica capaz de operar simultaneamente MH e MMUS usando uma única bobina de excitação, possibilitando o uso em tempo real. Superar esse desafio tecnológico envolveu a utilização de acoplamento eletromagnético. Para gerar imagens de MMUS, um gerador de pulso baseado em um circuito de descarga de capacitor-bobina foi desenvolvido e incorporado à plataforma teranóstica. O sistema integrado utilizou um indutor para gerar pulsos de campo magnético de até 258 mT (2,16 kA). Os deslocamentos induzidos exibiram uma correlação direta com a variação de temperatura durante um procedimento de MH. Além disso, o sistema de MH desenvolvido alcançou um aumento de temperatura de 8 °C ao empregar um campo magnético de 15 kA/m para aquecer volumes maiores que 1 cm^3, indicando seu potencial para uma terapia de MH eficaz. Os resultados obtidos durante esta pesquisa são importantes para compreender as configurações ideais da plataforma teranóstica e orientar estudos futuros *in vivo* e *in vitro*.

Abstract

Theranostic approaches, combining diagnostic and therapeutic modalities, are gaining recognition as an innovative method to enhance the effectiveness of medical treatments. One specific technique in this field is magnetic hyperthermia (MH), which uses high-frequency magnetic fields and magnetic nanoparticles (MNPs) to target and heat cancerous cells. However, real-time tracking of temperature and MNP location during MH therapy in-vivo presents significant challenges. Magnetomotive ultrasound (MMUS) shows potential in locating MNPs; therefore, enhancing the MH process. However, a major challenge is the implementation of automated switching between the magnetic fields required for MMUS and MH using a single excitation coil. This challenge arises from the different frequency requirements, with MH operating within a 100-500 kHz range and MMUS demanding lower frequency magnetic fields (<100 Hz). Therefore, the goal of this research was to develop a theranostic platform capable of simultaneous MH and MMUS operation using a single excitation coil, enabling potential real-time usage. Overcoming this technological challenge involved the utilization of electromagnetic coupling. To generate MMUS images, a pulse generator based on a capacitor-coil discharge circuit was developed and incorporated into the theranostic platform. The integrated system employed an air-core inductor to generate magnetic field pulses up to 258 mT (2.16 kA). The induced displacements exhibited a direct correlation with temperature variation during a MH procedure. Additionally, the developed MH system achieved temperature rise of 8 °C when employing a magnetic field of 15 kA/m to heat volumes larger than 1 cm^3, indicating its potential for effective MH therapy. The results obtained during this investigation are important for understanding the optimal configurations of the theranostic platform and will guide future in vivo and in vitro studies.

Figure table

Content table

Chapter 1: Introduction

Introduction

With its complex and heterogeneous nature, cancer continues to pose a significant global public health challenge [1]. Extensive research efforts are currently underway to enhance our understanding of the underlying mechanisms that drive cancer and develop effective therapeutic strategies. In recent years, remarkable progress has been achieved in decoding the intricate molecular pathways, genetic alterations, and microenvironmental influences involved in cancer initiation, progression, and metastasis [2]. These discoveries have shown that the development of cancerous cells is influenced by many internal and external factors, thus rendering it a multifactorial phenomenon [3]. Normal cells are transformed into cancer cells by accumulating multiple gene mutations that regulate cell division. Furthermore, a wide range of factors, including pollution, dietary habits, radiation exposure, and genetics, can trigger these mutations [4]. Consequently, this knowledge progress has helped to identify novel avenues for targeted therapies and personalized treatment approaches aimed at mitigating the complications experienced by patients.

Numerous treatment strategies, including chemotherapy, radiotherapy, immunotherapy, and surgical procedures, have been conventionally employed to inhibit tumor growth. However, it is unfortunate that these treatments often come with side effects that can negatively impact patients' overall health [5]. Thus, research is critical to develop novel techniques for early-stage diagnosis and effective therapy procedures while minimizing side effects.

In recent years, nanoscience and nanotechnology have emerged as essential contributors to pursuing innovative cancer treatments [6-9]. Additionally, nanotechnology-based procedures offer the potential for early-stage diagnosis, enabling timely intervention and improved patient outcomes. By harnessing the engineerable properties of magnetic nanoparticles (MNPs), these advancements have helped the way for innovative techniques in oncology, such as magnetic hyperthermia (MH), which holds great promise for improving cancer therapy, allowing that selectively eradicate cancer cells while preserving healthy tissues.

Particularly in the case of MH, magnetic nanoparticles are utilized to achieve precise energy deposition in cancer cells [8, 10]. This technique induces cell death by selectively

raising tissue temperature. Heat generation occurs through interaction between MNPs and external radiofrequency (100 kHz to 1 MHz) magnetic fields. As a result, MNPs become heat sources and elevate temperature at MNPs location, causing cell damage, ultimately leading to cell death, thereby minimizing side effects. However, until today, MH has not yet been considered a standalone curative treatment for cancer, but it has shown substantial potential in enhancing the effectiveness of radiation therapy and other techniques [11-13]. Furthermore, MH has been exemplified by compelling evidence from in vitro studies, in vivo experiments, and clinical observations [12, 14, 15]. However, despite its promising outcomes, the clinical application of hyperthermia remains limited primarily due to practical challenges in implementation [16], with the most crucial obstacle being the successful heating of deep tumors [11].

Since magnetic hyperthermia presents numerous advantages as an alternative and adjuvant treatment technique, it has challenges [17]. These challenges include real-time temperature monitoring, precise localization of MNPs, and ensuring scalability in pre-clinical settings. For example, real-time temperature monitoring is crucial in MH to maintain accurate control over the heating process and avoid potential damage to surrounding healthy tissues. Therefore, developing reliable and non-invasive methods for monitoring temperature changes within the tumor site during treatment is a crucial area of research.

In addition, achieving precise localization of MNPs within the target tissue is another critical challenge. The dynamic vascularization of MNPs in a living organism requires constant feedback for MH. Ensuring that the MNPs accumulate specifically in the tumor area while minimizing accumulation in healthy tissues is essential for maximizing treatment efficacy.

Furthermore, scalability in pre-clinical settings is essential for the widespread adoption of MH. Therefore, it is crucial to develop standardized protocols, medical equipment, and methodologies that can be replicated across different research laboratories and pre-clinical studies, enabling consistent and reliable outcomes. Addressing these challenges will be fundamental in advancing the field of magnetic hyperthermia and translating it into a clinically viable treatment option. Therefore, ongoing research efforts are focused on developing

innovative solutions to overcome these obstacles, thereby unlocking the full potential of MH as a safe and effective cancer therapy.

As an aforementioned consequence, theranostic platforms may hold promise for advancing the field of MH by overcoming some of its current limitations [18-21]. Traditionally, diagnostics and therapeutics have been separate entities in healthcare, with diagnosis preceding treatment. However, theranostic platforms aim to merge these two components, allowing for a more personalized and precise approach to patient care by combining diagnostic and therapeutic functionalities into a single entity. To revolutionize the treatment effectiveness for healthcare by enabling customized medicine, enhancing treatment outcomes, and reducing unnecessary interventions or side effects.

In the diagnostic aspect of the theranostic platform that includes MH, ultrasound imaging is a safe image method that could be an interesting choice [21]. It utilizes high-frequency sound waves that are transmitted into the body, interacting with various tissue structures. The transducer captures the echoes produced by this interaction and converts them into real-time images. This technology enables healthcare professionals to visualize organs, tissues, and detect potential abnormalities. Ultrasound images provide valuable diagnostic information, including tissue size, shape, and composition, and identify any abnormal structures or lesions [22]. However, there are certain limitations to the detecting size capabilities of ultrasound. For example, ultrasound alone may be insufficient when dealing with objects smaller than 1 μm, such as MNPs used for MH, as their sizes typically range below 100 nm [23, 24]. In that case, an innovative approach called magnetomotive ultrasound (MMUS) can complement ultrasound imaging to detect MNPs within tissues [25-28].

MMUS combines the principles of ultrasound imaging with the manipulation of MNPs by using external magnetic fields [29]. In this case, the interaction between an external magnetic field gradient and MNPs results in a magnetic force capable of inducing tissue movement. These movements (displacements) can be detected and quantified using ultrasound imaging, providing additional information beyond traditional ultrasound techniques [26, 30, 31]. The integration of MMUS expands the capabilities of ultrasound by enabling the detection

and localization of MNPs within the tissue. This approach holds potential in various theranostic applications, such as molecular imaging, targeted drug delivery, and functional tissue characterization [29].

In a previous study, the research group GIIMUS proposed a novel theranostic platform [21] designed to integrate MMUS and thermal ultrasound imaging with MH. An interesting aspect of this platform was the utilization of a single excitation coil for both MMUS and MH applications. Phantom experiments were conducted to demonstrate the platform's capability to map the location of MNPs and generate two-dimensional temperature maps during the MH procedure. The study also revealed that acquiring MMUS images before the MH procedure could predict the temperature distribution of MNPs during HM experiments.

Despite these successful outcomes, some remaining challenges hinder the pre-clinical implementation of the aforementioned theranostic platform. One technical limitation of the platform described in [21] was the absence of automated switching between the magnetic fields used for MMUS and MH. Due to this constraint, real-time acquisition of MMUS images during MH was not feasible. The design presented in [32] lacked the required power to conduct a comprehensive MH procedure in large-volume phantoms or potential animal applications. This limitation arises from the system's original design, which primarily emphasized MNP characterization [32].

Addressing these challenges is crucial to advance the implementation of the theranostic platform in pre-clinical settings. Overcoming the limitations in acquiring real-time MMUS images during MH and improving scalability will enhance the platform's applicability for in vivo experiments. To strengthen the evaluation of magnetomotive-induced displacements in dynamic environments [17], such as a living body, developing a robust system capable of delivering consistent feedback and controlling the application of MMUS magnetic pulses during MH becomes essential. Furthermore, enhancing the power capacity will enable comprehensive MH treatments in larger volumes, expanding the platform's potential for future pre-clinical and clinical applications.

In this research thesis, our primary objective was to develop an innovative and automatic

theranostic platform. This platform will enable pre-clinical experiments, monitor crucial physical tissue properties such as temperature, and facilitate the localization of MNPs using ultrasound imaging techniques. This integration will enhance the MH's effectiveness and minimize the risk of magnetic field overexposure. Furthermore, optimizing the theranostic platform aims to improve the experiments' performance, enable precise tissue property monitoring, and enhance the localization of MNPs through real-time ultrasound imaging. This advancement will contribute to the field of theranostics and improve the way for more effective and safer treatments in the future.

However, it is essential to acknowledge the inherent challenge of generating and synchronizing both MMUS and MH magnetic fields within a single system. MH typically operates within the 100 – 500 kHz frequency range [33-35], whereas MMUS operates below 100 Hz [25, 26, 36]. In MMUS, the utilization of a low-frequency, time-varying magnetic field is necessary due to the elastic response of tissues [28, 30], as will be discussed in detail in Chapter 2 of this thesis. In contrast, a higher frequency magnetic field is essential for MH due to the Neel and Brownian relaxation times [37], and this aspect will be detailed in Chapter 3 of this thesis. This discrepancy poses engineering and design challenges concerning material physic properties to fill the magnetic field requirements. As a result, the electronic control device of the system assumes the critical responsibility of synchronizing these two distinct natures' magnetic fields to achieve the implementation of MH therapy and MMUS image scanning. This way, creating a real histography of MNPs temperature while MH is applied is possible.

This research aims to address the aforementioned challenges by developing an automated theranostic platform. This proposed approach involved designing and implementing two separate systems for MH and MMUS, as shown in Fig. (1). These systems were interconnected and managed through a digital control system that synchronizes their operation, as illustrated in Fig. (2). By periodically activating and deactivating each system, it was achieved a complete integration within a single platform without interference. Notably, the platform utilizes the same excitation coil for both therapy and diagnosis, significantly enhancing its real-time

application capabilities. This integration of functions within a single inductor offers significant advantages, as it enables smooth operation, provides feedback, and enhances the efficiency and effectiveness of treatment procedures. It eliminates the need for separate setups or time-consuming transitions between therapy and diagnostic modes.

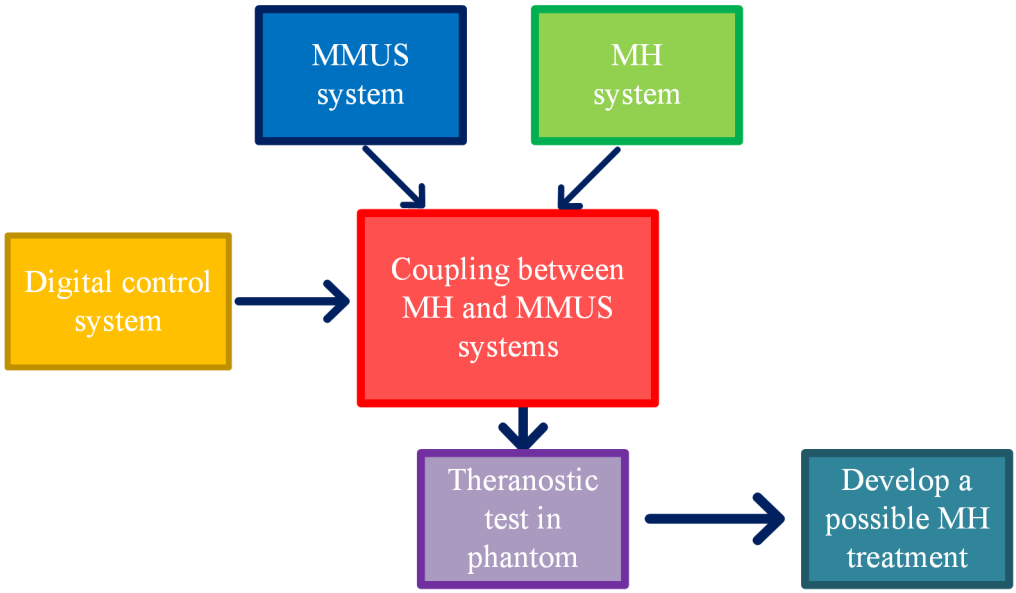

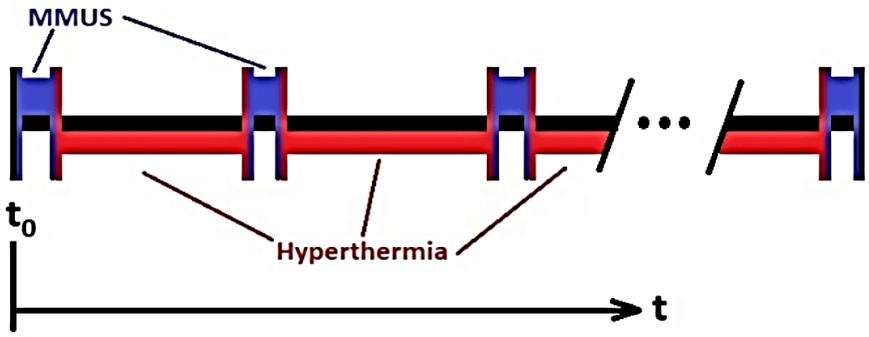

The next step involved experiments with tissue-mimicking phantoms in developing a feedback-controlled hyperthermia pre-clinical protocol that can be applied in potential *in-vivo* experiments with the developed system. Following this approach, it was aimed to overcome the previously identified limitations and provide a robust solution for integrating MH and MMUS into a theranostic platform.

This thesis is structured into four chapters, according to the following description. **Chapter 2** is dedicated to describing the development of pulsed MMUS systems. Throughout

this development process, it has identified specific aspects related to the generation of pulsed magnetic fields that require enhancement and optimization, particularly to facilitate its integration with the MH system. **Chapter 3** provides an in-depth description and characterization of the MH system. It specifically focuses on analyzing the built-in resonant inverter, which is crucial in generating the high-frequency magnetic field necessary for the hyperthermia procedure. **Chapter 4** explores the developed theranostic platform, examining multiple experiments to comprehensively understand its performance, capabilities, and potential issues. This chapter offers valuable insights into integrating and implementing the theranostic platform, paving the way for future studies and real-world applications. Also, **Chapter 4** presents the conclusions derived from the data analysis and findings obtained throughout this research.

Chapter 2: Development of Pulsed Magnetomotive Ultrasound Imaging Systems

Introduction

Nanostructured agents have gained increasing relevance in various scientific and technological fields because of, but are not restricted to, their versatile optical, thermodynamic, chemical, electric, and magnetic properties [38, 39]. One of the key advantages of these materials is their ability to be engineered for energy absorption in response to external stimulation, such as mechanical, magnetic, and optical, which makes them useful as contrast enhancers for imaging techniques such as ultrasound.

Ultrasound is a widely used medical imaging modality that is considered a safe, low-cost, portable, and real-time method. However, standard ultrasound techniques' spatial resolution and contrast limitations constrain nanostructure localization within tissues [25-28]. To overcome this limitation, different techniques have been proposed to monitor specific physical outputs that may arise from the interaction of nanoparticles with an external stimulus applied to the target [29]. The underlying concept behind these approaches is that the detected signal magnitude is proportional to the concentration of nanoparticles [40]. For example, when exposed to an external magnetic field, a tissue labeled with magnetic nanoparticles (MNPs) is magnetically attracted to the magnetic field source, generating micrometric displacements within the tissue. The induced displacements can be detected using ultrasound techniques by applying algorithms commonly used in elastography analysis [41]. The spatial distribution of these displacements can be processed to indicate the location of MNPs [42]. This technique is known as magnetomotive ultrasound imaging (MMUS) [26-28]. It has been studied for different applications, including the detection of MNPs in mouse tumors [26] and rat lymph nodes [43], evaluation of rat gastric function [44], sensing the endocytosis of MNPs into living cells [45], and imaging blood clot formation [46].

The external magnetic field is commonly generated by electromagnets using harmonic pulses, a single pulse, or pulse train magnetic fields [41]. In the case of harmonic magnetic field stimulation, audio amplifiers are employed for their low cost, easy access, and simplified operation [30, 43]. However, these devices present some drawbacks, preventing the optimal conversion of electric energy to the magnetic field (<70%) [47], such as minimum load

impedance, heating susceptibility in the coil and amplifier, delays related to the voltage-current phase, and no DC output support [47, 48]. In consequence, in these amplifiers, high-impedance coils greater than 2 Ω are required, resulting in long windings and poor fill factor, usually <90% [49].

Other applications using a single pulse or pulse train have been achieved with commercial current amplifiers connected to function generators [26, 50, 51]. These amplifiers present extended current-voltage features and versatility in pulse duration ranging from a few milliseconds to 5 seconds. Nevertheless, their implementation involves high costs and special infrastructure installation and still presents minimum load impedance defined by the output power. Recently, other studies using pulsed magnetic field generators based on capacitor discharge [25, 52, 53] have shown improvements in magnetic field features such as field magnitude up to 950 mT, acceptable variable pulse duration (2 ms – 1s), and capabilities of driving low-impedance coils, lower than 2 Ω.

In some situations, coils presenting lower electrical impedance are desired. For example, a recent paper proposed using MMUS images in combination with magnetic hyperthermia in a theranostic platform [21]. This platform was designed to use a single coil to apply both magnetic fields for MMUS and magnetic hyperthermia. In magnetic hyperthermia, heat is dissipated from the interaction of an external magnetic field and MNPs for cancer treatment. In this case, lower impedance coils are required to generate magnetic fields with frequencies ranging from 100 kHz to 500 kHz.

For this reason, a low-impedance output amplifier is desired to drive the coil and generate intense magnetic field pulses for MMUS, similar to that used in transcranial magnetic stimulation (TMS), where a capacitor bank is discharged through the coil. In addition, other strategies of current generators, namely resonant converters [53, 54], have been developed, and they can be adapted for biomedical purposes. These converters work as uninterrupted current power supply based on high-frequency inverters with the capability to continuously maintain hundreds of amperes current levels. However, using these devices entails developing complex high-power electronic systems but creating an opportunity for new MMUS designs.

Another crucial aspect of MMUS is related to the magnetic field temporal waveform and the expected displacement response of tissues. An idealized magnetic pulse for MMUS stimulation would be a perfect square wave (blue line in Fig. 3). However, an ideal magnetic pulse is difficult to achieve due to the coil and current generator's electrical features. In practice, an exponential response is more likely to be observed in the magnetic field rise and fall times (red line in Fig. 3). In the case of a non-zero magnetic field rise-time $t_r > t_0$, the time-to-peak displacement t_{pk} (green line in Fig. 3) is not exclusively associated with the material's mechanical properties. On the other hand, the residual magnetic field can influence the induced motion and reduce tissue peak-to-peak displacement when pulse trains are used [50]. Nonetheless, this undesirable effect created by the coil's reactive properties can be reduced by proper coil optimization and a correct choice of a low-output impedance generator.

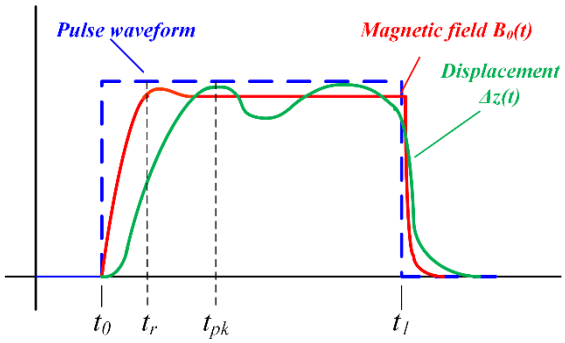

Fig. 3. The differences between the magnetic excitation and expected displacement waveforms related to the MMUS technique.

In the present study, two magnetic pulse generators integrated into an MMUS system were designed to overcome the aforementioned drawbacks of pulsed MMUS. As a starting point, the first magnetic field generator, named “generator 1”, was developed using a similar configuration of TMS devices but optimized for the MMUS technique. The second approach, “generator 2,” used a novel design based on a DC-DC resonant inverter converter. The performance of the magnetic generators was evaluated in terms of magnetic field amplitude, transient behavior, and pulse repetition frequency (PRF). The effect of the magnetic fields on the MMUS images was investigated with a tissue-mimicking phantom containing an inclusion filled with MNPs. To study the influence of the elastic properties of the phantom on the induced magneto-motion, the experiments were conducted at various temperatures in the 17 - 22 °C range.

Material and methods

A. Magnetic force

A tissue or a phantom material can be modeled as an elastic material with low viscosity. Thus, if these materials are labeled with a homogeneous distribution of MNPs, the interaction between them and an external magnetic field creates an attractive force F_z, moving the internal structures of the tissue. This magnetic force is proportional to the magnetic field magnitude B_0 and gradient, as well as MNPs susceptibility χ_s in a linear MNPs magnetization regimen [55, 56], as shown in the following equation [58]:

$$F_z = \frac{\chi_s V}{\mu} B_{0(z,t)} \frac{\partial B_0(z,t)}{\partial z} \quad (1)$$

In this equation, V is the MNPs inclusion volume and μ relative medium permeability. Therefore, by increasing the magnetic field generated, the induced displacement is enhanced and, consequently, improving the MMUS imaging contrast and the signal-to-noise ratio [26, 52]. Another important term is magnetic field time dependence, which is associated with the magnetic field waveform and attractive magnetic force. As a result, the transient displacement response is affected by both the tissue's elastic properties and the magnetic stimulation's temporal behavior [58].

B. Systems description

Several features were evaluated to investigate the performance of the generators mentioned above, such as magnetic field magnitude, transient response, magnetic PRF, and the induced displacement behavior of MNPs embedded in viscoelastic materials. Both generators were designed to circulate current magnitudes of up to 100 A through a magnetic field generating coil and to be controlled by external triggering devices. Despite the similar activation mode, their main difference is the power supply configuration and how it provides energy to generate the magnetic field. Fig. 4 (a) shows the generator 1, which is based on a capacitor discharging circuit. This platform uses a step-down converter as a charger circuit [53, 54] projected to charge the capacitor bank with a constant current, with values between 50 V and 230 V. Then, the charger circuit is disconnected, and the triggering device (here, it was

used a Tectronix function generator, model AFG320) controls the high-speed power switch, which is formed by four MOSFET IXKN45N80C in a parallel configuration, closing the circuit between the capacitor bank terminals. Therefore, the capacitor bank is discharged, forcing a high-magnitude current through the generating coil, with a controlled activation time between t_0 and t_1, as depicted in Fig. 2.

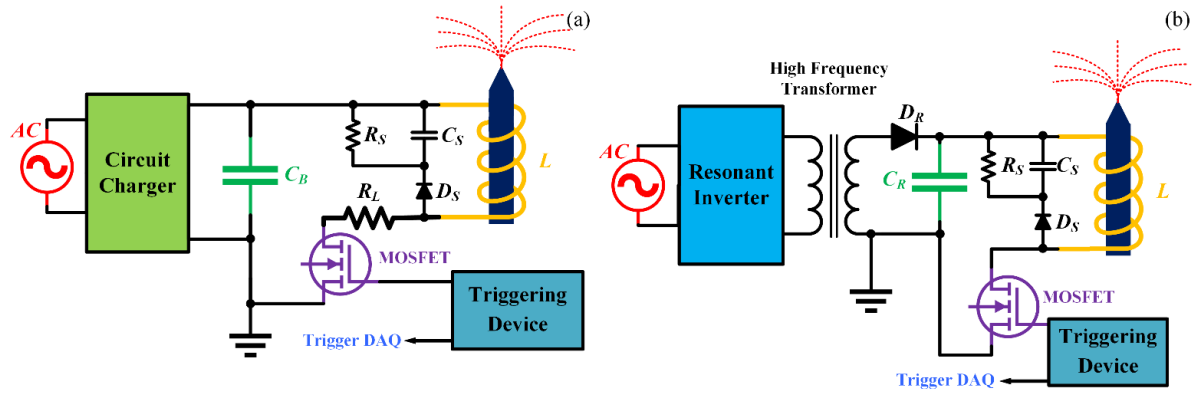

Fig. 4. Pulsed MMUS magnetic field generators. (a) Generator 1: device is based on a discharging capacitor topology activated by a triggering signal that closes a high-speed switching device. (b) Generator 2: uninterrupted DC-DC power converter that uses a resonant inverter for magnetic field generation by activating the MOSFET using a triggering signal.

Fig. 4(b) shows the pulse generator 2 based on a DC-DC resonant converter. In this case, the system works as a continuous high-frequency power supply using a variable autotransformer (JDG, TDGC2-3KVA) and a half H-bridge topology to switch a DC-controlled voltage, converting it from DC into a 40 kHz signal [53, 54, 59]. This system takes advantage of its resonant DC-DC converter to lower the voltage level and increase the current by employing a reduction transformer; then, a rectification stage is used to rectify the signal that feeds the excitation coil. Therefore, this setup can provide a constant current level when the high-speed power MOSFET closes the circuit, enhancing the control of the activation time t_0-t_1. Furthermore, the activation time can be varied without significant energy losses because it is continuously fed with current from the DC-DC converter.

Additionally, the magnetic PRF for generator 2 is substantially improved because this device does not depend on the capacitor charge time, allowing it to produce faster pulses uninterruptedly. In addition, Fig. 4 (a) and (b) show that an RDC-snubber circuit was also implemented in both generators, formed by a network of components Rs, Cs, and Ds. This circuit is widely used to limit voltage and current edge rates in high-power converters such as

flyback power supplies [60]. In this case, the snubber circuit was employed to reduce the magnetic field relaxation after the MOSFET deactivation by driving an opposite current produced by the counter-electromotive force, demagnetizing the coil's core.

C. Coil optimization for pulsed MMUS

An inductor is a reactive element where the current gradually increases in response to an applied voltage. Hence, an effective procedure to optimize the magnetic field rise-time t_r is to assume the excitation coil to be an inductor working as a low-pass LR-filter circuit, which is described by the transference function

$$H(\omega) = \frac{Re}{Re + Im} = \frac{R}{R + j\omega L} = \frac{1}{1 + j\omega R / L} \tag{2}$$

where the R and L values determine the stop frequency. R and L optimum values can be calculated by evaluating the filter response of equation (2) through a *Heaviside* step function

$$\frac{H(\omega)}{\omega} = \frac{1}{\omega} \cdot \frac{1}{1 + j\omega R / L} \tag{3}$$

Then, by converting equation (3) into time-dominium, an exponential function characterized by the term $-t(R/L)$ is obtained:

$$h(t) = 1 - e^{-t(R / L)} \tag{4}$$

This equation associates the specific time for the current to reach its maximum value in response to the applied stimulation, i.e., $t \approx t_r$. Here, t_r was taken as the time to reach ~95% of the maximum theoretical value. In order to determine a specific inductance L by using a required t_r value, as shown in Fig. 3, it is essential to consider two limiting criteria: i) expected mechanical response and ii) core magnetic properties of the coil. In this case, the t_r value should be as low as possible to avoid possible interferences induced by a magnetic field modulation on the time-to-peak displacement (t_{pk}) [61]. Additionally, magnetic hysteresis plays a critical role in limiting the minimum t_r value that the coil can reach under a pulse excitation regimen. For example, the maximum frequency at which a silicon steel core can handle a saturation magnetic flux (approx. 1.2 T) is 400 Hz [62] (period of 2.5 ms). Thus, to avoid a possible skin effect in the core [63, 64], the optimal and minimum possible value for t_r in this study was 2.5

ms due to the presence of a steel core.

Following the analysis of *h(t)*, the variable *R* can be found by considering the maximum current I_{max} and voltage V_{max} that the generator can provide at a safe full-load state. For example, by considering generator 1 operating at 100 A and 200 V, which are close to the generator's maximum capabilities, and using Ohm's law, the minimum load was R = 2.0 Ω. Therefore, using t_r = 2.5 ms and R = 2.0 Ω in equation (4) and taking 99% of the maximum value of *h(t)*, an inductance of 582 µH was obtained. However, generator 1, as depicted in Fig. 4(a), had a series resistor R_L = 1.4 Ω between the coil and switch device, which acted as a current limiter for the generator. Consequently, the coil impedance was designed to be 600 mΩ at 400 Hz.

To manufacture the coil, 130 turns of copper wire (AWG 17) were wound around a steel core (diameter = 16 mm, length = 40 mm, tip-angle = 45°), taking special care to achieve the aforementioned inductance and impedance values. Then, an impedance analyzer (Agilent, 4294A Precision Impedance Analyzer, 40 Hz to 110 MHz) was used to measure the actual coil parameters at 400 Hz, obtaining 584 µH for the inductance and 664 mΩ for the coil impedance. Next, this coil was tested with both pulsed MMUS units by measuring the generated magnetic field with a gaussmeter (TMAG-1T, Globalmag, Cotia, SP, Brazil). Finally, the results were compared with the analytical predictions of the low-pass LR filter using the *Heaviside* step function.

D. Phantom preparation

A cubic tissue-mimicking phantom containing a hemisphere inclusion labeled with MNPs was prepared. Each phantom material was produced by dissolving 5% bovine gelatin Bloom 250 (Gelita, Sao Paulo, Brazil) and 2% Agar (HiMedia, Mumbai, India) at weight-mass concentrations in Milli-Q water at 90°C. Agar and gelatin are well-known materials for mimicking soft tissue in terms of acoustic and elastic properties [65, 66]. The molten solution was maintained under magnetic stirring for 1 hr until homogenization was completed. Then, the mixture was cooled to 36 °C, and 0.2% of formaldehyde (Synth, São Paulo, Brazil) was added. At this point, the molten agar-gelatin mixture was ready to be poured into an 80 mm x

80 mm x 40 mm mold for cooling and gelling at 5 °C overnight. The inclusion and background were made using the same procedure and materials. In addition, the hemispherical inclusion with a radius of 7.5 mm was labeled with zinc-ferrite MNPs ($Zn_{0.1}Fe_{0.9}Fe_2O_4$), at a weight concentration of 1% [30]. The MNPs had an average size of 12 nm and a saturation magnetization of 83 emu/g. The reader is referred to [67, 68] for more details about the MNPs synthesis and characterization.

E. MMUS experiments

The experimental setup consisted of the magnetic field generator, the tissue-mimicking phantom, an ultrasound imaging system (SonixRP, Ultrasonix), and a parallel data acquisition system (SonixDAQ, Ultrasonix) connected to a linear array transducer (L14-5/38). The phantom, coil, and ultrasound transducer were held and aligned according to the experimental setup depicted in Fig. 5, leaving a gap (0.2 mm) between the phantom and the coil. The ultrasound echo data acquisition, at a frame rate of 4 kHz, was synchronized with the magnetic pulsed excitation.

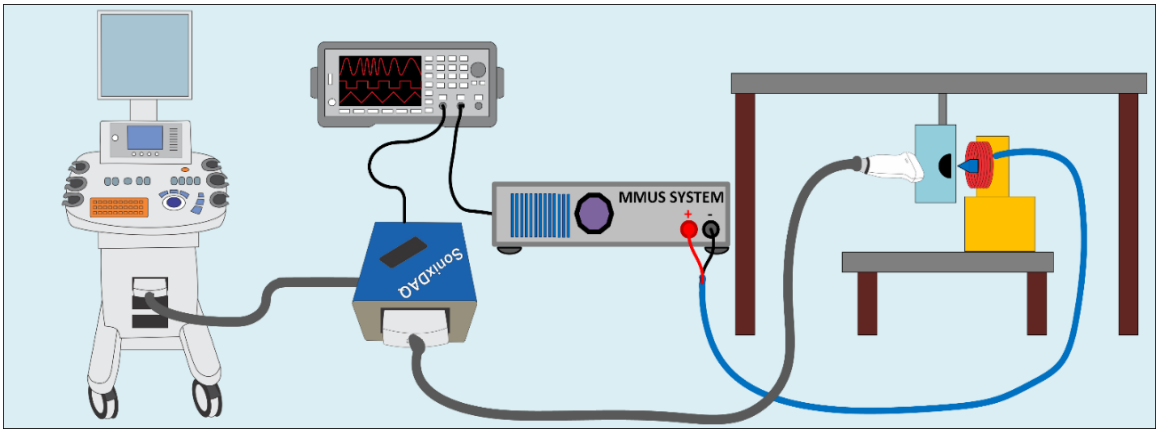

Fig. 5. Depiction of the pulsed MMUS imaging setup. The arrangement comprised an ultrasound imaging system coupled to a SonixDAQ parallel data acquisition device, a pulsed MMUS generator triggered by a function generator. The ultrasound transducer was placed in contact with the phantom and positioned opposite the coil.

F. Displacement analysis

A cross-correlation algorithm was applied between consecutive ultrasound RF signals to estimate the displacement map of the internal structure of the gelatin phantom [41]. The induced displacements within the inclusion (5 mm from the source field) were analyzed at different temperatures (17 – 22 °C) for both generators. In addition, parameters such as time-to-peak displacement and natural oscillation frequency were assessed. The frequency of

oscillation was estimated in two different situations: i) during the active magnetic field, "Field-ON," the resultant oscillation produced by a sudden displacement transition from a low to a high state with an extended active time, i.e., 40 ms; ii) after turning the magnetic field off, "Field-OFF," which considered the high-to-low transition.

Results

A. Magnetic field response

Fig. 6 shows the magnetic field generated with both generators by feeding the designed coil with a maximum current of 100 A. Fig. 6(a) shows the magnetic field rise-time comparison between the analytical model and device responses. The model (green square markers) agreed well with the magnetic field response of generator 1 (red line), indicating a high-accuracy prediction. Nevertheless, the rise-time obtained with generator 2 was slower and delayed in comparison with the analytical model (blue square markers). Fig. 6(b) and 6(c) show the magnetic fields produced by generators 1 and 2, respectively, for an activation time of 40 ms. For generator 1, the capacitor discharger device generated the magnetic field through different current levels. In this case, we can observe an exponential decrease in the magnetic field magnitude after reaching the maximum value due to the decay of the stored energy in the capacitor bank. In contrast, for generator 2, a more stable and nearly constant magnetic field level was achieved for longer activation times; however, a weak 120 Hz oscillation was observed due to rectifier ripple.

Fig. 6(d) shows the magnetic field magnitude for measurements taken from 0.2 mm to 16 mm from the core tip. These results demonstrate that within the MNP-laden inclusion, the magnetic field magnitude was in the 150 mT - 300 mT range. Fig. 6(e) and 6(f), the upper graph, show the minimum interval between two pulses for generators 1 and 2, respectively, using the designed coil. These results show a significant difference in magnetic PRF capabilities, with generator 2 reaching a maximum PRF of 100 Hz, and generator 1 reaching a maximum of 0.25 Hz. Additionally, Fig. 6(f) illustrates the versatility of generator 2 under a variable duty cycle test, ranging from 5 ms to 40 ms.

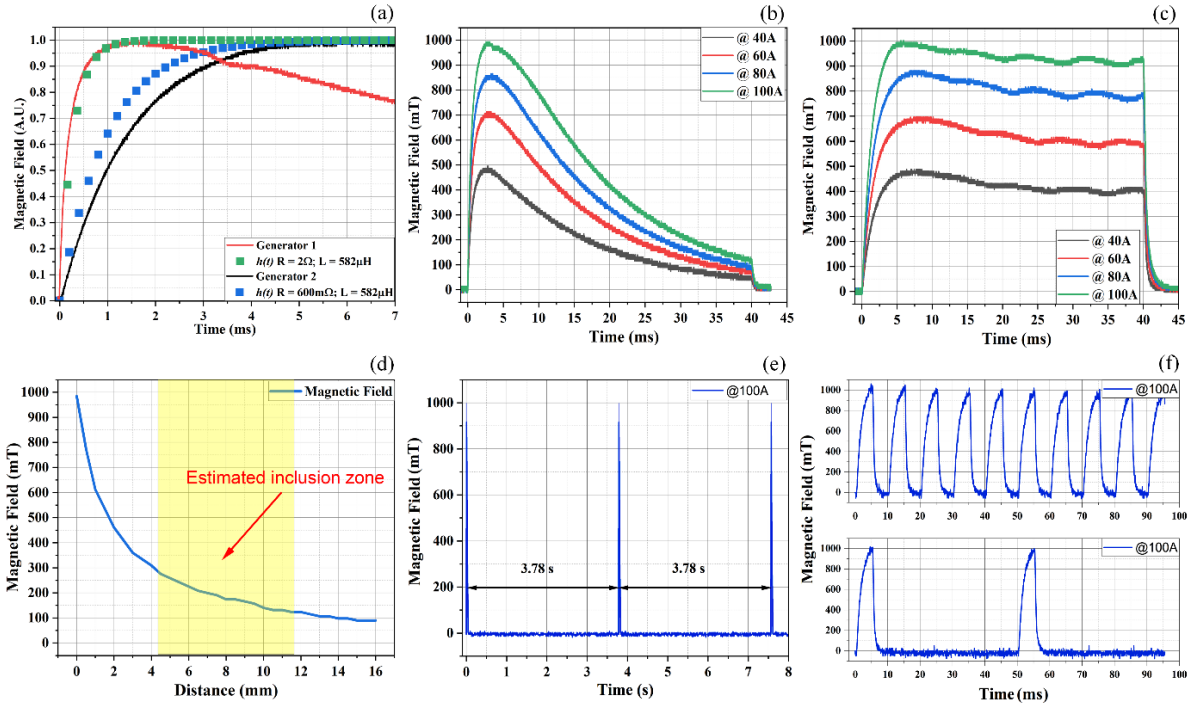

Fig. 6. Magnetic field characterization. (a) Low-pass LR filter model response and the experimental magnetic fields measured for generators 1 and 2. (b) Magnetic field generated by generator 1 at different stimulation currents and activation time 40 ms. (c) The magnetic field generated by generator 2 at different stimulation currents and an activation time of 40 ms. (d) Magnetic field intensity over distance from the magnetic field source. Minimum pulse repetition time for (e) generator 1 and (f – upper graph) generator 2. The lower graph in (f) illustrates the capability of generator 2 to operate under varying PRFs.

B. MMUS image analysis

Fig. 7(a) and 7(b) show B-mode and MMUS images of the phantom, acquired at 22 °C, respectively. The MMUS image was obtained by calculating the maximum induced displacement reached after turning the magnetic field on, at each spatial location. The inclusion can be clearly visualized in the MMUS image. Generator 1 was used in this case, and displacements of up to 25 µm for regions in the center of the inclusion were observed, and up to 15 µm for the surrounding areas due to mechanical coupling. Additionally, the time to reach these peak displacements was computed for each spatial location and is shown in Fig. 7(c). Time-to-peak displacement values of around 5 ms were measured for regions within the inclusion, while longer time-to-peak displacements were observed for areas away from the inclusion center, which is related to the shear wave propagation.

Fig. 8 shows the transient behavior of the induced displacements for both generators at a temperature of 22 °C. The plots were created by computing the average displacement within an 8 mm diameter semicircular region of interest inside the inclusion area. Fig. 8(a) compares the displacements obtained with both generators, indicating a time-to-peak displacement delay

of 1.5 ms, which is inherent to t_r (see Fig. 6(a)).

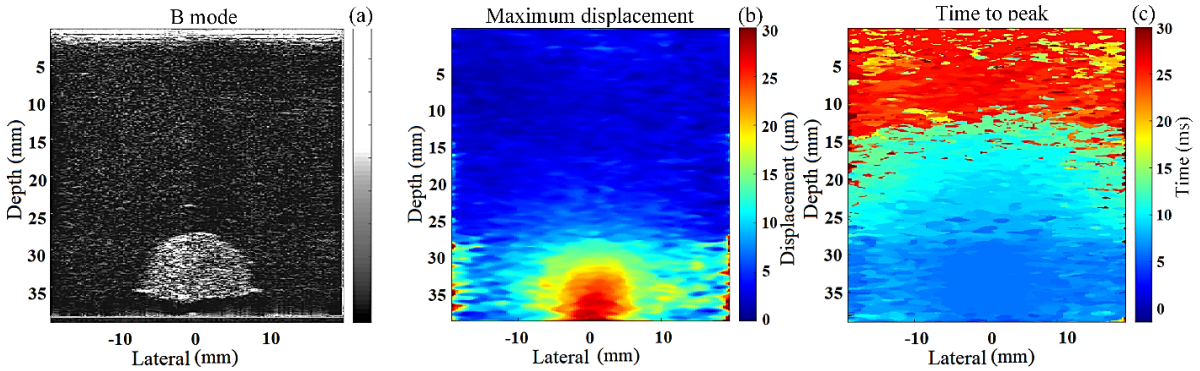

Fig. 7. Pulsed MMUS imaging results of the phantom at 22 °C. (a) B mode image obtained of the tissue-mimicking phantom embedded with MNPs. (b) MMUS image displaying a maximum displacement map. (c) Time-to-peak displacement map.

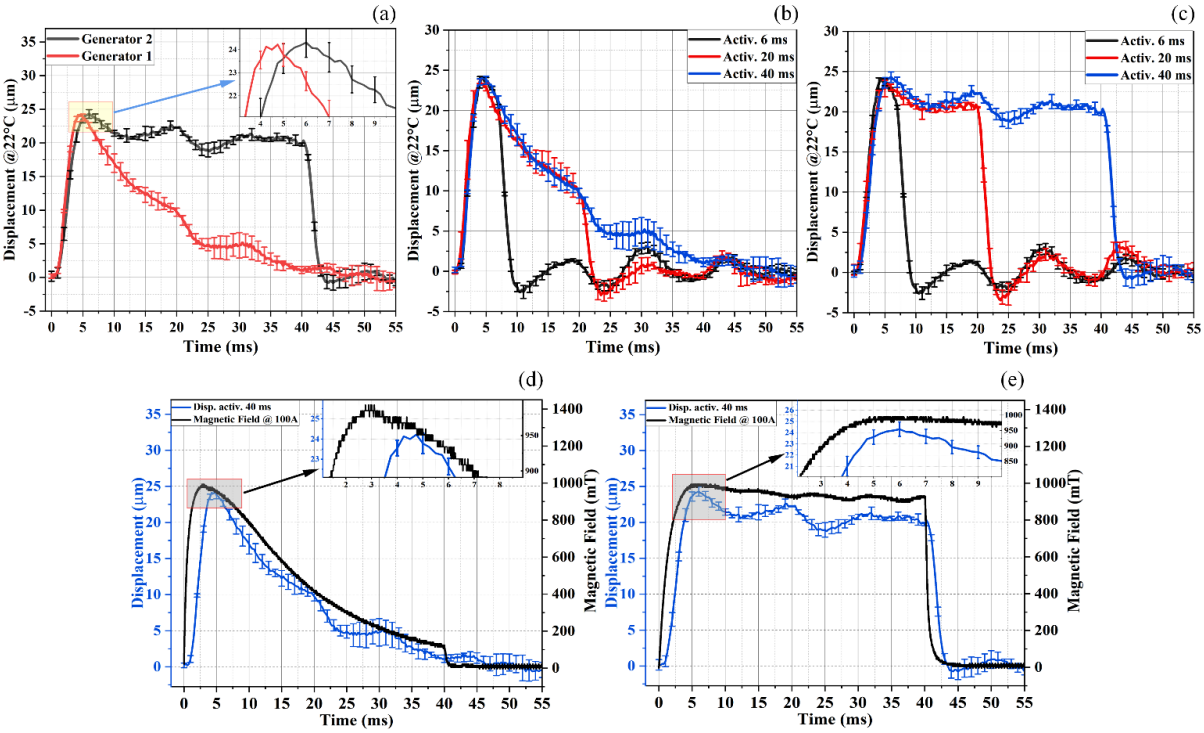

Fig. 8. Displacement behavior of the MNP-laden inclusion using both MMUS systems at 22 °C. (a) Comparison between both generators using the same activation time and coil. The inlet shows a better visualization of the time-to-peak difference between both generators. (b) Induced displacement within the inclusion using generator 1 for different activation times. (c) MNPs-induced displacement observed by applying the magnetic pulses with the inverter power supply at different activation times. (d-e) Comparison between magnetic field rise-times generated by both generators and the time-to-peak displacements.

Additionally, the decrease in magnitude observed in the displacement response for generator 1 is attributed to the exponential decay in the magnetic field due to the discharge of the capacitor device. Several experiments were conducted using different activation times; the results are shown in Fig. 8(b) and 8(c). The results for both generators were similar for 6 ms activation time, but discrepancies were verified for longer excitation times due to the discharger capacitor device. In fact, the temporal behavior of induced displacements was found to be consistent with that of the magnetic field, as shown in Fig. 8(d) and 8(e). These graphs

demonstrate a difference of 1.5 ms between the magnetic field rise-time and time-to-peak displacement for generator 1, and a difference of 1 ms for generator 2.

Fig. 9 shows the MMUS results obtained with the phantom for the experiments at various temperatures. To control the temperature, the phantom was kept inside an incubator (Cienlab, Campinas, Brazil) for a couple of hours until thermal equilibrium was achieved before each experiment. The phantom temperature was monitored during the experiment using a fiber optic thermometer system (Qualitrol NOMAD-Touch Portable Fiber Optic Monitor). Finally, the phantom was submerged in a container filled with mineral oil to avoid losing water to the environment. Fig. 9(a) shows that the phantom material shear modulus had an inverse temperature dependence. The shear moduli G were determined according to

$$G = \rho c_{sw}^2 \tag{5}$$

where c_{sw} is the shear wave speed. The time-to-peak displacement values measured at depths ranging from 29 mm to 36 mm and lateral position 0 mm, according to the image shown in Fig. 7(c), were used to estimate csw [69]. Fig.9(b) demonstrates a linear relationship between the maximum displacement within the inclusion and temperature. This trend is observed because the temperature influenced the elasticity of the inclusion, while the magnetic force remained constant. The elastic restorative force acts against the magnetic force and for this reason compliant materials offer less resistance; therefore, the displacement increased with temperature. Similarly, the time-to-peak displacements shown in Fig. 9(c) increased with temperature, between 18°C and 22°C, in both cases. Therefore, we believe the longer magnetic field tr of generator 2 was responsible for the nearly constant offset of (1.065 ± 0.046) ms between the output obtained for both generators.

Fig. 10 shows an underdamped oscillation that follows the on-to-off and off-to-on magnetic field transitions. In the case of a steady magnetic field and assuming negligible viscoelastic creep, the inclusion would ultimately reach a new equilibrium position [69]. Fig. 10 shows the frequency response for the induced displacements using both generators, according to the criteria depicted in Fig. 10(a). Fig. 10(b) shows the natural relaxation frequency of the phantom after turning the magnetic field off for an activation time of 6 ms.

Fig. 10(c) shows the frequency response during the magnetic excitation for an activation time of 40 ms.

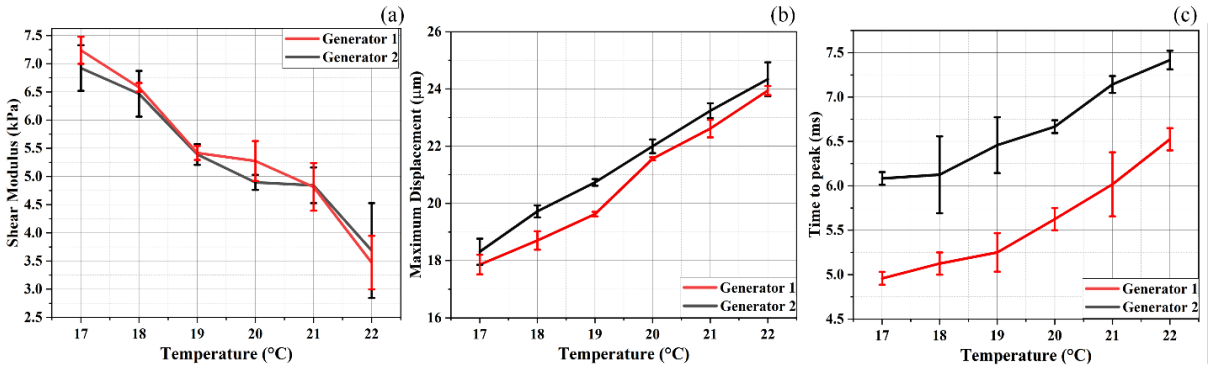

Fig. 9. Comparison of mechanical parameters, at different temperatures, of the phantom obtained with both generators. (a) Shear modulus; (b) maximum displacement; (c) time-to-peak displacement.

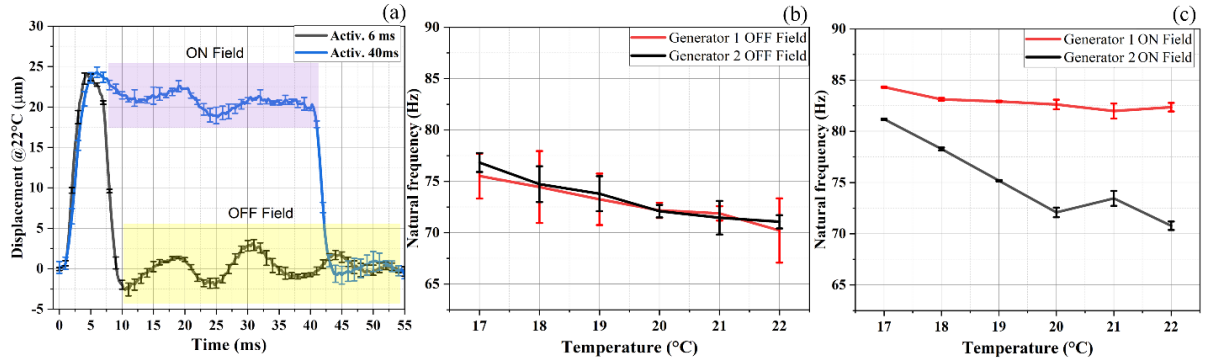

Fig. 10. Natural frequency response of the phantom. (a) Displacements obtained with generator 2, using 6 ms and 40 ms activation times. The graph highlights the fragments of the signals used to estimate the oscillation frequency of the motion induced by the magnetic force and the natural relaxation frequency after switching the field off. (b) Natural relaxation frequencies at different temperatures. The results show that higher frequencies are obtained for stiffer media. (c) Frequency response, at different temperatures, following the off-to-on magnetic field transition for both generators. The results of generator 2 agreed better with the measured relaxation frequencies.

Discussion

The magnetic field transient behavior, which was highly dependent on the switching current generator and the electromagnet, had an essential role in determining the MNPs displacement behavior. The coil impedance directly impacted the magnetic field magnitude and rise-time; despite the MOSFET having a switching rate of up to 1 MHz, the difference of magnetic rise-time t_r, shown in Fig. 6(a), suggested that the LR-filter model's R term should be considered an equivalent impedance of an electrical network. Even though the same coil was used in both systems under similar current conditions, the value of t_r obtained from both generators had significant differences related to the influence of the additional resistor R_L used only in generator 1 (see Fig. 4). Besides, the resistor R_L could not be included in generator 2,

because R_L was solely used as a current limiter and protection element for the high-voltage circuit of generator 1. As a result, the different t_r values directly affected the time-to-peak displacement t_{pk} by adding an extra constant delay [Fig. 8(a)].

Fig. 6(b) and 6(c) show significant differences in both systems' pulsed magnetic field transient behavior. For example, the exponential decay observed for the magnetic field of generator 1 resulted in non-steady magnetic force acting on MNPs, which clearly affected the induced displacements of the phantom, as seen in Fig. 8. As a consequence, the natural frequency of oscillation obtained with generator 1, while the magnetic field was on, was not consistent with the results of generator 2 [see Fig. 10(c)] or the relaxation frequency [see Fig. 10(b)]. Moreover, generator 2 was more stable in holding the magnetic field at a high level, even though a 120 Hz oscillation was observed, generated by the ripple effect of the rectification capacitor in the resonant inverter module [53, 54] [Fig. 4(b)]. However, the results shown in Fig. 8(c) and 10(c) demonstrate that the 120 Hz frequency was not noticeable in the phantom displacements, most likely because the natural frequency was in a lower range.

The pulse repetition rate capability was evaluated as shown in Fig. 6(e) and 6(f), where the minimum interval between two pulses can be observed. A minimum interval of 5 ms was obtained for generator 2, using the designed coil, which could be a benefit in cases where higher PRFs are necessary, as in real-time experiments [26]. For generator 1, the minimum interval between two consecutive pulses was 3.78 s due to the capacitance charging time, resulting in PRF = 0.25 Hz. Such PRF would be sufficient for offline applications; however, it could be undesirable for applications where the repetition rate is critical, for example, real-time MMUS imaging systems for future clinical and pre-clinical applications [70].

The pulse generator systems described in the present paper do not have the ability to amplify analogical bipolar waveforms, accepting just positive square waveforms. For this reason, it is impossible to apply negative pulses (overshot), which can be used to demagnetize the electromagnet to minimize the residual magnetic field, as described in [51]. However, with the implementation of the RDC-snubber network, electromagnet demagnetization was achieved, and the magnetic relaxation time was as low as 2.5 ms, as seen in Fig. 6(b) and 6(c).

It has been shown in [51] that long relaxation times can be a drawback in pulsed MMUS, especially in the case of applying pulse trains. The proposed approach of reversing the voltage to reduce the relaxation time was efficient; therefore, eliminating the necessity of applying negative pulses and simplifying the generator design.

Additionally, the use of a low-impedance coil enabled the production of magnetic fields with magnitudes close to 1 T and fast rise-times. This was achieved through coil optimization, a controllable process for generating magnetic fields under desired conditions, as illustrated in Fig. 6(a). This coil optimization procedure can be conducted with any power amplifier capable of driving an extended range of coil impedances.

Conclusions

Two magnetic pulse generators were designed and built specifically for pulsed MMUS. The development of these systems involved the careful analysis of multiple parameters, including the magnitude of the magnetic field, the rise and fall times, and the pulse repetition rate. Both generators were tested for detecting MNP in tissue-mimicking phantoms by evaluating the induced displacement to MNPs-laden inclusion using magnetic fields of up to 1 T and reaching displacements of 25 μm. Furthermore, the magnetic pulser using a resonant inverter as a continuous power supply showed better potential, compared to that based on a capacitor-coil discharge circuit, for real-time MMUS applications because it can operate at faster repetition rates, maintaining a stable magnetic field for more extended periods. The coil optimization procedure also contributed to achieving a magnetic response that more closely resembles a square waveform, which can be an important behavior when studying the elastic properties of tissues. To this end, an RDC-snubber circuit efficiently replaced the overshot or negative voltage pulse, simplifying the MMUS setup. Finally, both pulsed MMUS devices could detect alterations in the induced displacements due to small changes in the phantom viscoelastic properties observed during the variable temperature experiments.

Chapter 3: Development and Characterization of a Magnetic Hyperthermia Device

Introduction

Studies investigating magnetic nanoparticle hyperthermia in living beings have been conducted since the 1950s [9]. However, technological limitations during that era limited these studies to animals primarily [71]. In recent years, semiconductor technological advancements have allowed scientists to explore new and promising systems for applying this type of treatment. In magnetic nanoparticle hyperthermia or simply magnetic hyperthermia (MH), specially designed nanomaterials are used for advanced therapeutic purposes, offering potential advantages over conventional therapies, such as reduced side effects and enhanced precision in targeting diseased tissues.

In the field of oncology, the ultimate objective is to treat the tumor effectively. This is accomplished by administering magnetic nanoparticles (MNPs) into the target tissue or tumor, followed by applying an external high-frequency alternating magnetic field. This non-invasive approach generates hyperthermic effects specifically on the cancerous tissues, contributing to the goal of eliminating cancer cells [8, 9]. MNPs employed in MH are typically engineered to exhibit specific magnetic properties, with superparamagnetism being one of the most noteworthy. This property ensures that the MNPs do not retain magnetization in the absence of an external magnetic field, reducing particle agglomeration caused by magnetic attraction [72, 73], improving these MNPs for biomedical applications [74, 75], and avoiding problems like cytotoxicity and uneven distribution throughout the body [76, 77].

In MH, the generation of heat is primarily attributed to magnetic hysteresis loss. Magnetic hysteresis refers to the energy dissipation that occurs when a magnetic material undergoes repeated magnetization cycles in response to an external magnetic field. In this case, the heat generated can be described based on the magnetic hysteresis cycle relying upon the material's magnetization M that responds to the applied magnetic field H [78] as

$$W_h = \int_{H\,min}^{H\,max} \mu M(H)dH \tag{6}$$

where W_h is the energy dissipated in each hysteresis cycle, μ is the relative magnetic permeability of the material, and $M(H)$ is the material magnetization due to magnetic field H.

In a continuous scenario, wherein it is considered an assembly of magnetic nanoparticles exhibiting superparamagnetic behavior, characterized by minimal coercivity and remanence, the magnetostatic field is negligible, resulting in insignificant interaction [55]. In this case, the magnetization in response to an external magnetic field follows the Langevin function, which is an analytical approximation applicable in situations where the magnetic field H is either static or low-frequency, typically below 10 Hz [79, 80]. However, in the case of alternating magnetic fields with higher frequencies, where the timescale aligns with the characteristic relaxation time of the system, a dynamic delay arises between the magnetization and the magnetic field, originating the so-called dynamic hysteresis [78, 80, 81]. This delay is associated with the effective relaxation time $\tau = \tau_N \tau_B / (\tau_N + \tau_B)$ where $\tau_N = \tau_0 e^{KV_m/k_BT}$ and $\tau_B = 3\eta V_h / k_B T$ represent the Néel and Brownian relaxation times, respectively. In this context, K denotes the anisotropy constant, V_m corresponds to the magnetic volume, k_B is the Boltzmann constant, T is the temperature, η stands for the viscosity of the medium, and V_h is the hydrodynamic volume of the MNPs.

According to the linear response theory [37], when the amplitude of the magnetic field is sufficiently low, the susceptibility can be represented as a complex constant $\chi = \chi' - i\chi''$. As a result, the magnetization M produced by a sinusoidal magnetic field can be approximated as the product of the susceptibility and the applied magnetic field $M(t) = H_{max}(\chi' \cos\omega t + \chi'' \sin\omega t)$. This linear relationship between the magnetization and the magnetic field allows for a simplified understanding and analysis of the system's behavior. In this case, the dissipated power can be written as [37]

$$P = W_h f = \pi \mu_0 f H_{max}^2 \chi''$$
$$\chi'' = \frac{2\pi f \tau}{1 + (2\pi f \tau)^2} \chi_0 \quad (7)$$

where χ_0 is the static susceptibility. Equation (7) is commonly used to compare the heating efficiency of MNPs in terms of the specific loss power (*SLP*), which can be defined as

$$SLP = \frac{P}{\rho} \tag{8}$$

where ρ is the density of MNPs [82], this characteristic quantitatively measures the amount of heat generated per unit of nanoparticle mass.

Based on the linear response theory, the dissipated power directly correlates with the frequency (f) and increases quadratically with the applied magnetic field (H^2). Therefore, to achieve efficient and precise heating of MNPs in MH treatments, careful consideration must be given to the technique's sensitivity towards magnetic field amplitude and frequency. Furthermore, optimal values for these parameters are also influenced by various factors related to the properties of MNPs, including magnetic anisotropy, blocking temperature, sphericity, and size. Therefore, the success of MH-based therapies relies on developing reliable and efficient devices capable of delivering a controlled magnetic field to specific target sites within the body.

In the present thesis, the main objective was to develop a theranostic platform that combines ultrasound imaging with MH using a single excitation coil, as described in chapter 1. In this platform, the magnetomotive ultrasound (MMUS) technique is investigated to detect the presence of MNPs within a tissue. MMUS relies on the movement of MNPs and the surrounding tissues in response to an external magnetic field gradient, necessitating a non-uniform magnetic field configuration. Although some studies have aimed to improve field homogeneity MH to regulate temperature distribution better and potentially reduce non-specific tissue inductive heating, the use of a non-uniform magnetic field configuration has demonstrated efficacy in small animal applications [83, 84]. In addition, this approach offers advantages, such as preventing the heating of non-specific organs where magnetic nanoparticles (MNPs) may accumulate, such as the liver [85].

One crucial challenge encountered in MH therapy using a non-uniform field configuration is the rapid decrease in magnetic field strength over distance [18, 86]. To overcome this limitation, an MH magnetic generator device must be designed to handle high-power duties (> 1 kW for *in vivo* experiments). These designs are essential for maintaining a

consistent magnetic field strength at frequencies above 100 kHz, even at significant distances from the magnetic field source. It is important to note that a higher power input is necessary as the distance between the magnetic field source and the target tissue increases. However, ensuring that the power remains within a suitable range is crucial to prevent undesired inductive heating. In this scenario, resonant inverters have emerged as an optimal solution to fulfill this requirement, gaining considerable popularity and widespread implementation [87].

As their name indicates, a resonant inverter is an electronic circuit that generates high-frequency alternating current or voltage with improved energy efficiency. It is commonly employed in various applications, including power electronics, renewable energy systems, and high-frequency magnetic field generation for magnetic hyperthermia [53]. An essential feature of a resonant inverter is its ability to operate close to a resonant frequency, allowing optimal power transfer and reduced energy losses. In addition, the inverter can store and release energy efficiently by utilizing resonant components, such as capacitors and inductors, minimizing losses due to switching and conduction. The resonant inverter circuit typically consists of switching devices, such as transistors based on metal oxide semiconductor field effect (MOSFETs) or insulated gate bipolar transistors (IGBTs), and resonant components connected in a specific configuration. Also, standard resonant inverters include the series resonant inverter and parallel resonant inverter, whose choice depends on the application requirements. Besides, resonant inverters offer benefits such as increased power density, reduced electromagnetic interference, and enhanced system stability. These advantages enable the design of compact and portable MH devices that can be easily incorporated into clinical settings, providing flexibility in treatment delivery and improving patient comfort [88].

However, the technology of resonant inverters in MH has not yet been extended beyond the characterization of MNPs, small animal *in vivo* studies, and some limited clinical cases [8, 32, 81, 89, 90]. This is due to the inherent challenges associated with implementing complex control and safety systems required for their broader application. Accordingly, this study aims to introduce a magnetic hyperthermia device that addresses several key challenges existing technologies face, such as scalability and heating uniformity, and a new feature, the capability

of synchronized working with theranostic applications.

Materials and methods

A. High power supply for a resonant inverter

A simple rectification power supply is frequently employed in induction heating devices and typically consists of a straightforward rectification diode bridge along with a rectification capacitance. However, performing MH experiments *in vivo* demands a more sophisticated power supply design than conventional setups [91]. By incorporating advanced control features and additional components, it is possible to assure optimal performance, precise control, and reliable operation. Thus, the power supply must include current-voltage control and soft start functionality. For example, by regulating the current and voltage levels, achieving the desired heating level and avoiding excessive power consumption or overheating is possible. At the same time, a soft start feature is essential in high-power MH applications [92, 93]. A soft start gradually ramps up the power delivered to the induction heating semiconductors and coils, reducing the initial surge of current and preventing abrupt and potentially damaging thermal stress. This gradual power increase enhances the device's reliability and longevity and contributes to a smoother, more controlled heating process [94]. Therefore, this power supply design should incorporate techniques that may include complex control algorithms, high-speed switches, resonant circuits, feedback loops, and digital control systems. For this purpose, a synchronous buck converter, also referred to as a step-down converter, was implemented [54, 59]; see Fig. 11 (a). This DC-DC (direct current to direct current) power converter is specifically designed to adapt a higher input voltage to a lower output voltage level. By utilizing this converter, it becomes possible to regulate both the output voltage and current to achieve a desired power level.

Fig. 11(b) shows a photograph to showcase the synchronous step-down converter. Firstly, two-phase voltage sources feed the system, V1 and V2, operating at 127 V per phase with a potential of 220 V between phases. Subsequently, the contactor RL1 (T91-1C) and the resistor R1 (50Ω, 50W) are used to gradually charge the capacitor bank C1 (3x EPCOS B43875-A5228-Q5) through the diode bridge BR1 (MDS100A-12). Next, the voltage-current sensor

U1 (supplementary material 1) continuously detects the voltage and maintains communication with the DSP synchronous control board U3 (supplementary material 2). Until the C1 voltage reaches a minimum of 250V, U3 energizes the contactor RL1, allowing the current to bypass resistor R1. Following this, U3 generates signals to activate the internal transistor of the power IGBT module Q1 (FF450R12KT3), activating the switching from a minimum duty cycle until it reaches the predetermined reference value (soft start procedure). This control mechanism ensures the regulation of the average output voltage for a specific load.

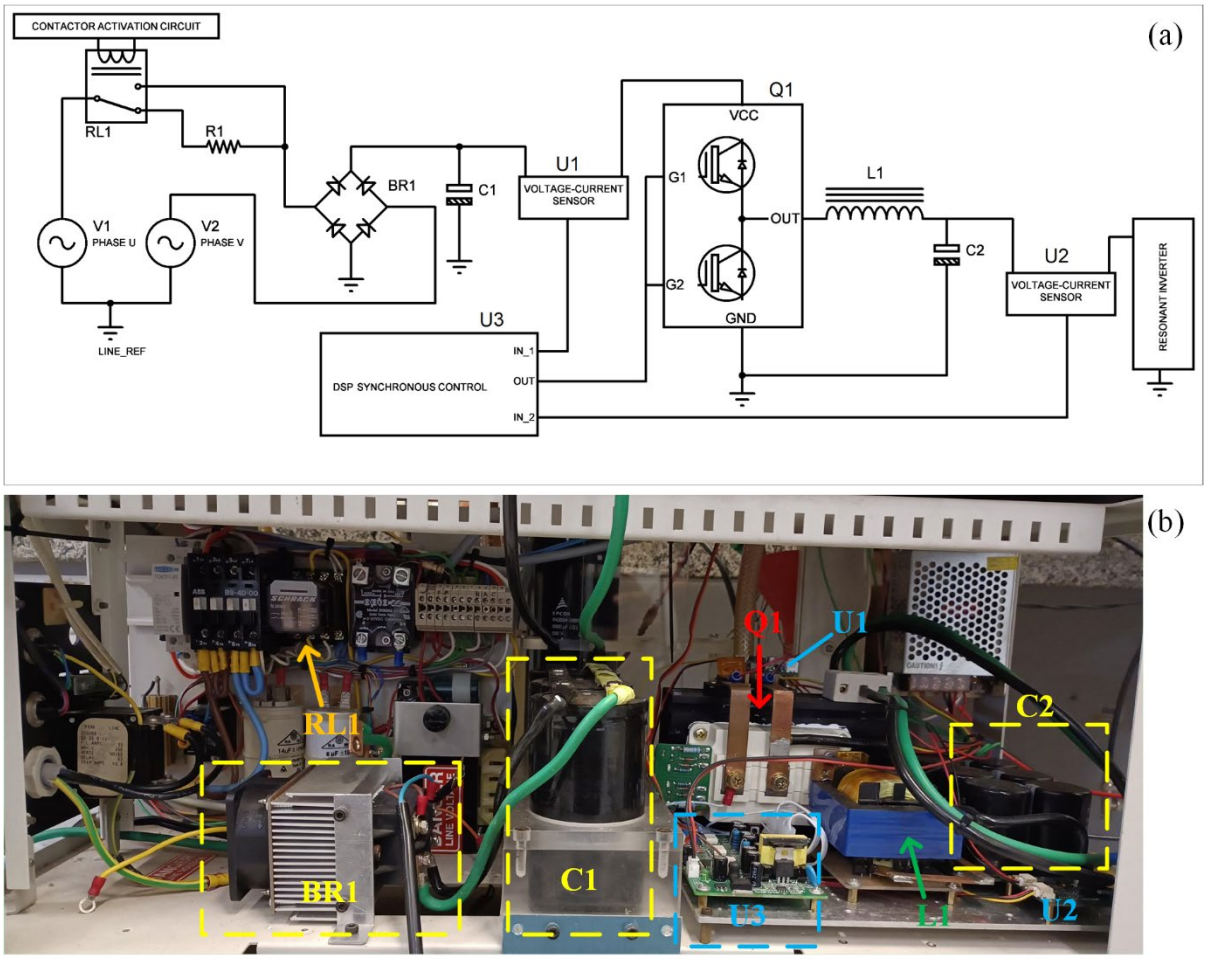

Fig. 11 High-power step-down converter. (a) The circuit schematic of the controlled variable power supply based on a step-down converter with capacities of 250 – 30 V and 100 A. (b) A photograph showcasing the developed step-down converter setup for the MH system and its principal components. RL1 is the power contactor, BR1 is the diode full bridge, C1 and C2 are two capacitor banks, Q1 is an IGBT power module, U1 and U2 are circuits designed for sensing input/output current and voltage, and finally, U3 is the power supply controller.

The operation of this converter can be summarized as follows. First, the low-side transistor of Q1 is switched off, while the high-side transistor of Q1 is switched on. This allows the current to flow from the input source to the inductor L1 (250uH 100A), which stores energy as a magnetic field. Subsequently, the inductor L1 releases the stored energy, allowing the current

to flow towards the output capacitor bank C2 (consisting of 8 x Epcos B43504-A9477-M97) and the load (resonant inverter).

In the second stage, as the high-side transistor of Q1 switches off and the low-side transistor switches on, the changing magnetic field of the inductor induces a voltage across it. This voltage maintains the current flow through the load via the low-side transistor of Q1. In addition, the output capacitor C2 stabilizes and filters the output voltage, minimizing ripples and fluctuations.

Finally, using the U2 sensor, the feedback circuitry monitors the output voltage and current values. These values are then compared with the reference value inside the U3 control circuit. Suppose discrepancies exist between the desired and actual output voltage or current value. In that case, the control circuit adjusts the duty cycle of the PWM signal to regulate the output voltage accordingly.

B. Full-bridge inverter

A full-bridge inverter utilizes a complete bridge configuration of power electronic switches to convert DC power into AC power [53, 54, 95]. The full-bridge inverter comprises four power electronic switches arranged in an H-bridge configuration, see Fig. 12. In this configuration, each switch Q is typically implemented as a power transistor. For this particular case, they are embedded within IGBT modules 1 and 2 (FF150R12RT4).

During operation, the switches Q in the full bridge inverter are controlled complementary to produce the desired AC output waveform. When Q1 and Q4 are turned on, current flows from the DC input through Q1, the resonant load, and Q4 to the other side of the DC input, creating a positive half-cycle of the AC waveform. Conversely, when Q2 and Q3 are turned on, current flows in the opposite direction, creating a negative half-cycle of the AC waveform. By controlling the IGBT's switching sequence and duty cycle, typically maintained below 50%, the full-bridge inverter can generate a high-quality AC output waveform with adjustable frequency and voltage.

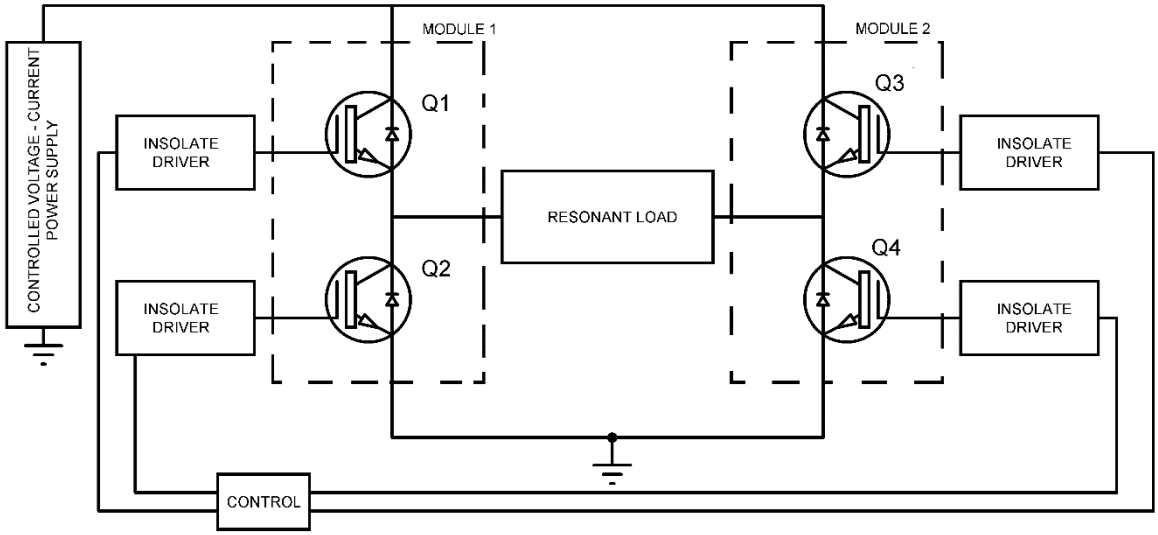

Fig. 12. The full-bridge configuration of a DC-AC converter that supplies a resonant load, known as an H-bridge, comprises four switches activated, each one by an isolated driver ruled by a control stage. In this schematic, Q1, Q2, Q3, and Q4 are the switches implemented as power transistors and embedded within IGBT modules 1 and 2.

It's important to note that the output waveform will be a bipolar square waveform due to the nature of the full-bridge configuration. Full-bridge inverters offer superior power handling capability, improved efficiency, and better control over the output waveform than simpler inverter topologies. However, they require more complex control circuitry (supplementary material 3) and have a higher component count, such as IGBT activation drivers, usually implemented using a totem pole circuit configuration [96]. Therefore, full bridge inverters are well-suited for medium to high-power applications requiring precise control and high-quality AC output.

C. Class D series resonant inverter circuit

A series resonant inverter (SRI) is a type of resonator specifically designed to operate with a series resonant load. This load typically consists of an inductor L_s and a capacitor C_s connected in series, along with their respective active part R_s, as shown in Fig. 13. In cases where this circuit has a high-quality factor Q_s, the current passing through the inverter becomes nearly sinusoidal. The quality factor Q_s represents the ratio of energy stored in the reactive elements to the energy dissipated during each cycle. For example, in the resonant inverter used in this thesis, the calculated Q_s was 10. One significant advantage of SRI is the low voltage experienced across the inverter transistors and immunity to the DC-current state. Additionally,

utilizing low-resistance IGBTs in the bridge configuration ensures high efficiency.

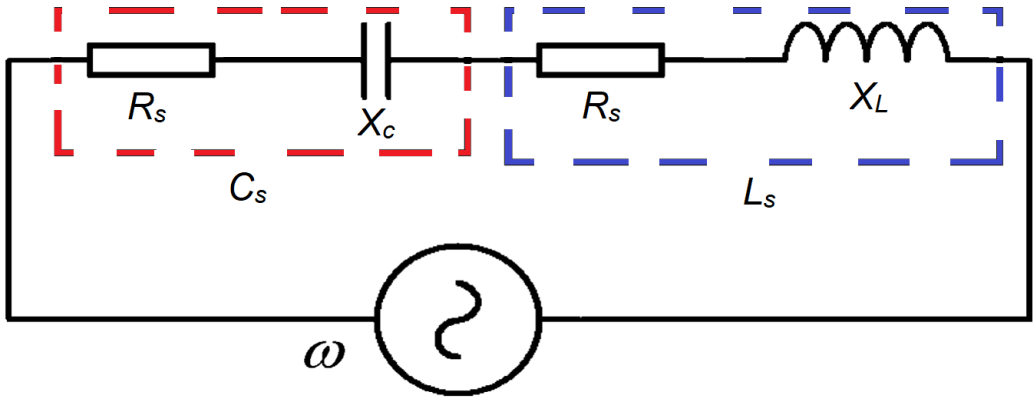

Fig. 13. A series resonant inverter consists of an inductor and a capacitor with a complex behavior when electric current flows through them. This behavior is characterized by two components: the active part, represented by the series resistance R_s, and the reactive part, represented by the reactance X. It is essential to note that the inductor and capacitor exhibit opposite reactive behaviors while the active component is a resistive value that can be taking as a resistance summary.

Researchers have extensively investigated the SRI properties, particularly emphasizing its voltage gain [53, 54]. When the inverter operates in proximity to the resonant frequency ω_0, there is a dynamic energy exchange between the inductor and capacitor. This exchange has the potential to amplify the voltage, resulting in an increased voltage amplitude V_{LS} across the inductor L_s. Mathematically, this relationship can be expressed by considering a mean input current I_m passing through the inductor L_s [54]

$$V_{LS} = \omega L_s I_m = \frac{2V_i\left(\frac{\omega}{\omega_0}\right)}{\pi\sqrt{\left(\frac{R_s}{Z_0}\right)^2 + \left(\frac{\omega}{\omega_0} - \frac{\omega_0}{\omega}\right)^2}} \tag{9}$$

where V_i is the input inverter voltage, Z_0 is the impedance at the resonance frequency and ω the inverter oscillation frequency (for the MH system development in this work, a ω_0 = 180 kHz was chosen). Based on the voltage amplification capability of the SRI, a reactive resonator configuration was adopted [97, 98], as shown in Fig. 14 (a). In this setup, MH's magnetic field excitation coil was denoted as L_{MH} and was connected to a ferrite transformer designed explicitly for voltage-to-current conversion. In addition, this transformer serves the purpose of galvanically isolating the SRI and effectively coupling the varying impedances, thereby optimizing the current flow. Incorporating the ferrite transformer enhances the current delivery to the L_{MH} coil, resulting in enhanced performance.

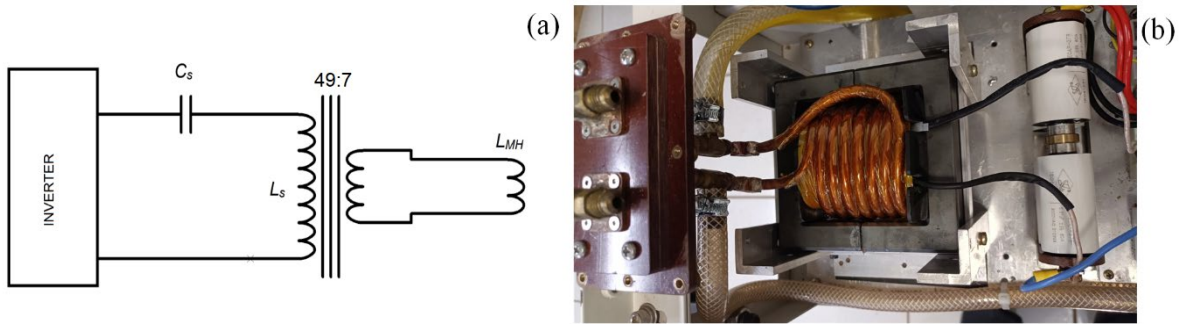

Fig. 14. Reactive series resonant inverter. (A) The Schematic illustrates the reactive transformer to increase the current that feeds the L_{MH} coil. In addition, it allows an impedance adjustment through coupling. (B) Photograph of the reactive series resonant inverter system without LMH coil installed. The image shows the water cooling system connected to the transformer output.

The designed transformer utilized a ferrite core (EE110 material PC40) with a turn ratio of 49:7. To accomplish this turn ratio, two windings were incorporated: the primary winding was constructed using Litz wire (2 wires of 70 x 32 AWG), while the secondary winding was made of a copper pipe with a diameter of 1/4" (6.35 mm). In addition, the secondary winding was equipped with a water-cooling system, as depicted in Fig. 14(B). To complete the resonator setup, four polypropylene capacitors (CORE-GTR 0.01 µF±5% 3000 VAC) were connected in a series-parallel configuration with the primary winding, resulting in a total capacitance of 10 nF with a maximum voltage of 6000 VDC.

D. Coil design

The design of the heating inductor considered various factors, including the target's operating frequency, power requirements, and geometrical constraints. In addition, specific requirements were addressed to align with the system's focus on MH therapy with simultaneous and interleaved MMUS imaging acquisition. To achieve this, the design of the excitation coil, as shown in Fig. 15(a), accounted for the shape of the ultrasound transducer. The objective was to minimize inhomogeneity in the magnetic field along the lateral dimension of the transducer (x-axis) and maximize the field intensity within the slice thickness of the ultrasound image (y-axis). This design approach aimed to achieve optimal variation in temperature (MH) and attractive force (MMUS) while ensuring compatibility with the ultrasound imaging field of view. To this end, a specially designed ellipsoidal-planar shape was implemented, featuring an inner hole of 40 mm x 10 mm.

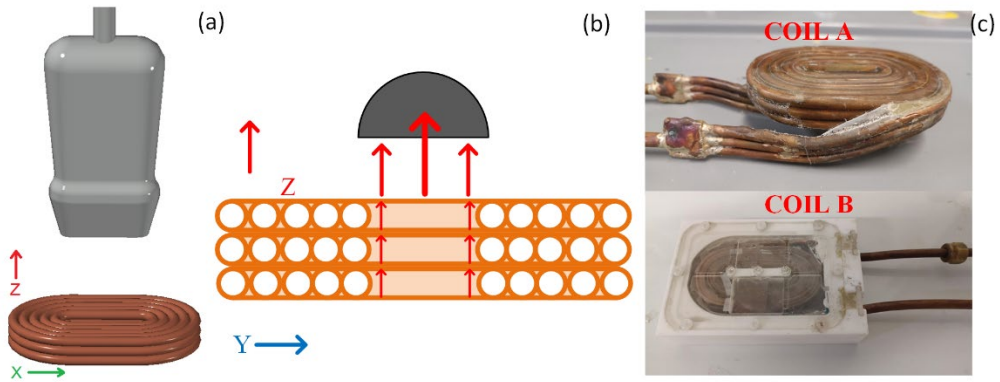

Fig. 15. Coil modeling for MH. (a) Illustration of the designed ellipsoidal-planar coil positioned below a linear medical ultrasound probe. (b) Section view of Coil A, showing the magnetic field direction depicted by red arrows on the z-axis. (c) Photographs of the two coils manufactured for the system: Coil A, constructed using copper tube, and Coil B, manufactured using a copper flat bar. Both coils were designed with similar geometries.

Fig. 15(c) shows photographs of two coils manufactured according to the aforementioned description and specifications. The first coil, referred to as coil A, was constructed using three layers of copper pipe with a diameter of 3/16" (4.76 mm). Each layer consisted of 5 turns, as depicted in Fig. 15(b). This configuration resulted in an inductance of 1.2 µH and an impedance of 1.35 Ω at 180 kHz. To ensure the structural integrity of this coil, it was encapsulated using epoxy (Tek Bond's Araldite 10-minute adhesive). On the other hand, another coil B was manufactured using a copper flat bar measuring 3/4" x 1/16" (19.05 mm x 1.58 mm). This coil comprised 10 turns and was encapsulated within a dedicated case designed for water cooling. As a result, coil B exhibited electrical properties of 2.57 µH inductance and an impedance of 2.94 Ω at 180 kHz.

E. Resonant inverter characterization

Before energizing the resonator using the inverter, an impedance analyzer (Agilent 4294A Precision Impedance Analyzer 40 Hz to 110 MHz) was employed to measure the resonator's impedance. This measurement was conducted without applying high power to accurately determine the resonance frequency and impedance values across various frequencies and inductor loads L_{MH}. Three cases were analyzed with inductance values of 1.2 µH, 2.57 µH, and a without coil.

The voltage and current ratings of three critical parts of the inverter were measured using a high-voltage differential probe (Micsig 1300V 100MHz Digital High Voltage Differential Probe DP10013) and a current probe (Micsig AC/DC Current Probe 2.5MHz CP2100B) at 25%

of inverter power. The first measurement was taken at the output inverter on the terminals of the IGBTs. The second measurement was obtained from the primary winding of the transformer, also referred to as L_s. Lastly, the voltage-current measurement was conducted at the output transformer, precisely between the coil terminals. Additionally, the total harmonic distortion was calculated for the second and third measurement waveforms, providing further insights into the quality and characteristics of the employed resonator.

F. MH experiments

For the hyperthermia measurements, three identical samples (M1, M2, and M3) containing 2 mL of zinc-substituted magnetite (nominal formula $Zn_{0.1}Fe_{0.9}Fe_2O_4$) MNPs were used at a 20 mg/mL concentration. The MNPs had a mean diameter of 12 nm and were synthesized according to the method described in [68]. To conduct the measurements, the samples were placed in spectrophotometer cuvettes and positioned above coil A, with one cuvette centered and the other two at the focal centers, as shown in Fig. 16. Additionally, a silicone sheet of 1.6 mm was placed between the cuvettes and the coil to mitigate any possible heat transference from the coil to the sample. The samples were exposed to a magnetic field magnitude of 15 kA/m at 166 kHz for 18 minutes, using 40% of the inverter's power capacity.

Temperature variations during the magnetic field application were recorded using a fiber optic thermometer system (Qualitrol NOMAD-Touch Portable Fiber Optic Monitor). Furthermore, a thermal camera (FLIR C5, MSX Multi-Spectral Dynamic Imaging) was employed to measure the temperature distribution on the surface of the samples.

Finally, the Box-Lucas was used for computing the SLP value by applying a fitting procedure using the following equation [99]:

$$y = a\left(1 - e^{-bx}\right) \tag{10}$$

Box-Lucas is a method used in thermodynamics to analyze non-adiabatic systems, where convective heat losses play a significant role. In such scenarios, the convective heat losses are often approximated as a loss term, considering the temperature difference between the sample and the ambient environment. However, the Box-Lucas analysis assumes that the system under consideration is not perfectly insulated and can exchange heat with its surroundings through

convection. This is particularly relevant when the system is in contact with a fluid medium, such as air or a liquid [100].

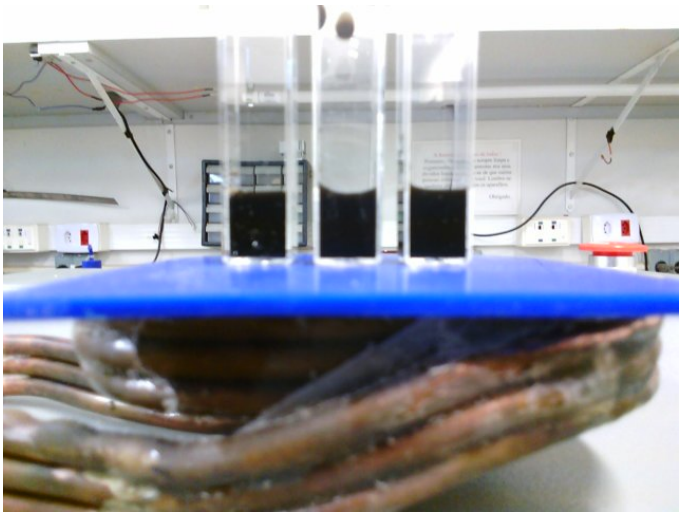

Fig. 16. Three spectrophotometer cuvettes containing MNPs samples positioned over the ellipsoidal-planar coil A on the coil center and at 15 mm from the center.

Results and discussion

A. Resonant inverter characterization

Fig. 17 shows the results obtained from the electrical characterization of coils A and B. Fig. 17(a) shows the inductance results, revealing a decrease in inductance as the frequency increases for both coils. This behavior can be attributed to the leak current in the insulating material surrounding the conductors [49]. The close proximity of the winding turns, separated only by the insulator, can create a capacitive effect, resembling the conductive layers and dielectric material within a capacitor [101]. Consequently, the insulator begins to exchange electric loads across frequencies, leading to the observed effect, which can affect the capacity of the coil to generate a strong magnetic field at higher frequencies (above 200 kHz). Considering this situation in the design of coils utilized in induction heating systems is essential. Due to the high voltages (> 150 VAC) that the coils experience it places additional stress on the insulators. Therefore, careful selection of insulating materials is crucial. In the present case, the coils' insulator consisted of a 0.5 mm mylar sheet with a dielectric resistance of 133 V/µm and a maximum work frequency of 250 kHz. Therefore, this effect is considered acceptable for the proposed conditions.

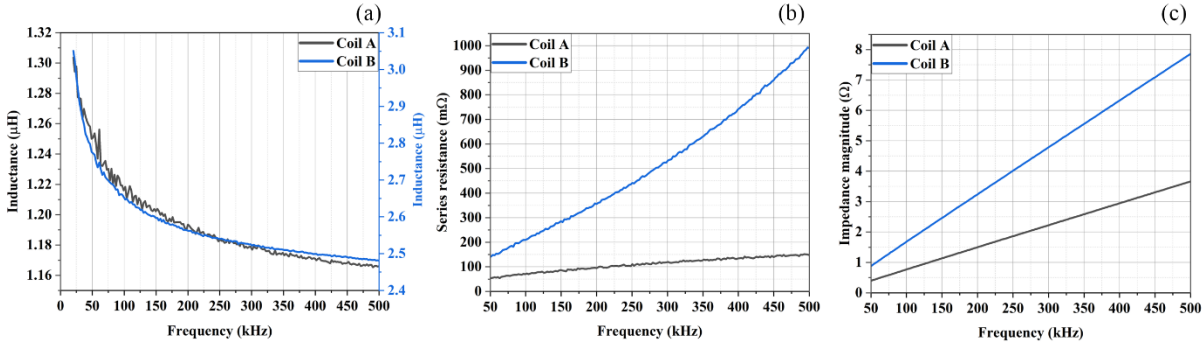

Fig. 17. Electrical characterization of coils A and B. (a) Series inductance characterized by exponential decay behavior. (b) Series resistor over frequency using a current of 2 mA. (c) Impedance magnitude over frequency.

Fig. 17(b) compares the series resistances obtained for both coils, revealing a noticeable difference in the slope of the behaviors. This discrepancy directly impacts the overall impedance of the inductor, as demonstrated in Fig. 17(c), resulting in a substantial increase in magnitude, exceeding a twofold difference for frequencies above 125 kHz. Consequently, assuming a constant voltage supply from the transformer, the potential gain in magnetic field strength is hindered due to the reduced current resulting from the elevated impedance of coil B. Furthermore, it is essential to emphasize that the increased resistance observed for coil B, as shown in Fig. 17(b), is primarily attributed to the reduction in the effective cross-sectional area available for the current flow. In other words, the resistance of a conductor is determined mainly by its cross-sectional area and resistivity. Therefore, the skin depth phenomenon, which affects the depth of current penetration into the conductor, directly impacts the effective cross-sectional area available for current flow [102].

Fig.18 shows the electrical impedances of the coils for three different scenarios that the resonant inverter may encounter depending on its load conditions. In the first situation, when no-load (coil) is connected to the transformer terminals [Fig. 18(a)], a noticeable shift in the resonant frequency is observed, decreasing to a minimum value of around 25 kHz. In this case, the reluctance of the transformer was eliminated entirely, and only the total inductance of the primary winding remained [103, 104]. The concept of transformer reluctance relates to the resistance encountered by magnetic flux lines as they pass through a specific path or medium.

In practical terms, when the secondary winding of a transformer remains unconnected to a coil, the primary winding exhibits higher inductance compared to when a coil or load is

connected to the secondary winding. In this context, reluctance can be seen as analogous to electrical resistance; however, instead of impeding the flow of electric current, it restricts the flow of magnetic flux [105]. For example, as illustrated in Fig. 18(b), the reluctance of the transformer became more pronounced when coil A was connected as the load. This leads to a shift in the resonant frequency, increasing it to 166 kHz by reducing the transformer's inductance. As an additional result, the impedance experienced a smoother transition, approaching the expected power values for our MH application. This indicates that at the resonance frequency, the impedance was 4.5 Ω. Thus, the resonant inverter can handle a maximum current of 55 A_{pk} when utilizing a 250 VDC in the power supply. On the other hand, in Fig.18(c), coil B exhibited similar behavior to the previously described case, but the resonance occurred at around 130 kHz.

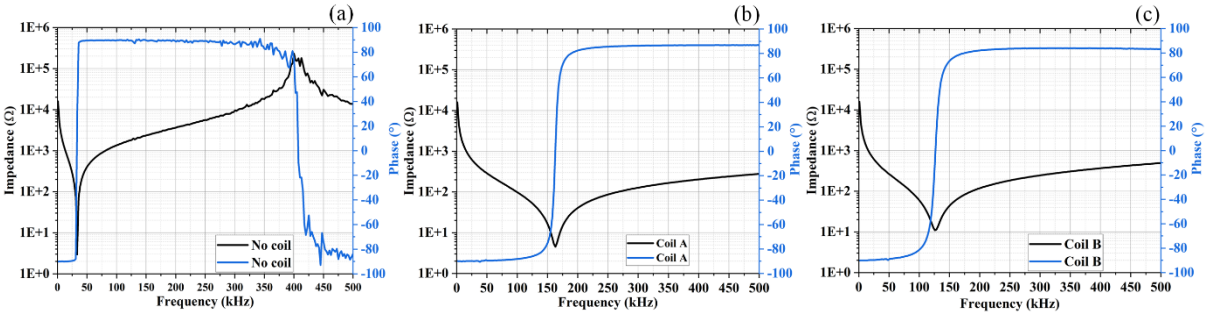

Fig. 18. Impedance and phase characterization of the resonator composed by the transformer and the polypropylene capacitors in a series configuration. (a) The impedance of the resonator in a no-load state. (b) and (c) Resultant impedance with a load using coils A and B, respectively.

Indeed, it is crucial to highlight that the impedance graphs of Fig. 18, in every scenario, display a characteristic logarithmic transition of impedance closely associated with resonance and the Q_s value. This is a phenomenon whereby the impedance undergoes a sudden change with even a slight alteration in frequency. This sharp transition underscores the system's sensitivity to any fluctuation in the values of the component devices. Such fluctuations could be brought about by various factors, including heating or changes induced through actions like switching in the stimulator coil or any other component. In such circumstances, the resonant frequency will need to be rectified. If overlooked, it may potentially lead to a notable drop in the performance of the resonant inverter. To solve this issue, one plausible solution that could be considered is the application of a phase-locked loop (PLL) to the frequency signal source

[89]. A phase-locked loop is an electronic system with a voltage or digital phase comparator, a low-pass filter, and a voltage-controlled oscillator structured in a feedback loop [106, 107]. It locks the phase of the output signal in sync with the input signal's phase, making it an ideal solution for maintaining stability at the resonant frequency and preventing performance degradation.

Fig. 19 shows thermal images captured after 5 minutes of operation, illustrating the heating patterns of both coils. In Fig. 19(a), it is evident that the center of coil A exhibits more pronounced heating compared to the surrounding regions. This effect can be attributed to the autoinduction phenomenon occurring between the outer and inner turns of the coil.

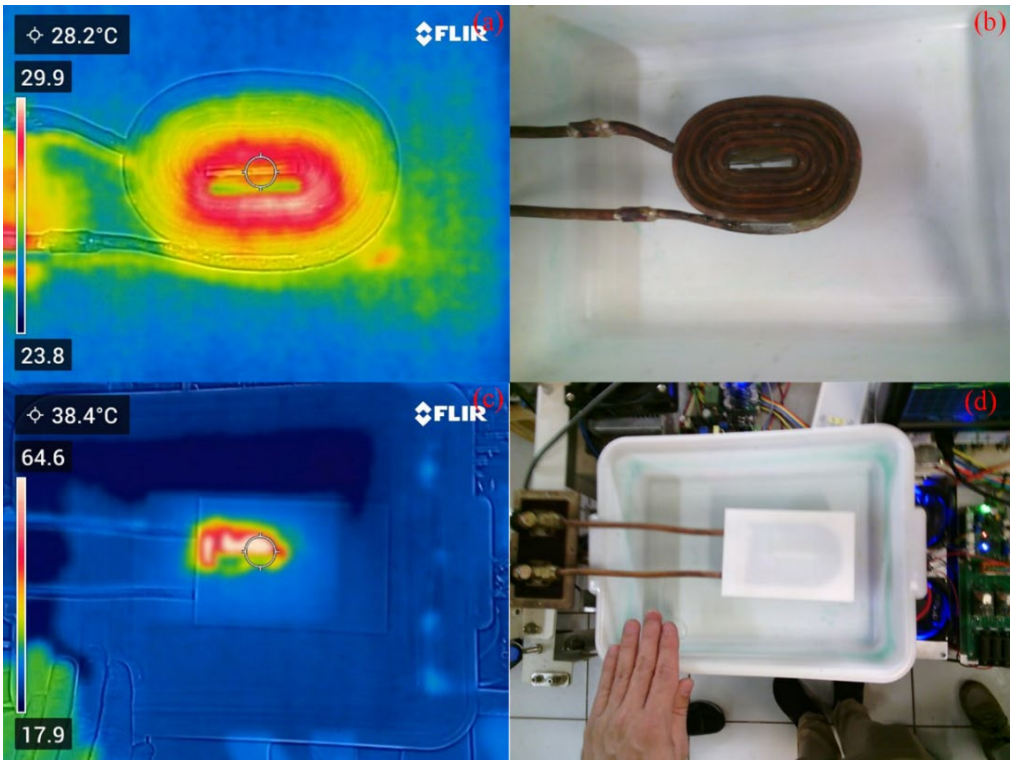

Fig. 19. Heating profiles within the coils observed during the utilization of the resonant inverter. (a), (c)Thermal images of coils A and B, respectively. (b), (d) Photograph of the setup used to acquire the thermal images of coils A and B, respectively.

The temperature distribution observed for coil A remained constant during 20 minutes of operation without significant variations, demonstrating stable performance. In contrast, Fig. 19(c) reveals non-uniform heating across the entire surface of coil B, which poses a leak risk due to a possible melt of the water-encapsulated case, depicted in Fig. 19(d). In addition, the temperature on the case exceeded 60 °C, suggesting that the internal temperature exceeded this value, leading to a significant loss of conductivity due to material overheating. Consequently,

the current configuration of coil B proved to be unsuitable for use in the MH system due to its thermal instability.

Fig. 20 shows the resonator waveforms obtained when connecting coil A to the system. The full-bridge voltage is displayed in Fig. 20(a) as the starting point for the resonator analysis. It is important to note that, due to the switching action and characteristics of the power electronic devices (IGBTs), there is inherent ripple and switching noise present in the full-bridge voltage output. In addition, during the transition between the ON and OFF states of the power electronic switches, there is a finite time for the switch to change its state, resulting in switching transients. These transients introduce high-frequency components into the output voltage, causing ripple and noise. However, in our design, the resonant charge minimized these undesired effects, ensuring a stable and reliable output voltage.

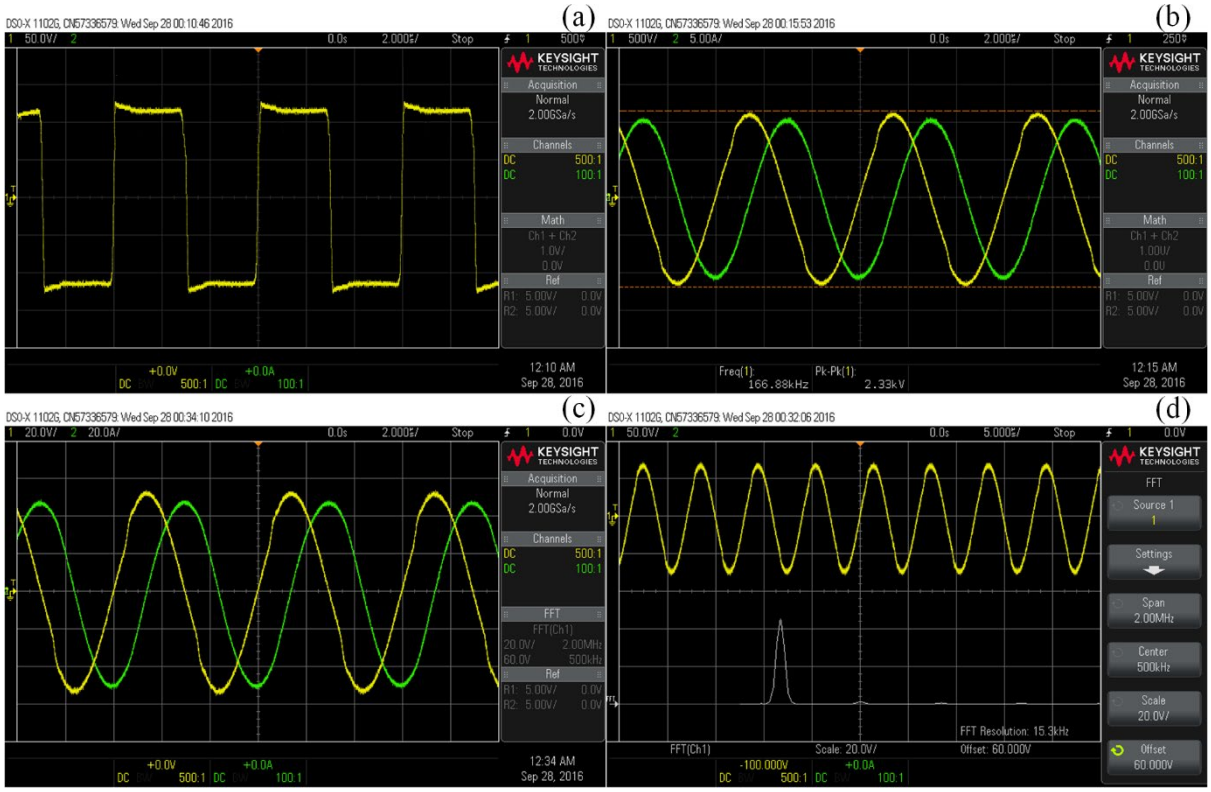

Fig. 20. Resonant inverter output waveforms. (a) Voltage signal obtained from the full H-bridge utilized. (b) Stress voltage on coil L_s and the current of all resonator elements are evaluated at 40% of their capacity. (c) Transformer output voltage and current, with coil A as the load, in a power of 25%. (d) Total Harmonic Distortion (THD) calculation using the Fast Fourier Transform (FFT) feature of the oscilloscope.

Fig. 20(b) shows the voltage gain of the inverter, measured at 120 V_{pk}. The L_s coil experienced a stress level of approximately 1.16 kV_{pk} at 40% of the total power. The evaluation at this power level primarily focused on assessing the voltage limit that the differential probe

can handle in terms of its operational lifespan. The observed voltage gain aligned with the earlier calculated value Q_s = 10. In addition, the presence of a pure sinusoidal voltage in the output waveform is a positive indication that effective filtering has been applied to the square wave output of the inverter, resulting in the removal or suppression of higher-order harmonic components. This suggests that the primary winding's sinusoidal wave is expected to produce a similar response to the secondary winding. In Fig.20(c), the current and voltage of the output transformer winding are depicted, providing further evidence for the aforementioned statement. It can be observed that the current in coil A is predominantly influenced by the interaction between the output voltage and the coil impedance at 166 kHz, as shown in Fig. 17(c). Finally, but not less importantly, the results obtained are also critical for setup animal studies because they indicate that animals as operators should be electrically isolated from the stimulation coil for a safe treatment.

B. MH experiments

The development of the resonant inverter has not only prompted a comprehensive analysis from both mathematical and electrical perspectives, but it has also led to the objective of experimentally evaluating the resonant inverter in the context of nanoparticle heating. This evaluation serves as an initial step toward obtaining curves for estimating the SLP values. Fig. 21 illustrates the heating extending throughout the entire coil A' x-axis of MNPs when exposed to a magnetic field of 166 kHz.

In Fig. 21(a), a thermal image capture is exposed, wherein the heating exhibited a non-uniform pattern for all samples, possibly for a delayed convective effect, but showing the heating behavior of volumetric samples. In addition, sample M1 has a slightly lower concentration of heat in comparison to the M3 sample, which was positioned on the other side from the center sample. However, this slight decrease in heating observed is possibly due to a minor positioning error concerning the ellipsoidal focus of the coil. It is worth noting that the initial ambient temperature of the samples, around 23°C, increased to an average temperature of 38°C within approximately 18 minutes. This validates the system's capability to heat MNPs volumes outside the coil effectively. Furthermore, with MH treatments, concentrations

typically exceed 2% [21, 90, 108], often peaking at around 15% [8, 9, 109]. This implies that the heating effect of MH treatment can be amplified when using our device, particularly with MNPs concentrations surpassing 2%. Consequently, this system harbors substantial promise for MH applications in simulated models (phantoms) and small-scale animal subjects.

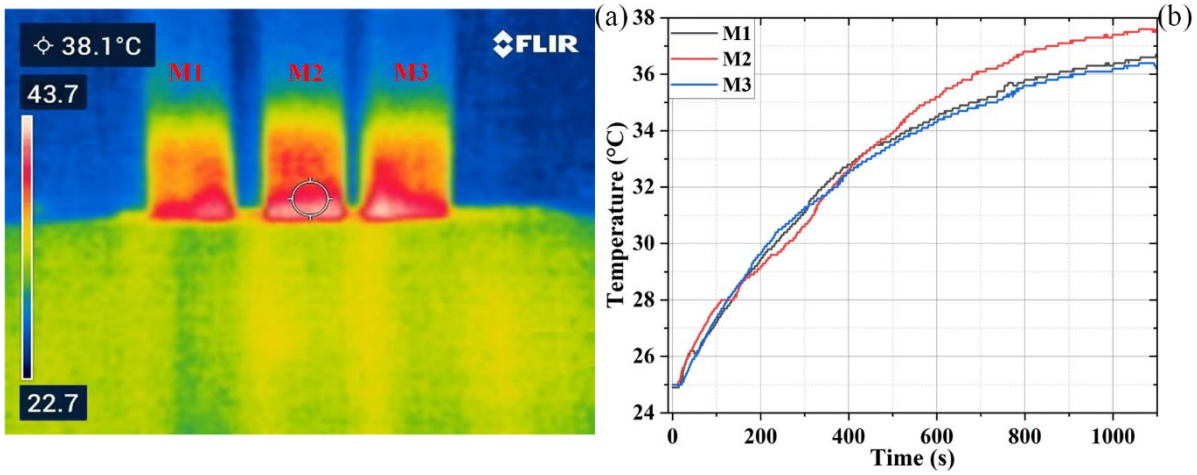

Fig. 21. Temperature evaluation of MNPs samples heated with the designed MH system generating a maximum magnetic field amplitude of 28 kA/m. (a) A thermal image capturing the cuvettes containing MNPs samples. The image provides visual insight into the temperature distribution at the sample surface. (b) Measured temperature variation inside the cuvettes using a fiber optic thermometer.

Fig.21(b) shows the temperature variation within all three samples, measured using a fiber optic thermometer. This approach ensures an accurate assessment of the temperature values. However, the results were different toward the thermal image capture, principally due to the thermal camera emissivity (ε) factor, which was adjusted at 0.90, and should be compensated for cuvette emissivity [84]. Despite these variations, it is worth mentioning that the observed differences in the results are not significant in terms of the overall temperature distribution. The variations primarily affect the temperature values themselves rather than altering the underlying temperature distribution within the samples. It is essential to consider that the thermal scale adjustment impacts the absolute temperature values obtained from the thermal image capture but does not affect the overall understanding of the temperature distribution across the samples.

concentration and amount of MNPs used in aforementioned samples. Finding that the SLP values will decrease for volumes superior to 1 cm^3 because the amount of total MNPs' mass is more significant. In addition, it is essential to note that the Box-Lucas analysis is an approximation and relies on certain assumptions. These assumptions include assuming a well-mixed fluid environment, neglecting radiative heat transfer effects, and assuming steady-state conditions. Despite these simplifications, these results comprehensively analyze the developed system's heating capabilities and potential applications for MNPs

Conclusions

A high-frequency magnetic field generator was designed and built specifically for MNPs heating. The development of this system involved the careful analysis of multiple parameters, including the magnitude of the magnetic field, impedance, coil design, and dynamic cases for different load conditions. In addition, the full-bridge topology of the resonant inverter contributed to achieving a magnetic response that more closely resembles a pure sine waveform, which can be an essential behavior when the resonant inverter works for prolonged periods. However, it is vital to indicate that this MH system can be improved by implementing a PLL on the frequency signal source for the long stability of the resonant inverter.

As a result, the generator was tested for heating MNP in a concentration as low as 2%, using magnetic fields of 15 kA/m at 166 kHz for 18 minutes, using 40% of the inverter's power capacity reaching temperatures up to 38°C, which means that for possible complete power application, the heating will be more intense and the effectiveness have to be evaluated. To end this, the planar ellipsoidal-planar coil used by the resonant inverter as a continuous power supply showed an exceptional ability for heating volumetric MNPs samples along the *x-axis,* reaching a relatively homogeneous in volume heating, which supposes a significant improvement for preparing the system for theranostic experiments with MMUS because the coil fits the shape of a linear ultrasound transducer completely and achieves enough magnetic field strength for MNPs heating.

Chapter 4: Development an automated theranostic platform

Introduction

The field of personalized medicine has witnessed remarkable advancements in recent years, paving the way for more effective and precise approaches to patient care across various disease treatments. One area where these advancements are particularly noteworthy is in the treatment of complex diseases, including cancer. Researchers and clinicians have recognized the importance of integrated platforms that combine diagnostics and therapeutics into a unified framework [19, 21, 110, 111]. This integration can catalyze significant transformation in healthcare by facilitating the implementation of targeted treatments specifically tailored to individual patients.

Theranostic platforms encompass diverse technologies, ranging from nanoparticles and molecular imaging agents to advanced drug delivery systems and gene therapies [18]. These platforms provide a unique opportunity to simultaneously diagnose diseases, monitor treatment response, and deliver therapeutic interventions with enhanced precision. By integrating these approaches, theranostics aims to overcome the limitations of conventional treatments, improve patient outcomes, and minimize adverse effects [112].

Magnetic hyperthermia (MH) is a therapeutic approach that utilizes magnetic nanoparticles (MNPs) to generate localized heat within tumor cells [7-9]. These nanoparticles, when exposed to a high-frequency alternating magnetic field, produce heat through hysteresis and relaxation mechanisms [37, 64, 78]. This targeted heat generation can lead to several beneficial effects, including direct tumor cell destruction, enhanced drug delivery, and synergistic interactions with traditional approaches such as chemotherapy and radiotherapy [17]. To enhance the efficiency of MH, MNPs can be guided to the target tissue (e.g., a tumor) using an external magnetic field, which allows for more localized treatment and can help to minimize damage to healthy tissues [21].

Although MH is widely recognized as a promising adjuvant therapy in the treatment of cancer, significant challenges still hinder this method to be effectively translated into clinical practice. One crucial challenge is the precise heating control during MH [113, 114]. Maintaining the optimal temperature is vital as excessive heat can harm healthy tissues, while

insufficient heat may not effectively kill tumor cells. Therefore, achieving accurate intertumoral temperature control requires effective temperature monitoring throughout the procedure. Currently, clinical investigations of MH have primarily relied on the insertion of one or more fiber-optic thermometers into the treated region [115]. However, this approach has limitations as it offers data from a restricted number of points within the three-dimensional temperature distribution and involves invasive procedures that are less desirable. Alternatively, thermographic cameras have emerged as a new approach to intertumoral thermal estimation [83, 116]. Initial experiments using this method have shown promising real-time outcomes in studies conducted on living mice [84]. However, this method is mainly suitable for superficial tumors, and incorrect implementation can lead to significant errors in temperature determination within the specific region of interest (ROI) [84].

Ultrasound and thermoacoustic techniques present alternative noninvasive imaging methods for monitoring thermal therapy outcomes, including temperature, tissue elasticity, and tumor vascularization, and can be integrated into theranostic platforms [21, 117-120]. These methods exploit the fact that temperature elevation induces diverse alterations in tissues' elastic and acoustic characteristics. For example, the temperature-induced fluctuations in the speed of sound lead to time-delayed echoes in the backscattered signals [121], enabling the mapping of tissue temperature variation. Additionally, ultrasonic approaches can monitor changes in tissue elasticity, serving as an indicator of temperature variations during the procedure [52, 122]. Finally, photoacoustic imaging has been investigated as a potential method for mapping temperature and tumor vasculature changes [119].

Another noteworthy challenge in the clinical translation of MH is the efficient localization of MNPs within the tissue. Studies have demonstrated the efficient localization of MNPs using magnetic resonance imaging (MRI) [123] and magnetic particle imaging (MPI) [124]. For example, superparamagnetic iron oxide nanoparticles (SPIONs) located within tissues manifest as dark regions in the MRI images, indicating the presence of the MNPs [125, 126]. MPI analyzes the nonlinear magnetization response from MNPs, enabling precise distribution and concentration localization [127, 128]. However, integrating these techniques

with MH poses challenges primarily due to their high cost and the lack of efficient integration. Despite mainly being based on magnetic field utilization, these approaches require distinct setups and operating conditions. For example, the intense and static magnetic field in MRI can affect the magnetic properties of MNPs and impede their ability to generate heat efficiently. On the other hand, recent publications have reported promising results in integrating MPI with MH, achieving efficient MNP localization and selective MH application to specific ROIs in mice [129].

Magnetomotive ultrasound imaging (MMUS) is another technique developed to localize MNPs within the tissue. MMUS operation is based on MNPs displacement detection produced by a strong magnetic field gradient [29, 43, 52, 69, 130]. This magnetic field interacts with MNPs; once the magnetic field is applied, an ultrasound transducer emits high-frequency sound waves into the tissue to generate ultrasound images used, through specialized motion tracking algorithms, to detect micrometer changes in the tissue surrounding of MNPs. Using the temporal behavior of these displacements, inverse problems can be used to detect MNPs distribution and concentration [42, 131]. In addition, the MMUS systems' portability and easy execution (see Chapter 2) make it an excellent choice for MH as a diagnostic method.

Magnetomotive ultrasound imaging (MMUS) is another technique developed for localizing magnetic nanoparticles (MNPs) within a tissue [29, 30, 43, 52, 58, 70, 130, 131]. By leveraging an intense magnetic field gradient, MMUS detects the displacement of MNPs. Once the magnetic field is applied, an ultrasound transducer emits high-frequency sound waves into the tissue, generating ultrasound images that can be processed using specialized motion tracking algorithms to identify micrometer-scale displacements in the surrounding tissue where the MNPs are located. Utilizing the temporal behavior of these displacements, inverse problems can be solved to determine the distribution and concentration of MNPs [42, 131]. Furthermore, the portability and ease of use of the MMUS system (as discussed in Chapter 2) make it a potential diagnostic tool for MH.

A theranostic platform [21] was developed in a previous study to integrate MMUS and thermal ultrasound imaging with MH. An interesting aspect of this platform was the utilization

of a single excitation coil for both MMUS and MH applications. The theranostic system exhibited promising results in phantom experiments by successfully mapping the location of MNPs and generating two-dimensional temperature maps during the MH procedure. However, despite these achievements, some remaining challenges persisted, impeding the pre-clinical implementation of the platform. One technical limitation of the platform described in [21] was the absence of automated switching between the magnetic fields used for MMUS and MH, preventing real-time acquisition of MMUS images during MH. Additionally, the design presented in [32] lacked the required power to conduct a comprehensive MH procedure in large-volume phantoms or potential animal applications, primarily due to its original focus on MNP characterization [32].

This chapter presents a method to integrate the MMUS and MH systems, which were previously described in chapters 2 and 3. The main goal was to establish a versatile theranostic platform capable of automatically switching between high-frequency and pulsed magnetic fields, which are used for MH and MMUS, respectively. In addition, it is provided a detailed description of the platform's design, including the steps involved in the development of the system and the strategies used to enhance its capabilities. This comprehensive discussion sets the foundation for understanding how this platform enables both MH and MMUS functionalities. Furthermore, a series of preliminary experiments were conducted to evaluate the integrated system, including magnetic field characterization, MMUS imaging of tissue-mimicking phantoms, and analysis of MMUS displacement behavior during an MH experiment. Finally, the remaining challenges and potential future directions are discussed.

Materials and methods

A. Combining MMUS and MH systems

Combining MMUS and MH techniques into a theranostic system poses a significant challenge in generating and synchronizing two types of magnetic fields within a single system. These magnetic fields are interleaved and applied concurrently, using a single inductor for both purposes. This integration requires careful design and control to ensure the efficient operation of both techniques. As discussed in Chapter 1 and Chapter 3, MH typically operates within a

100 - 500 kHz frequency range, while MMUS demands a lower frequency magnetic field (<100 Hz). This lower frequency requirement for MMUS is due to the elastic response of tissues. Overcoming this technological challenge requires the utilization of electromagnetic coupling, as depicted in Fig. 22.

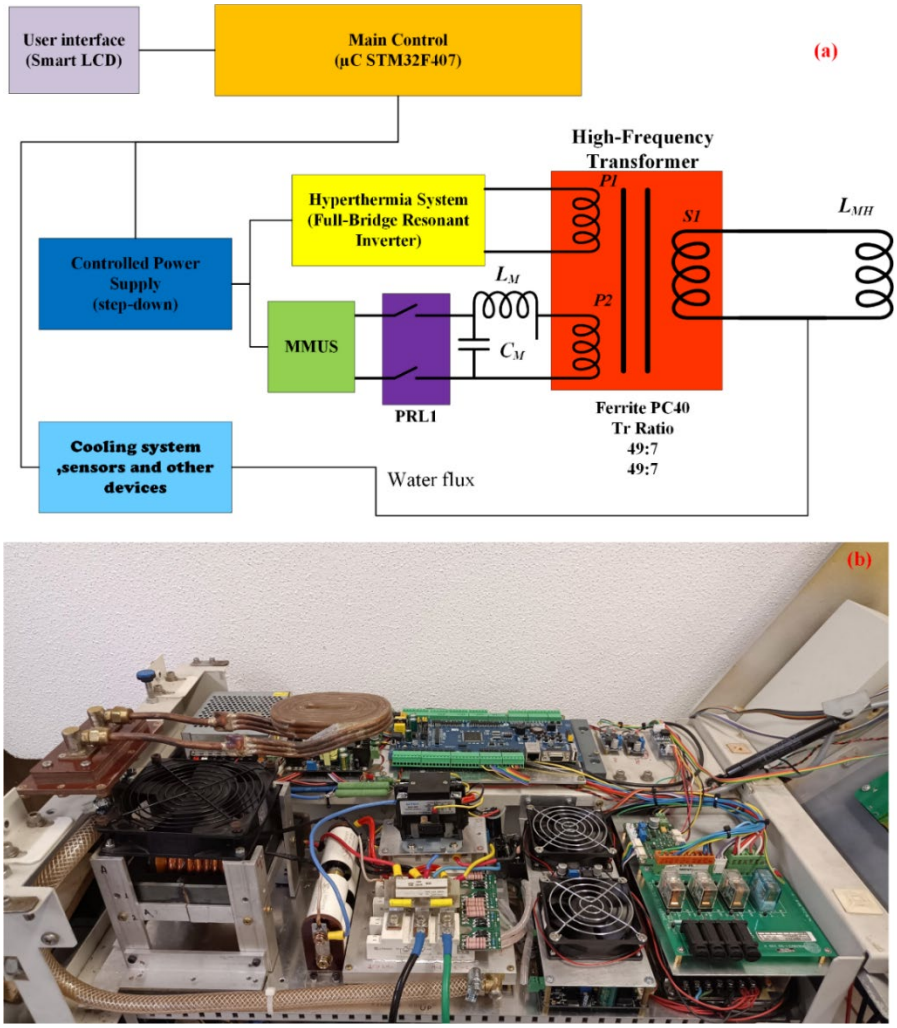

Fig. 22. Automated theranostic platform combining MMUS and MH. (a) a schematic block representation of the theranostic platform. (b) A photograph of the implemented circuitry used for the theranostic platform.

The MH device described in Chapter 3 served as the base for implementing the theranostic platform. To enable the integration of MMUS capabilities, an additional primary winding (P2) was added to the high-frequency transformer, as shown in Fig. 22(a). Unlike the Litz wire used in the original primary winding (P1), the new winding was constructed using 18 AWG copper wire. For the MMUS excitation module, the capacitor discharge system, as discussed in Chapter 2, was employed based on the Faraday-Lenz principle, which requires a time-varying magnetic field for successful magnetic induction. Although the pulsed MMUS

system designed with an inverter offered several advantages over the capacitor discharge system, it has limited compatibility with an MH coupling induction device (transformer). To overcome this limitation, the system described in Fig. 4(a) of Chapter 2 was implemented. In the present configuration, the output terminals of the MMUS system were connected to the new primary winding P2 of the transformer instead of directly to the excitation coil. This setup enabled the generation of magnetic field pulses of up to 2 ms.

Meeting the requirements of the present application, additional components were necessary for the development of the theranostic platform. One addition was the installation of a power contactor, PRL1, which served as a decoupling stage between the MMUS pulse generator and the transformer. This addition was explicitly necessary for the present application, as the system operated in MH mode, where the P2 windings of the transformer acted as an output. Since P2 windings had the same number of turns as P1, they experienced voltages comparable to those encountered by P1 during resonance, exceeding 1000 VAC. Ordinary semiconductor arrangements connected to P2 would not be able to withstand such high stress. Therefore, the inclusion of the contactor PRL1 was necessary to ensure the safety and proper functioning of the MMUS system within the theranostic platform, which was not a feature of the system described in Chapter 2.

Following the aforementioned modifications, the inclusion of components C_M (CDET 943C20P1K-F 0.1UF 2000V) and L_M (150 µH, PQ5050 core for 100A) between the PRL1 contactor and the P2 winding served as a matching circuit in the system. This circuit serves two main purposes. In MH mode, where frequencies reach hundreds of kHz, the L_M inductor works as a high-impedance element connected to a capacitor (a low-impedance component at high frequencies). This configuration acts as a high-voltage filter, providing stability against high-voltage sparks that may occur. Conversely, in MMUS mode, these elements exhibit an inverse impedance behavior. In this case, the L_M inductor serves as a current limiter for the MMUS pulse, preventing excessive current flow through the transistor used for generating the excitation. This allows the energy source to transmit the majority of energy without exceeding the current limits of the transistor. In addition, C_m acts as a charged capacitor, effectively open-

circuiting itself to facilitate the flow of pulsed current.

Finally, Fig. 22 (a) illustrates essential additional system modules that enable the efficient operation of the diagnostic platform. At the core of these modules is the control unit, which operates using an ARM family microcontroller (this module will be discussed in more detail in the following section). The microcontroller establishes direct or indirect connections with the cooling system, sensors, and the power source, which supplies both the MH and MMUS modules. Fig. 22 (b) shows a photograph of the complete system assembly.

B. Digital control system

Integrating microcontrollers is an optimal solution for the theranostic system, which requires precise synchronization of events within calculated intervals. This cost-effective and efficient solution not only meets but surpasses the demanding requirements of safety, processing power, and overall system performance. The solution leverages the capabilities of the STM32F407ZGT6 model, a high-performance 32-bit microcontroller integrated into a robust, industrially-designed development card (refer to supplementary material 4 for detailed information). The main control module follows the block diagram depicted in Fig. 23, ensuring access to every module of the theranostic system. By using a real-time operating system (FreeRTOS) and 16 interruption levels, the microcontroller efficiently communicates with each module, assigning specific hardware addresses based on their bus protocols.

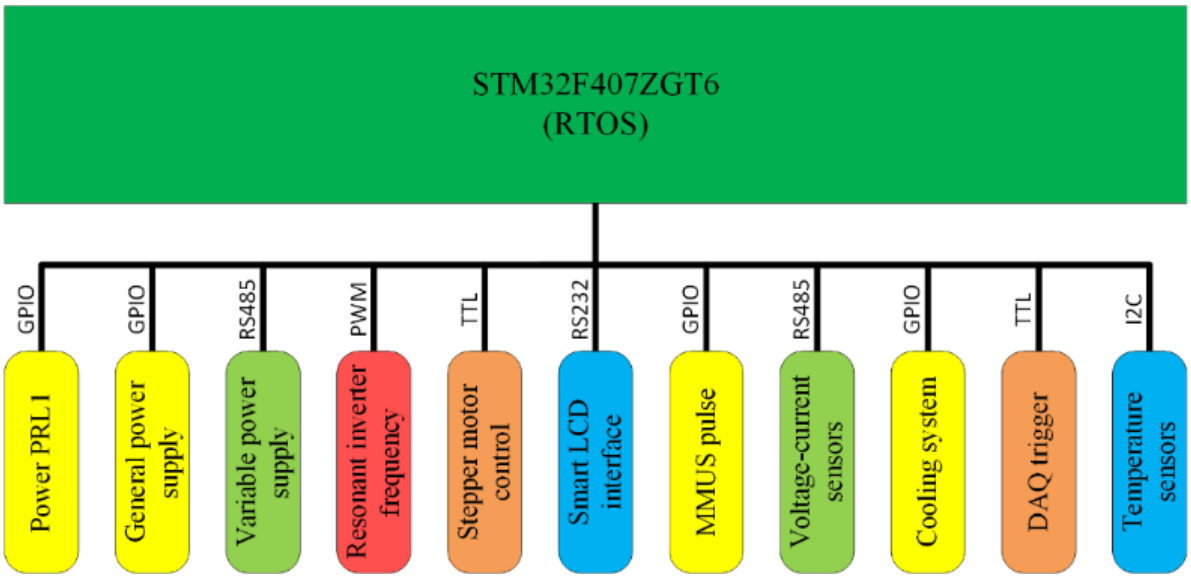

Fig. 23. The main control module, a 32bits microcontroller, is used to communicate with all theranostic platform individual modules using GPIO and bus protocols.

C. Cooling module

Additional modules were implemented to enhance the platform's performance, including the integrated cooling module, as shown in Fig. 24. The components of the implemented chiller include a pump, radiator, and heat exchanger. The cooling module operates by circulating the refrigerant liquid through heat exchangers that come into contact with the components requiring cooling, such as the IGBT modules, transformer, and excitation coil. The liquid refrigerant then flows through the radiator equipped with a cooling fan. As the radiator absorbs heat from the fluid, the fluid cools down before being recirculated back to the reservoir or water tank, starting a new cycle.

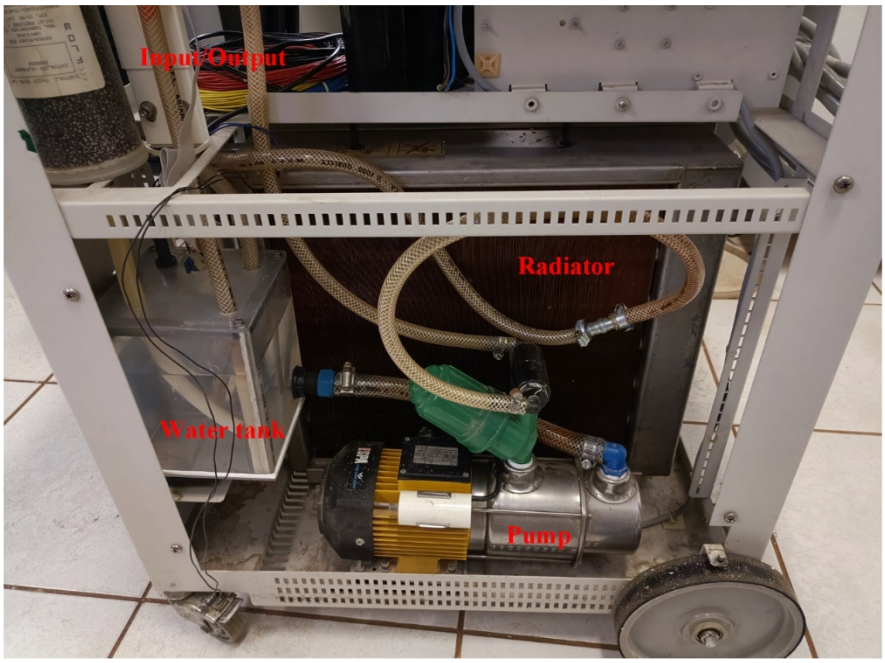

Fig. 24. The theranostic cooling module comprises a ½ H.P. connected to a small water tank. The pump delivers water directly to the heat exchangers, which are attached to the electric components for cooling purposes. Once the cooling process is complete, the water returns and enters the radiator. Ultimately, the water completes the cycle by returning to the small tank.

D. 3D scanning module for MMUS imaging

This module consists of two mechanical translating stages employed to generate three-dimensional MMUS images, as illustrated in Fig. 25. The first system is a manual raster configuration attached to the ultrasound probe support (blue box). This system serves two primary functions: it holds the ultrasound probe and allows manual positioning to align with the center of the excitation coil. Although it lacks automation, this system offers good mobility, providing flexibility during operation. In contrast, the second raster system (yellow box)

features complete automation. It is a sliding table that employs a stepper motor (model 7HS08-1004S) as the actuator responsible for moving the phantom perpendicular to the ultrasound probe. Controlled by the microcontroller, the stepper motor interfaces with an Easy Driver V4.4 A3967, which ensures precise operation with a minimum resolution as fine as 0.01 mm. This automated positioning functionality enables the generation of volumetric images while mechanically insulating the phantom from the excitation coil. This insulation ensures clean image quality by reducing noise and prevents heat transfer from the coil to the phantom.

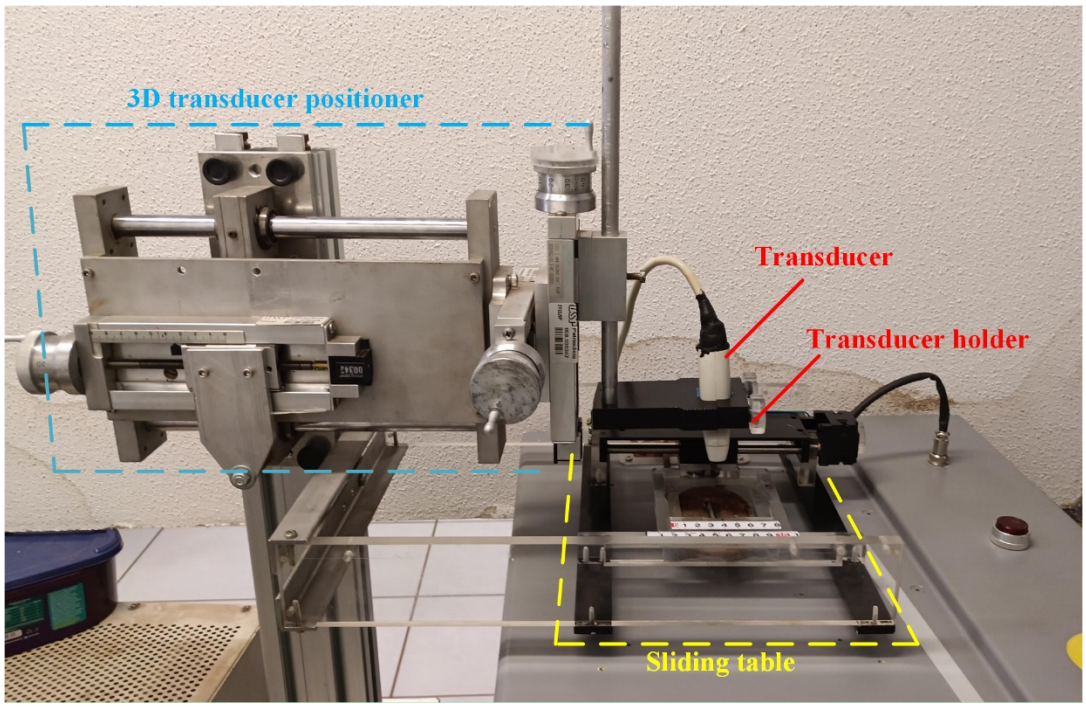

Fig. 25. The scanning module can be used to create 3D MMUS imaging. This module comprises a 3D holder for the medical ultrasound transducer and a second system for phantom movement.

E. Phantom preparation

To assess the performance of the theranostic platform, two cubic tissue-mimicking phantoms containing inclusions labeled with MNPs were prepared. The shape specifications of the phantoms are depicted in Fig. 26. The first phantom was prepared containing a hemispherical inclusion with a radius of 7.5 mm, as illustrated in Fig. 26(a). The second phantom was created to have three cylindrical inclusions with 3 mm radius x 7.5 mm height, as shown in Fig. 26(b). These inclusions were strategically positioned to cover the ultrasound transducer's entire lateral field.

c

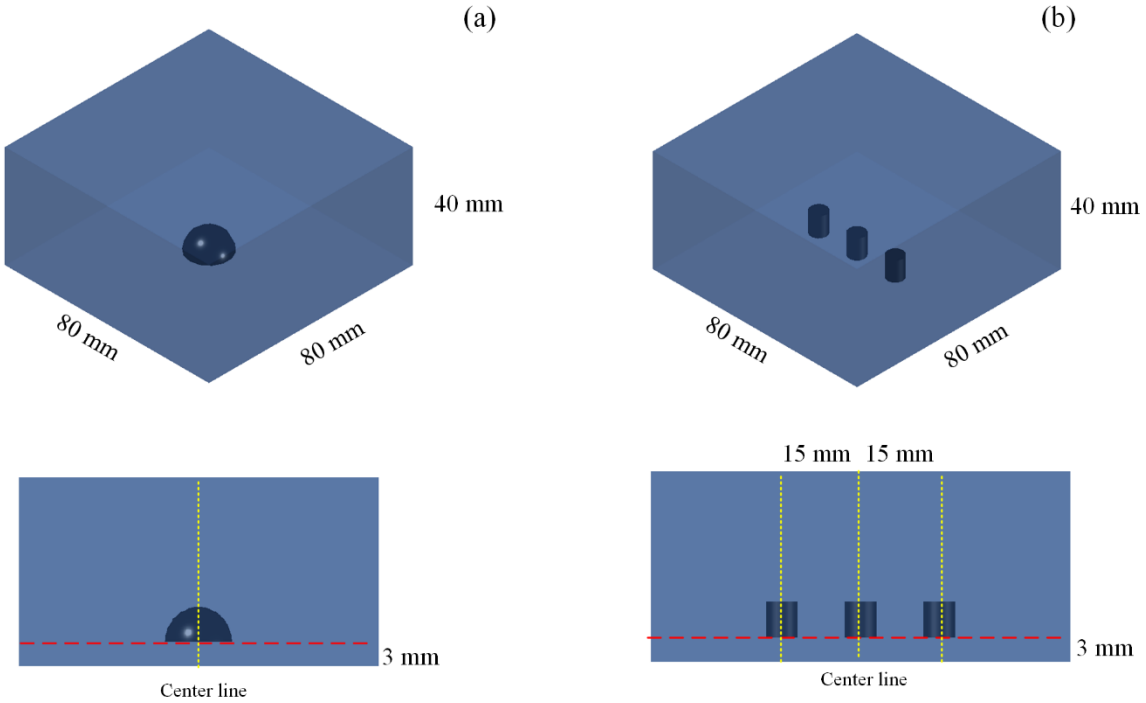

Fig. 26. Tissue tissue-mimicking phantoms used to evaluate the performance of the theranostic platform. (a) Phantom prepared with a hemispherical inclusion. (b) Phantom containing three cylindrical inclusions separated by 15 mm between each other, strategically positioned to conver the entire lateral field of view of the ultrasound transducer.

The phantom material was prepared by dissolving 5% bovine gelatin (Bloom 250, Gelita, Sao Paulo, Brazil) and 2% Agar (HiMedia, Mumbai, India) in Milli-Q water at 90°C. Agar and gelatin are commonly used materials for simulating soft tissue due to their comparable acoustic and elastic properties [66, 67]. The solution was heated and stirred magnetically for 1 hour to ensure homogenization until it reached a temperature of 90 °C. Subsequently, the mixture was cooled to 36 °C, and 0.2% formaldehyde (Synth, São Paulo, Brazil) was added. The molten agar-gelatin mixture was poured into an 80 mm x 80 mm x 40 mm mold and allowed to cool and solidify overnight at 5 °C. The same procedure and materials were used to create the inclusions and background. The phantom material used to make the inclusions was labeled with zinc-ferrite MNPs ($Zn_{0.1}Fe_{0.9}Fe_2O_4$) at a weight concentration of 2% [30]. The MNPs had an average size of 12 nm and a saturation magnetization of 83 emu/g. The reader is referred to [67, 68] for more details about the MNPs synthesis and characterization.

F. Magnetic field characterization

For this purpose, the stimulation coil was driven by a 2 ms pulsed current with a magnitude of 2.16 kA. This high-level current was chosen to determine the maximum magnetic

field capacity that is possible to generate with this coil. The magnetic field amplitude was measured using a Gaussmeter (TMAG-1T model from Globalmag, a reputable manufacturer based in Cotia, SP, Brazil). The magnetic field per ampere produced by the coil was calibrated, establishing a relationship between the input current and the resulting magnetic field. To map the spatial distribution of the magnetic field, the Gaussmeter probe was attached to the manual scanning system depicted in Fig. 25.

G. MMUS imaging

2D MMUS images were obtained for both phantoms. An ultrasound imaging system connected with a parallel data acquisition system (SonixDAQ, Ultrasonix), and equipped with a linear array transducer (L14-5/38), was used. The ultrasound echo data acquisition, at a frame rate of 4 kHz, was synchronized with the high-intensity pulsed magnetic field.

The ultrasound images were used to track the displacements resulting from the interaction between the external magnetic field and MNPs. This tracking was achieved using a cross-correlation algorithm applied to the successive ultrasonic backscattered RF data. The algorithm was specifically designed to handle the data obtained from the system, allowing for the creation of 2D MMUS images. Additionally, the sliding table module was used to create 3D MMUS imaging. Initially, the manual positioning system aligned the ultrasound probe with the center of the excitation coil. Subsequently, the automated translational stage, driven by a stepper motor, facilitated the movement of the phantom or tissue being examined. This enabled the acquisition of multiple 2D MMUS images at different spatial positions, which were then compiled and reconstructed to produce a volumetric 3D MMUS rendering using the software 3D Slicer.

H. Preliminary experiment to evaluate the theranostic platform

To understand the performance of the developed theranostic platform in acquiring MMUS images during an MH procedure, a similar experimental setup, as described in section G of this chapter, was employed. In this particular case, a fiber-optic thermometer probe (Qualitrol NOMAD-Touch Portable Fiber Optic Monitor) was positioned within the hemispherical inclusion of the phantom, as depicted in Fig. 27. The phantom was positioned

on a dedicated sample holder designed to ensure a distance of approximately 0.5 mm between the phantom and the coil, effectively preventing direct contact between them.

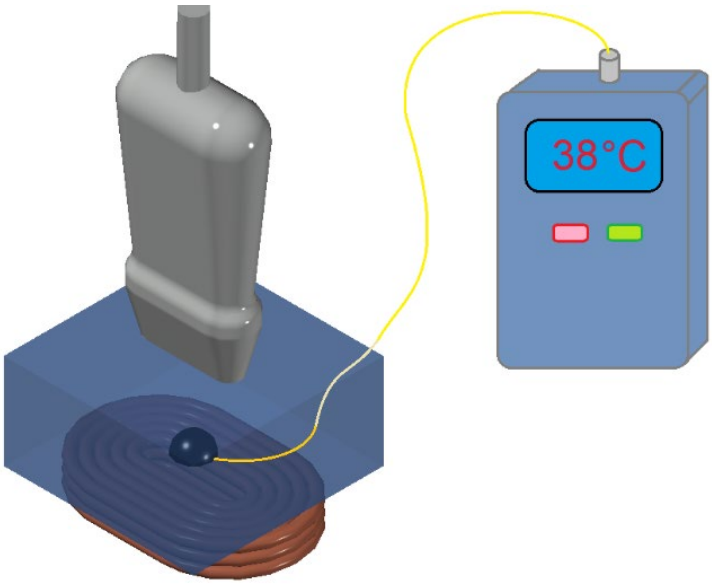

Fig. 27. Theranostic setup used to evaluate the capability of the system for acquiring MMUS images during the MH procedure. The stimulation coil generates the magnetic field required for MH therapy and MMUS imaging. An optic fiber thermometer was positioned within the inclusion of the phantom to monitor the temperature.

The experiment started by acquiring MMUS images before activating the MH magnetic. These initial data served as a reference point for the subsequent displacement measurements. Afterward, the system switched to MH mode, which lasted for 23 minutes until another programmed transition occurred, returning to MMUS imaging. During this cooling phase, a series of MMUS images were acquired to gain valuable insights into the behavior of the phantom at different temperatures induced by MH therapy. Throughout the experiment, temperature data were recorded using the fiber-optic thermometer probe.

Results and discussion

A. Magnetic field characterization

Fig. 28 shows a detailed analysis of the magnetic field magnitude generated during pulsed current stimulation of 2.16 kA. The experimental results show a maximum magnetic field strength of 258 mT. The magnetic field distribution along the *x-axis* exhibited a nearly trapezoidal shape, as illustrated in Fig. 28(a). This profile is particularly beneficial as it ensures comprehensive coverage of the ultrasound transducer lateral field of view. In addition, two

distinct peaks in the magnetic field can be observed, located approximately 20 mm from the central axis of the coil. These peaks correspond directly to the ellipsoid shape of the coil, with the foci centers acting as areas of intensified magnetic field.

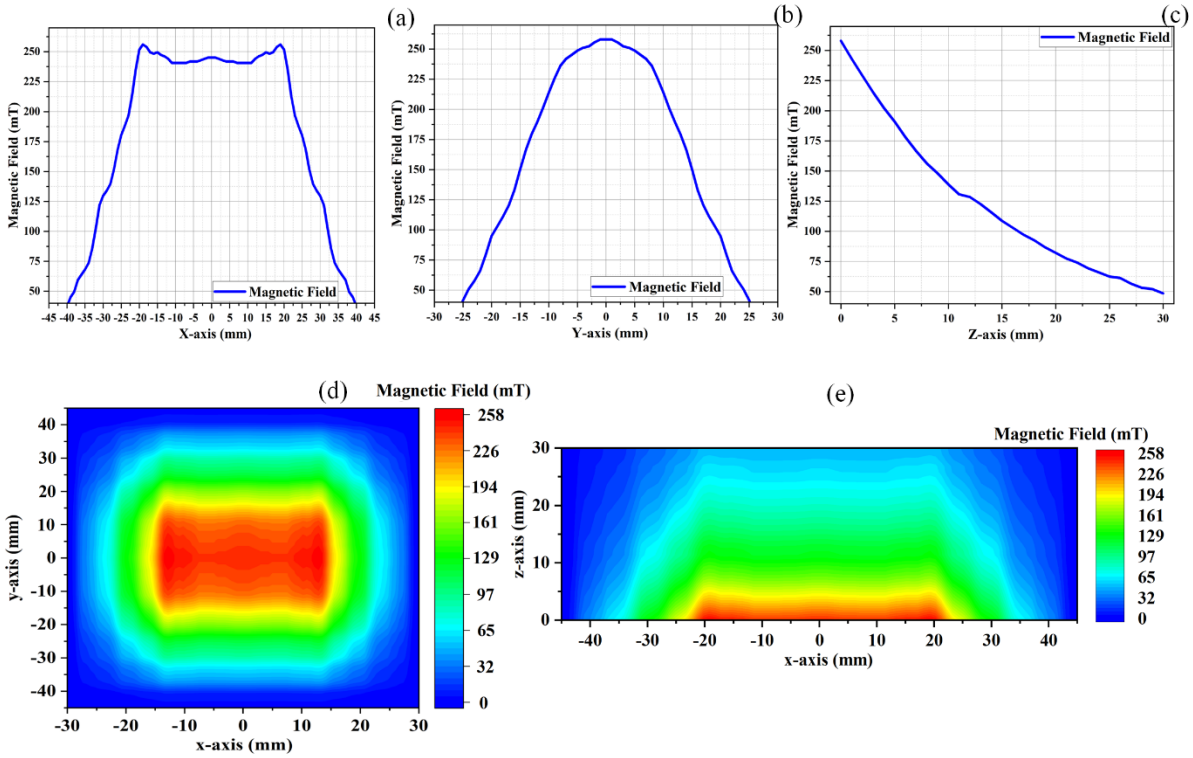

Fig. 28. Magnetic field characterization for coil used in MH and MMUS. (a) The magnetic field measurement at z = 0 mm from the excitation coil along the x-axis. (b) The measured magnetic field on the top of the excitation coil along the *y-axis*. (b) The magnetic field on the coils along the *z-axis*.

Additionally, a less prominent peak is observed at the center of the coil, where the magnetic field maintained a relatively constant strength with only a 4% difference compared to the peak intensity. Upon revisiting the MH experimental results presented in Chapter 3, an apparent disparity was observed between thermal image and fiber thermometer readings concerning the magnetic field along the *x-axis* (see Fig. 21). However, this discrepancy can be explained by considering the spatial positioning of the samples relative to the elliptical foci of the coil. Immediately after these foci, there was a significant decrease in the magnetic field intensity. Specifically, samples M1 and M3 were located at these foci, where the magnetic field reached its peak but also exhibited more expressive non-homogeneity. This abrupt variation in the field intensity can result in reduced heating effectiveness due to the transient nature of the peaks in the magnetic field strength and delays in the thermal convection within the samples. On the other hand, sample M2 was positioned in a more homogeneous magnetic field region.

This allowed for a more homogeneous stimulation across the sample, leading to more consistent and potentially more effective heating. Understanding these positional dependencies can be crucial in optimizing the placement and the overall effectiveness of MH treatment. In addition, this understanding can benefit future experiments in both MH and MMUS, leading to more controlled and predictable heating and displacement profiles.

Fig. 28(b) shows the spatial distribution of the magnetic field along the y-axis. When viewed from this perspective, the ellipsoidal coil exhibited characteristics similar to those of a circular coil. As a result, the magnetic field pattern did not display the prominent trapezoidal transition observed along the *x-axis*. Notably, in this view, an approximate 10 mm region at the center of the coil maintained a relatively stable magnetic field intensity with only a 3% variation. This consistent region provided a "window" where the magnetic field remained sufficiently strong. By considering the contributions along the x-axis and y-axis, defining an appropriate stimulation area is possible.

Another crucial aspect to consider in this study is the penetration depth of the magnetic field. Fig. 28(c) shows the magnetic field profile along the z-axis. From this perspective, the field gradient exhibited a 6.55 mT/mm value, indicating a nearly linear transition. The magnetic field presented a significant contribution from a depth of 5 mm and propagated up to 20 mm. Figs. 28(d) and 28(e) show the spatial distribution of the magnetic field in the x-y plane at z = 0 mm and the x-z plane at y = 0 mm, respectively. These images offer a more comprehensive visualization of the non-homogeneous magnetic field generated by the proposed ellipsoidal excitation coil.

B. MMUS imaging

Fig. 29(a) shows a typical B-mode ultrasound image of the phantom containing a hemispherical inclusion. As previously discussed in Chapter 2, visualizing the inclusion labeled with MNPs using standard ultrasound techniques can be challenging as they can be easily be mistaken for other tissue structures withing the body. However, when the pulsed magnetic stimulus is applied, the resultant peak displacement map [Fig, 29(b)] effectively highlights the location of the MNPs. This is further depicted in Fig. 29(c), where the color-encoded MMUS

images are overlaid on the B-mode image, providing a clear visual representation.

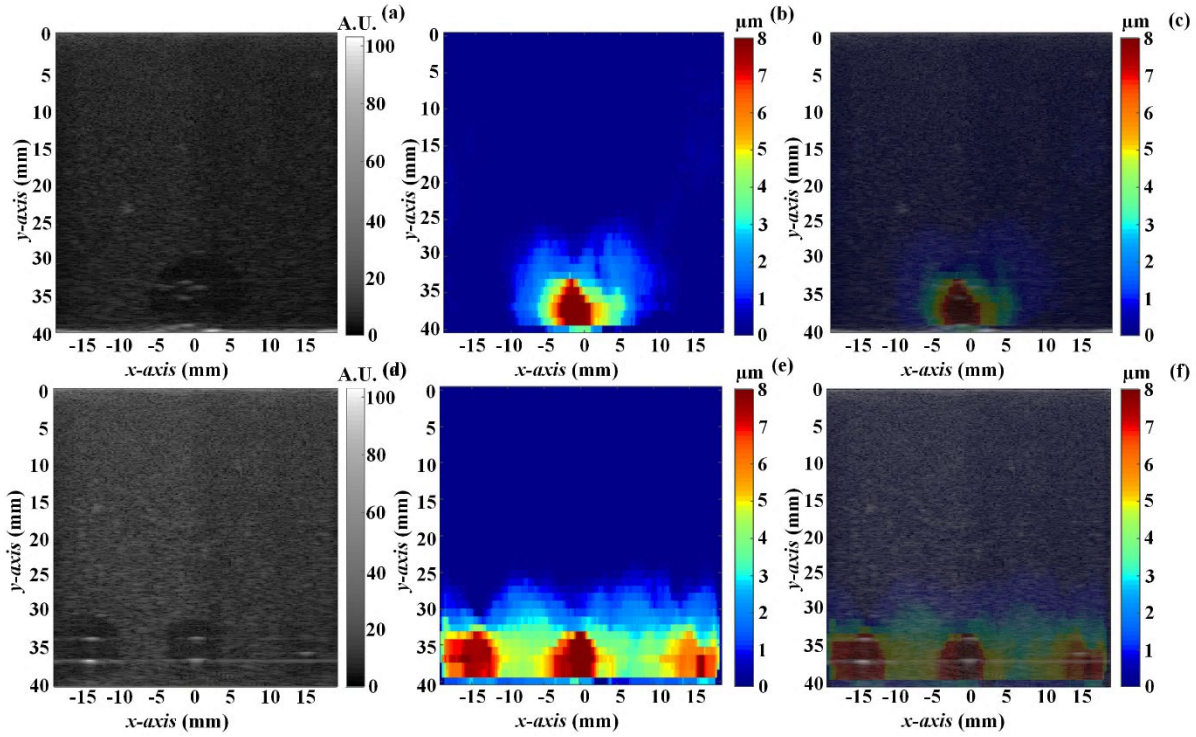

Fig. 29. Pulsed MMUS imaging results obtained from two tissue-mimicking phantoms. (a) B-mode ultrasound image of a phantom containing a hemispherical inclusion. (b) Peak displacement map of the same phantom shown in (a). (c) Color-encoded MMUS images overlaid on the B-mode image, providing a clear visual representation. (d) B-mode ultrasound image of a phantom containing three cylindrical inclusions. (e) Peak displacement map (MMUS image) of the phantom shown in (c). (f) Color-encoded MMUS images overlaid on the B-mode image, providing a clear visual representation of the three cylindrical inclusions is displayed here.

The peak-displacements observed in this experiment (~8 μm) were lower compared to those obtained in Chapter 2 [Fig. 7(b)], where displacements reached up to 30 μm. This difference can be primarily attributed to the strength of the external magnetic field. In the present experiment, a maximum magnetic field of up to 255 mT was achieved, while the magnetic field with a magnitude close to 1000 mT were obtained in Chapter 2. In Chapter 2, the excitation coil incorporated a magnetic field concentrator made of steel in its core, resulting in a more intense magnetic field and magnetic field gradient. However, including a core within the stimulator coil is not feasible for MH applications in this dual-purpose theranostic system, as it can lead to an elevated heating effect. Therefore, compromises were necessary to achieve both objectives.

The same experiment conducted with the hemispherical inclusion phantom was replicated with the phantom containing three cylindrical inclusions [Fig. 29 (d), (e), and (f)]. Similar behavior is expected, as evident from the B-mode image [Fig. 29(d)]. However, several

white points within the inclusions, possibly due to the presence of tiny air bubbles or reverberation artifacts, were noted. Fortunately, these high-intensity echo signals did not affect the quality of the displacement map, as demonstrated in Fig. 29(e).

The displacement map showed relatively consistent results along the *x-axis* for the inclusions situated at 0 mm and -15 mm. However, the inclusion located at 15 mm exhibited a diminished response in comparison. Upon closer examination of the MMUS image, a centering error of 2 mm was identified for the middle inclusion. This suggests that there may be a misalignment along the *x-axis* between the focal point of the coil and the actual position of the inclusion at 15 mm, resulting in a reduced effect of the magnetic field.

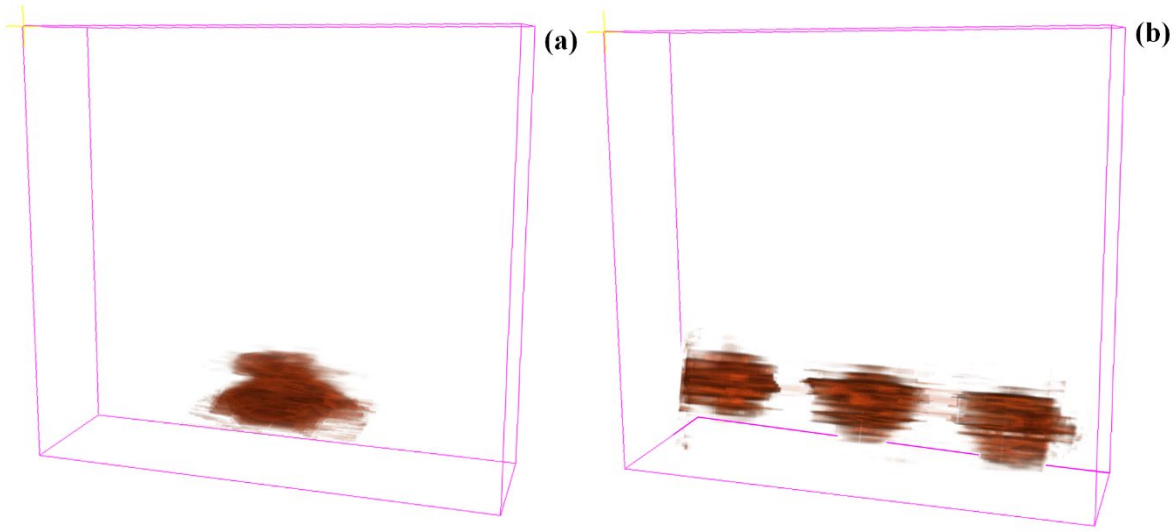

Fig. 30. 3D pulsed MMUS imaging obtained with both tissue-mimicking phantoms. (a) Volumetric representation of the displacements induced to the phantom with a hemispherical inclusion. (b) Volumetric representation of the induced displacements to the phantom containing three cylindrical inclusions.

C. Preliminary theranostic experiments

Magnetic hyperthermia (MH) presents significant challenges, particularly in accurately detecting the precise location of magnetic nanoparticles (MNPs) and non-invasively measuring

temperature variations. By leveraging the magnetomotive ultrasound imaging (MMUS) approach, which estimates displacement resulting from magnetic excitation, the heat generated by the MNPs for diagnostic purposes is exploited. Fig. 31 shows typical MMUS displacement maps obtained from the phantom containing a hemispherical inclusion.

As shown in Fig. 31(a) and 31(b), significant differences in magnetomotive-induced displacements are observed before and after the MH procedure. These MMUS images were acquired at temperatures of approximately 24°C and 30°C, respectively, at the center of the inclusion. The disparity in displacements primarily arises from the impact of temperature on the elastic properties of the phantom material [67, 132].

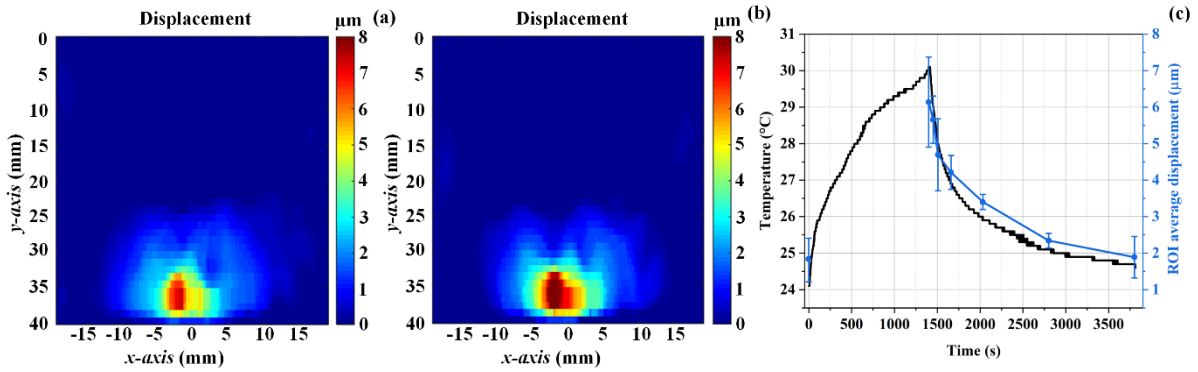

Fig. 31. Displacement under different thermal conditions. (a) Initial displacement mapping of hemispherical inclusion at 24°C: This initial state of the hemispherical inclusion was observed without any MH treatment. (b) Final displacement mapping post-MH therapy at 30°C. It provides a detailed view of how MH treatment has affected the induced displacement. (c) Temporal behavior of the average displacement within the inclusion derived from heating by MH stimulation.

The heating of tissues during thermal therapies generally results in a softening effect, increasing their susceptibility to deformation under consistent stress levels [132]. This change in tissue stiffness is reflected in the displacement graph shown in Fig. 31(c), where the average displacement of each pixel within the region of interest (ROI) is considered. However, it is essential to acknowledge that this treatment approach may introduce a certain level of uncertainty, as indicated by the error bars in the graph. Additionally, the non-uniform distribution of induced displacement within the ROI used to estimate the mean displacement in the inclusion further contributes to this uncertainty.

Therefore, comprehensive characterization of tissue properties is essential to ensure accurate and meaningful analysis in MH treatment. This evaluation should consider various additional factors that may influence tissue response to MH treatment, such as tissue

heterogeneity, hydration levels, and vascular perfusion. The MMUS displacement map, which captures the induced displacement, provides a visual and quantifiable representation of how MNPs have affected the mechanical properties of the tissue. The magnitude of displacement correlates with the strength of the thermal effect, with greater displacement indicating a more pronounced thermal effect. Thus, MMUS imaging offers valuable insights into the therapeutic efficacy of MH treatment and its impact on tissue mechanics.

Conclusions

In conclusion, the research conducted in this study demonstrated the potential of integrating a magnetic hyperthermia (MH) device with a magnetomotive ultrasound (MMUS) imaging system to create an automatized theranostic platform. The imaging capabilities of this platform, which combine the localized heating effects of MNPs with high-resolution MMUS imaging, presented novel diagnostic possibilities to be conducted during MH. The results confirmed the system's capacity to non-invasively localize MNPs, monitor thermal changes, and visualize alterations in tissue properties. However, challenges remain, particularly in addressing inherent signal-noise issues to improve the generation of 3D imaging. Additionally, it is crucial to understand better the heating effects on tissue stiffness and subsequent mechanical response. Therefore, comprehensive tissue characterization and an understanding of the precise correlation between tissue deformation, heat generation, and therapeutic outcomes are ongoing research areas in our group GIIMUS.

Bibliography

[1] C. O'Connor, J. U. Adams, and J. Fairman, *Essentials of Cell Biology*. Nature: Nature Education (in English), 2014.

[2] A. W. Lambert, D. R. Pattabiraman, and R. A. Weinberg, "Emerging Biological Principles of Metastasis," (in eng), *Cell,* vol. 168, no. 4, pp. 670-691, Feb 9 2017, doi: 10.1016/j.cell.2016.11.037.

[3] G. M. Cooper., *The Cell: A Molecular Approach. 2nd edition.* NCBI: Sinauer Associates Inc (in English), 2000.

[4] P. Anand *et al.*, "Cancer is a preventable disease that requires major lifestyle changes," (in eng), *Pharm Res,* vol. 25, no. 9, pp. 2097-116, Sep 2008, doi: 10.1007/s11095-008-9661-9.

[5] B. Pedersen, D. P. Koktved, and L. L. Nielsen, "Living with side effects from cancer treatment--a challenge to target information," (in eng), *Scand J Caring Sci,* vol. 27, no. 3, pp. 715-23, Sep 2013, doi: 10.1111/j.1471-6712.2012.01085.x.

[6] K. Ahmed and S. F. Zaidi, "Treating cancer with heat: hyperthermia as promising strategy to enhance apoptosis," (in eng), *J Pak Med Assoc,* vol. 63, no. 4, pp. 504-8, Apr 2013.

[7] M. Johannsen *et al.*, "Clinical hyperthermia of prostate cancer using magnetic nanoparticles: presentation of a new interstitial technique," (in eng), *Int J Hyperthermia,* vol. 21, no. 7, pp. 637-47, Nov 2005, doi: 10.1080/02656730500158360.

[8] A. Jordan *et al.*, "Presentation of a new magnetic field therapy system for the treatment of human solid tumors with magnetic fluid hyperthermia," *Journal of Magnetism and Magnetic Materials,* vol. 225, no. 1, pp. 118-126, 2001/01/01/ 2001, doi: https://doi.org/10.1016/S0304-8853(00)01239-7.

[9] A. Jordan, R. Scholz, P. Wust, H. Fähling, and F. Roland, "Magnetic fluid hyperthermia (MFH): Cancer treatment with AC magnetic field induced excitation of biocompatible superparamagnetic nanoparticles," *Journal of Magnetism and Magnetic Materials,* vol. 201, no. 1, pp. 413-419, 1999/07/01/ 1999, doi: https://doi.org/10.1016/S0304-8853(99)00088-8.

[10] R. K. Gilchrist, R. Medal, W. D. Shorey, R. C. Hanselman, J. C. Parrott, and C. B. Taylor, "Selective inductive heating of lymph nodes," (in eng), *Ann Surg,* vol. 146, no. 4, pp. 596-606, Oct 1957, doi: 10.1097/00000658-195710000-00007.

[11] S. V. Spirou, M. Basini, A. Lascialfari, C. Sangregorio, and C. Innocenti, "Magnetic Hyperthermia and Radiation Therapy: Radiobiological Principles and Current Practice (†)," (in eng), *Nanomaterials (Basel),* vol. 8, no. 6, Jun 3 2018, doi: 10.3390/nano8060401.

[12] P. Wust *et al.*, "Hyperthermia in combined treatment of cancer," (in eng), *Lancet Oncol,*

vol. 3, no. 8, pp. 487-97, Aug 2002, doi: 10.1016/s1470-2045(02)00818-5.

[13] R. L. Page, D. E. Thrall, M. W. Dewhirst, and R. E. Meyer, "Whole-body hyperthermia. Rationale and potential use for cancer treatment," (in eng), *J Vet Intern Med,* vol. 1, no. 3, pp. 110-20, Jul-Sep 1987, doi: 10.1111/j.1939-1676.1987.tb01998.x.

[14] J. van der Zee, "Heating the patient: a promising approach?," (in eng), *Ann Oncol,* vol. 13, no. 8, pp. 1173-84, Aug 2002, doi: 10.1093/annonc/mdf280.

[15] J. Overgaard, "The heat is (still) on--the past and future of hyperthermic radiation oncology," (in eng), *Radiother Oncol,* vol. 109, no. 2, pp. 185-7, Nov 2013, doi: 10.1016/j.radonc.2013.11.004.

[16] S. V. Strother, J. M. Bull, and S. A. Branham, "Activation of coagulation during therapeutic whole body hyperthermia," (in eng), *Thromb Res,* vol. 43, no. 3, pp. 353-60, Aug 1 1986, doi: 10.1016/0049-3848(86)90155-6.

[17] M. Peiravi, H. Eslami, M. Ansari, and H. Zare-Zardini, "Magnetic hyperthermia: Potentials and limitations," *Journal of the Indian Chemical Society,* vol. 99, no. 1, p. 100269, 2022/01/01/ 2022, doi: https://doi.org/10.1016/j.jics.2021.100269.

[18] D. Hensley *et al.*, "Combining magnetic particle imaging and magnetic fluid hyperthermia in a theranostic platform," *Phys Med Biol,* vol. 62, no. 9, pp. 3483-3500, May 7 2017, doi: 10.1088/1361-6560/aa5601.

[19] D. Ho, X. Sun, and S. Sun, "Monodisperse Magnetic Nanoparticles for Theranostic Applications," *Accounts of Chemical Research,* vol. 44, no. 10, pp. 875-882, 2011/10/18 2011, doi: 10.1021/ar200090c.

[20] S. S. Kelkar and T. M. Reineke, "Theranostics: combining imaging and therapy," (in eng), *Bioconjug Chem,* vol. 22, no. 10, pp. 1879-903, Oct 19 2011, doi: 10.1021/bc200151q.

[21] Y. Hadadian, J. H. Uliana, A. A. O. Carneiro, and T. Z. Pavan, "A Novel Theranostic Platform: Integration of Magnetomotive and Thermal Ultrasound Imaging With Magnetic Hyperthermia," (in eng), *IEEE Trans Biomed Eng,* vol. 68, no. 1, pp. 68-77, Jan 2021, doi: 10.1109/tbme.2020.2990873.

[22] J. Eber and C. Villaseñor, "Ultrasound: advantages, disadvantages, and controversies," (in eng), *Nurse Pract Forum,* vol. 2, no. 4, pp. 239-242, 1991/12// 1991. [Online]. Available: http://europepmc.org/abstract/MED/1840986.

[23] E. C. Abenojar, S. Wickramasinghe, J. Bas-Concepcion, and A. C. S. Samia, "Structural effects on the magnetic hyperthermia properties of iron oxide nanoparticles," *Progress in Natural Science: Materials International,* vol. 26, no. 5, pp. 440-448, 2016/10/01/ 2016, doi: https://doi.org/10.1016/j.pnsc.2016.09.004.

[24] D. Chang *et al.*, "Biologically Targeted Magnetic Hyperthermia: Potential and Limitations," (in eng), *Front Pharmacol,* vol. 9, p. 831, 2018, doi: 10.3389/fphar.2018.00831.

[25] M. Mehrmohammadi, J. Oh, S. Mallidi, and S. Y. Emelianov, "Pulsed magneto-motive ultrasound imaging using ultrasmall magnetic nanoprobes," (in eng), *Molecular imaging,*

vol. 10, no. 2, pp. 102-110, 2011. [Online]. Available: https://pubmed.ncbi.nlm.nih.gov/21439255
https://www.ncbi.nlm.nih.gov/pmc/articles/PMC3101631/.

[26] M. Mehrmohammadi *et al.*, "In vivo pulsed magneto-motive ultrasound imaging using high-performance magnetoactive contrast nanoagents," (in eng), *Nanoscale,* vol. 5, no. 22, pp. 11179-11186, 2013, doi: 10.1039/c3nr03669c.

[27] J. Oh, M. D. Feldman, J. Kim, C. Condit, S. Emelianov, and T. E. Milner, "Detection of magnetic nanoparticles in tissue using magneto-motive ultrasound," *Nanotechnology,* vol. 17, no. 16, pp. 4183-90, Aug 28 2006, doi: 10.1088/0957-4484/17/16/031.

[28] T. W. J. Almeida, D. R. T. Sampaio, T. Z. Pavan, and A. A. O. Carneiro, "Shear wave Vibro Magneto Acoustography for measuring tissue mimicking phantom elasticity and viscosity," in *2014 IEEE International Ultrasonics Symposium*, 3-6 Sept. 2014 2014, pp. 1097-1100, doi: 10.1109/ULTSYM.2014.0269.

[29] S. Sjöstrand, M. Evertsson, and T. Jansson, "Magnetomotive Ultrasound Imaging Systems: Basic Principles and First Applications," *Ultrasound in Medicine & Biology,* vol. 46, no. 10, pp. 2636-2650, 2020/10/01/ 2020, doi: https://doi.org/10.1016/j.ultrasmedbio.2020.06.014.

[30] T. W. J. Almeida, D. R. T. Sampaio, A. C. Bruno, T. Z. Pavan, and A. A. O. Carneiro, "Comparison between shear wave dispersion magneto motive ultrasound and transient elastography for measuring tissue-mimicking phantom viscoelasticity," *IEEE Transactions on Ultrasonics, Ferroelectrics, and Frequency Control,* vol. 62, no. 12, pp. 2138-2145, 2015, doi: 10.1109/TUFFC.2015.007353.

[31] T. Ersepke, T. C. Kranemann, and G. Schmitz, "On the Performance of Time Domain Displacement Estimators for Magnetomotive Ultrasound Imaging," *IEEE Transactions on Ultrasonics, Ferroelectrics, and Frequency Control,* vol. 66, no. 5, pp. 911-921, 2019, doi: 10.1109/TUFFC.2019.2903885.

[32] Y. Hadadian, M. Azimbagirad, E. A. Navas, and T. Z. Pavan, "A versatile induction heating system for magnetic hyperthermia studies under different experimental conditions," (in eng), *Rev Sci Instrum,* vol. 90, no. 7, p. 074701, Jul 2019, doi: 10.1063/1.5080348.

[33] I. Hilger, W. Andrä, R. Hergt, R. Hiergeist, H. Schubert, and W. A. Kaiser, "Electromagnetic Heating of Breast Tumors in Interventional Radiology: In Vitro and in Vivo Studies in Human Cadavers and Mice," *RSNA,* vol. 218, no. 2, pp. 570-575, 2001, doi: 10.1148/radiology.218.2.r01fe19570.

[34] R. Ivkov *et al.*, "Application of high amplitude alternating magnetic fields for heat induction of nanoparticles localized in cancer," (in eng), *Clin Cancer Res,* vol. 11, no. 19 Pt 2, pp. 7093s-7103s, Oct 1 2005, doi: 10.1158/1078-0432.Ccr-1004-0016.

[35] E. E. Mazon *et al.*, "A high-resolution frequency variable experimental setup for studying ferrofluids used in magnetic hyperthermia," (in eng), *Rev Sci Instrum,* vol. 88, no. 8, p. 084705, Aug 2017, doi: 10.1063/1.4998975.

[36] M. Evertsson, M. Cinthio, S. Fredriksson, F. Olsson, H. W. Persson, and T. Jansson, "Frequency- and phase-sensitive magnetomotive ultrasound imaging of superparamagnetic iron oxide nanoparticles," *IEEE Transactions on Ultrasonics, Ferroelectrics, and Frequency Control,* vol. 60, no. 3, pp. 481-491, 2013, doi: 10.1109/TUFFC.2013.2591.

[37] R. E. Rosensweig, "Heating magnetic fluid with alternating magnetic field," *Journal of Magnetism and Magnetic Materials,* vol. 252, pp. 370-374, 2002/11/01/ 2002, doi: https://doi.org/10.1016/S0304-8853(02)00706-0.

[38] N. Dudchenko, S. Pawar, I. Perelshtein, and D. Fixler, "Magnetite Nanoparticles: Synthesis and Applications in Optics and Nanophotonics," (in eng), *Materials (Basel, Switzerland),* vol. 15, no. 7, Apr 1 2022, doi: 10.3390/ma15072601.

[39] S. Arsalani *et al.*, "Uniform size PEGylated iron oxide nanoparticles as a potential theranostic agent synthesized by a simple optimized coprecipitation route," *Journal of Magnetism and Magnetic Materials,* vol. 564, p. 170091, 2022/12/15/ 2022, doi: https://doi.org/10.1016/j.jmmm.2022.170091.

[40] S. Arsalani *et al.*, "The effect of magnetization of natural rubber latex-coated magnetite nanoparticles on shear wave dispersion magneto-motive ultrasound," *Physics in Medicine & Biology,* vol. 64, no. 21, p. 215019, 2019/11/04 2019, doi: 10.1088/1361-6560/ab4693.

[41] D. R. T. Sampaio, F. W. Grillo, A. C. Bruno, T. Z. Pavan, and A. A. O. Carneiro, "A magneto-motive ultrasound platform designed for pre-clinical and clinical applications %J Research on Biomedical Engineering," *Research on Biomedical Engineering,* vol. 32, pp. 337-346, 2016. [Online]. Available: http://www.scielo.br/scielo.php?script=sci_arttext&pid=S2446-47402016000400337&nrm=iso.

[42] D. Thapa, B. E. Levy, D. L. Marks, and A. L. Oldenburg, "Inversion of displacement fields to quantify the magnetic particle distribution in homogeneous elastic media from magnetomotive ultrasound," *Physics in Medicine & Biology,* vol. 64, no. 12, p. 125019, 2019/06/20 2019, doi: 10.1088/1361-6560/ab1f2b.

[43] M. Evertsson *et al.*, "Multimodal detection of iron oxide nanoparticles in rat lymph nodes using magnetomotive ultrasound imaging and magnetic resonance imaging," *IEEE Transactions on Ultrasonics, Ferroelectrics, and Frequency Control,* vol. 61, no. 8, pp. 1276-1283, 2014, doi: 10.1109/TUFFC.2014.3034.

[44] A. C. Bruno, D. R. T. Sampaio, T. Z. Pavan, O. Baffa, and A. A. O. Carneiro, "A hybrid transducer to evaluate stomach emptying by ultrasound and susceptometric measurements: an in vivo feasibility study," *IEEE Transactions on Ultrasonics, Ferroelectrics, and Frequency Control,* vol. 62, no. 7, pp. 1288-1294, 2015, doi: 10.1109/TUFFC.2014.006950.

[45] M. Qu, M. Mehrmohammadi, and S. Emelianov, "Detection of Nanoparticle Endocytosis Using Magneto-Photoacoustic Imaging," vol. 7, no. 20, pp. 2858-2862, 2011, doi: https://doi.org/10.1002/smll.201100960.

[46] A. G. Pope *et al.*, "Contrast-enhanced imaging of SPIO-labeled platelets using magnetomotive ultrasound," *Physics in Medicine & Biology,* vol. 58, no. 20, p. 7277, 2013/09/26 2013, doi: 10.1088/0031-9155/58/20/7277.

[47] S. Mei, Y. Hu, H. Xu, and H. Wen, "The Class D Audio Power Amplifier: A Review," *Electronics*, vol. 11, no. 19*,* doi: 10.3390/electronics11193244.

[48] R. Palmer, "Guidelines for Measuring Audio Power Amplifier Performance," *Texas Instruments Application Report,* no. SLOA068A, pp. 1-25, 2001.

[49] M. Kazimierczuk, "Winding Resistance at High Frequencies," in *High‐Frequency Magnetic Components*: Wiley, 2013, ch. 5, pp. 265-382.

[50] J. Li *et al.*, "Magneto-Optical Nanoparticles for Cyclic Magnetomotive Photoacoustic Imaging," *ACS Nano,* vol. 9, no. 2, pp. 1964-1976, 2015/02/24 2015, doi: 10.1021/nn5069258.

[51] B. Arnal, C. W. Wei, J. Li, X. Gao, and M. O'Donnell, "Highly sensitive magneto-motive photoacoustic and ultrasound (PAUS) imaging with cyclic excitations," *Journal of Optics,* vol. 18, no. 2, p. 024009, 2016/01/19 2016, doi: 10.1088/2040-8978/18/2/024009.

[52] E. E. Mazon, S. Arsalani, J. H. Uliana, A. A. O. Carneiro, A. J. Gualdi, and T. Z. Pavan, "A pulsed magnetomotive ultrasound imaging system for magnetic nanoparticle detection," in *2021 IEEE UFFC Latin America Ultrasonics Symposium (LAUS)*, 4-5 Oct. 2021 2021, pp. 1-4, doi: 10.1109/LAUS53676.2021.9639204.

[53] M. H. Rashid, *Power Electronics: Devices, Circuits, and Applications*. Pearson, 2014, p. 702.

[54] M. K. Kazimierczuk and D. Czarkowski, *Resonat Power Converters* (1). New Jersey: John Wiley & Sons, 2011, p. 632.

[55] N. A. Usov and O. N. Serebryakova, "Equilibrium properties of assembly of interacting superparamagnetic nanoparticles," (in eng), *Scientific reports,* vol. 10, no. 1, p. 13677, Aug 13 2020, doi: 10.1038/s41598-020-70711-w.

[56] K. Enpuku, T. Sasayama, and T. Yoshida, "Estimation of magnetic moment and anisotropy energy of magnetic markers for biosensing application," *Journal of Applied Physics,* vol. 119, no. 18, p. 184902, 2016, doi: 10.1063/1.4948951.

[57] J. F. Schenck, "Safety of strong, static magnetic fields," (in eng), *Journal of magnetic resonance imaging : JMRI,* vol. 12, no. 1, pp. 2-19, Jul 2000, doi: 10.1002/1522-2586(200007)12:1<2::aid-jmri2>3.0.co;2-v.

[58] T. Ersepke, T. C. Kranemann, and G. Schmitz, "Frequency response of soft tissue displacements induced by the force on magnetic nanoparticles," in *2017 IEEE International Ultrasonics Symposium (IUS)*, 6-9 Sept. 2017 2017, pp. 1-1, doi: 10.1109/ULTSYM.2017.8092878.

[59] A. M. Abou-Alfotouh, A. V. Radun, H. Chang, and C. Winterhalter, "A 1-MHz hard-switched silicon carbide DC–DC converter," *IEEE Transactions on Power Electronics,* vol. 21, no. 4, pp. 880-889, 2006, doi: 10.1109/TPEL.2006.876891.

[60] P. C. Todd, "Snubber circuits: Theory, design and application," in *Unitrode-Power Supply Design Seminar*, 1993, pp. 2-1.

[61] A. Cebrecos, N. Jiménez, R. Tarazona, M. Company, J. M. Benlloch, and F. Camarena, "Characterization of Viscoelastic Media Combining Ultrasound and Magnetic-Force Induced Vibrations on an Embedded Soft Magnetic Sphere," *IEEE Transactions on Ultrasonics, Ferroelectrics, and Frequency Control,* vol. 68, no. 12, pp. 3540-3548, 2021, doi: 10.1109/TUFFC.2021.3097883.

[62] P. K. Lee, K. C. Kuo, C. J. Wu, Z. T. Wong, and J. Y. Yen, "Prediction of iron losses using the modified Steinmetz equation under the sinusoidal waveform," in *2011 8th Asian Control Conference (ASCC)*, 15-18 May 2011 2011, pp. 579-584.

[63] P. Popović and B. D. Zoya, *Introductory Electromagnetics*. New Jersey: Prentice-Hall, 2000, p. 581.

[64] G. Bertotti, *Hysteresis in Magnetism: For Physicists, Materials Scientists, and Engineer* (Hysteresis in Magnetism). San Diego: Academic Press, 1998, p. 588.

[65] T. J. Hall, M. Bilgen, M. F. Insana, and T. A. Krouskop, "Phantom materials for elastography," *IEEE Transactions on Ultrasonics, Ferroelectrics, and Frequency Control,* vol. 44, no. 6, pp. 1355-1365, 1997, doi: 10.1109/58.656639.

[66] T. Z. Pavan, E. L. Madsen, G. R. Frank, A. Adilton O Carneiro, and T. J. Hall, "Nonlinear elastic behavior of phantom materials for elastography," *Physics in Medicine and Biology,* vol. 55, no. 9, pp. 2679-2692, 2010/04/19 2010, doi: 10.1088/0031-9155/55/9/017.

[67] Y. Hadadian, A. P. Ramos, and T. Z. Pavan, "Role of zinc substitution in magnetic hyperthermia properties of magnetite nanoparticles: interplay between intrinsic properties and dipolar interactions," *Scientific Reports,* vol. 9, no. 1, p. 18048, 2019/12/02 2019, doi: 10.1038/s41598-019-54250-7.

[68] Y. Hadadian *et al.*, "Synthesis and characterization of zinc substituted magnetite nanoparticles and their application to magneto-motive ultrasound imaging," *Journal of Magnetism and Magnetic Materials,* vol. 465, pp. 33-43, 2018/11/01/ 2018, doi: https://doi.org/10.1016/j.jmmm.2018.05.069.

[69] C. Vasilica, A. Adeel, and A. B. M. D. Stephen, "Magnetomotive optical coherence elastography for microrheology of biological tissues," *Journal of Biomedical Optics,* vol. 18, no. 12, p. 121504, 10/1 2013, doi: 10.1117/1.JBO.18.12.121504.

[70] M. Evertsson *et al.*, "Towards real-time magnetomotive ultrasound imaging," in *2017 IEEE International Ultrasonics Symposium (IUS)*, 6-9 Sept. 2017 2017, pp. 1-4, doi: 10.1109/ULTSYM.2017.8092548.

[71] R. T. Gordon and D. Gordon, "Selective resolution of plaques and treatment of Atherosclerosis by biophysical alteration of “cellular” and “intracellular” properties," *Medical Hypotheses,* vol. 7, no. 2, pp. 217-229, 1981/02/01/ 1981, doi: https://doi.org/10.1016/0306-9877(81)90118-3.

[72] U. Engelmann, E. M. Buhl, M. Baumann, T. Schmitz-Rode, and I. Slabu, "Agglomeration

of magnetic nanoparticles and its effects on magnetic hyperthermia," vol. 3, no. 2, pp. 457-460, 2017, doi: doi:10.1515/cdbme-2017-0096.

[73] S. E. Favela-Camacho, E. J. Samaniego-Benítez, A. Godínez-García, L. M. Avilés-Arellano, and J. F. Pérez-Robles, "How to decrease the agglomeration of magnetite nanoparticles and increase their stability using surface properties," *Colloids and Surfaces A: Physicochemical and Engineering Aspects,* vol. 574, pp. 29-35, 2019/08/05/ 2019, doi: https://doi.org/10.1016/j.colsurfa.2019.04.016.

[74] E. M. Materón *et al.*, "Magnetic nanoparticles in biomedical applications: A review," *Applied Surface Science Advances,* vol. 6, p. 100163, 2021/12/01/ 2021, doi: https://doi.org/10.1016/j.apsadv.2021.100163.

[75] M. I. Anik, M. K. Hossain, I. Hossain, A. M. U. B. Mahfuz, M. T. Rahman, and I. Ahmed, "Recent progress of magnetic nanoparticles in biomedical applications: A review," *Nano Select,* https://doi.org/10.1002/nano.202000162 vol. 2, no. 6, pp. 1146-1186, 2021/06/01 2021, doi: https://doi.org/10.1002/nano.202000162.

[76] M. Ebadi, K. Buskaran, S. Bullo, M. Z. Hussein, S. Fakurazi, and G. Pastorin, "Synthesis and Cytotoxicity Study of Magnetite Nanoparticles Coated with Polyethylene Glycol and Sorafenib-Zinc/Aluminium Layered Double Hydroxide," (in eng), *Polymers (Basel),* vol. 12, no. 11, Nov 17 2020, doi: 10.3390/polym12112716.

[77] G. Sharma *et al.*, "Iron oxide nanoparticle agglomeration influences dose rates and modulates oxidative stress-mediated dose-response profiles in vitro," (in eng), *Nanotoxicology,* vol. 8, no. 6, pp. 663-75, Sep 2014, doi: 10.3109/17435390.2013.822115.

[78] J. Carrey, B. Mehdaoui, and M. Respaud, "Simple models for dynamic hysteresis loop calculations of magnetic single-domain nanoparticles: Application to magnetic hyperthermia optimization," *Journal of Applied Physics,* vol. 109, no. 8, 2011, doi: 10.1063/1.3551582.

[79] P. Langevin, "Sur la théorie du magnétisme," *J. Phys. Theor. Appl.,* 10.1051/jphystap:019050040067800 vol. 4, no. 1, pp. 678-693, // 1905. [Online]. Available: https://doi.org/10.1051/jphystap:019050040067800.

[80] Y. L. Raikher and V. I. Stepanov, "Dynamic hysteresis of a superparamagnetic nanoparticle at low-to-intermediate frequencies," *Journal of Magnetism and Magnetic Materials,* vol. 300, no. 1, pp. e311-e314, 2006, doi: 10.1016/j.jmmm.2005.10.108.

[81] A. H. Sámano *et al.*, "A dynamic hysteresis meter for studying ferrofluids designed for magnetic hyperthermia," *Measurement Science and Technology,* vol. 31, no. 5, p. 055902, 2020/02/26 2020, doi: 10.1088/1361-6501/ab6521.

[82] S. Nain, N. Kumar, B. Chudasama, and P. Kumar Avti, "The SLP estimation of the nanoparticle systems using size-dependent magnetic properties for the magnetic hyperthermia therapy," *Journal of Magnetism and Magnetic Materials,* vol. 565, p. 170219, 2023/01/01/ 2023, doi: https://doi.org/10.1016/j.jmmm.2022.170219.

[83] G. Capistrano *et al.*, "Noninvasive intratumoral thermal dose determination during in vivo

magnetic nanoparticle hyperthermia: combining surface temperature measurements and computer simulations," (in eng), *Int J Hyperthermia,* vol. 37, no. 3, pp. 120-140, Dec 2020, doi: 10.1080/02656736.2020.1826583.

[84] H. F. Rodrigues, F. M. Mello, L. C. Branquinho, N. Zufelato, E. P. Silveira-Lacerda, and A. F. Bakuzis, "Real-time infrared thermography detection of magnetic nanoparticle hyperthermia in a murine model under a non-uniform field configuration," *International Journal of Hyperthermia,* vol. 29, no. 8, pp. 752-767, 2013/12/01 2013, doi: 10.3109/02656736.2013.839056.

[85] C. Leuschner, C. S. S. R. Kumar, W. Hansel, W. Soboyejo, J. Zhou, and J. Hormes, "LHRH-conjugated Magnetic Iron Oxide Nanoparticles for Detection of Breast Cancer Metastases," *Breast Cancer Research and Treatment,* vol. 99, no. 2, pp. 163-176, 2006/09/01 2006, doi: 10.1007/s10549-006-9199-7.

[86] A. F. Bakuzis, "Nanomedicine and thermal therapies: where are we going?," *International Journal of Hyperthermia,* vol. 37, no. 3, pp. 1-3, 2020/12/15 2020, doi: 10.1080/02656736.2020.1854355.

[87] M. E. Cano, A. Barrera, J. C. Estrada, A. Hernandez, and T. Cordova, "An induction heater device for studies of magnetic hyperthermia and specific absorption ratio measurements," (in eng), *Rev Sci Instrum,* vol. 82, no. 11, p. 114904, Nov 2011, doi: 10.1063/1.3658818.

[88] M.-H. Ahn, S.-K. Baek, J. Min, and J.-H. Park, "A portable electromagnetic induction heating device for point-of-care diagnostics," *BioChip Journal,* vol. 10, no. 3, pp. 208-214, 2016/09/01 2016, doi: 10.1007/s13206-016-0307-4.

[89] E. E. Mazon, A. H. Sámano, H. Calleja, L. H. Quintero, J. A. Paz, and M. E. Cano, "A frequency tuner for resonant inverters suitable for magnetic hyperthermia applications," *Measurement Science and Technology,* vol. 28, no. 9, 2017, doi: 10.1088/1361-6501/aa7be2.

[90] M. Soleymani *et al.*, "Effects of multiple injections on the efficacy and cytotoxicity of folate-targeted magnetite nanoparticles as theranostic agents for MRI detection and magnetic hyperthermia therapy of tumor cells," *Scientific Reports,* vol. 10, no. 1, p. 1695, 2020/02/03 2020, doi: 10.1038/s41598-020-58605-3.

[91] B. Herrero de la Parte *et al.*, "Proposal of New Safety Limits for In Vivo Experiments of Magnetic Hyperthermia Antitumor Therapy," *Cancers*, vol. 14, no. 13, doi: 10.3390/cancers14133084.

[92] P. Herasymenko, "Soft Start-up Output Current of PDM-based Series-Resonant Converter for Induction Heating Application," in *2019 IEEE 2nd Ukraine Conference on Electrical and Computer Engineering (UKRCON)*, 2-6 July 2019 2019, pp. 570-575, doi: 10.1109/UKRCON.2019.8879832.

[93] J. Li, "Design and simulation of soft start control circuit for induction heating circuit," *AIP Conference Proceedings,* vol. 2066, no. 1, p. 020052, 2019, doi: 10.1063/1.5089094.

[94] P. Herasymenko and V. Pavlovskyi, "Soft start-up strategy of pulse-density-modulated

series-resonant converter for induction heating application," *International Journal of Power Electronics and Drive Systems,* vol. 12, pp. 258-272, 2021.

[95] K. C. Wu, *Switch-Mode Power Converters: Design and Analysis*. Elsevier Academic Press, 2006, p. 408.

[96] B. W. Williams, *Power Electronics: Devices, Drivers, Applications, and Passive Components* (McGraw-Hill, no. 2nd). New York: McGraw-Hill, 1992.

[97] J. M. Espi-Huerta, E. J. Dede Garcia Santamaria, R. Garcia Gil, and J. Castello-Moreno, "Design of the L-LC Resonant Inverter for Induction Heating Based on Its Equivalent SRI," *IEEE Transactions on Industrial Electronics,* vol. 54, no. 6, pp. 3178-3187, 2007, doi: 10.1109/tie.2007.905928.

[98] Y. Zhongming, P. K. Jain, and P. C. Sen, "A Full-Bridge Resonant Inverter With Modified Phase-Shift Modulation for High-Frequency AC Power Distribution Systems," *IEEE Transactions on Industrial Electronics,* vol. 54, no. 5, pp. 2831-2845, 2007, doi: 10.1109/tie.2007.896030.

[99] G. T. Landi, "Simple models for the heating curve in magnetic hyperthermia experiments," *Journal of Magnetism and Magnetic Materials,* vol. 326, pp. 14-21, 2013/01/01/ 2013, doi: https://doi.org/10.1016/j.jmmm.2012.08.034.

[100] H. L. Ring, A. Sharma, R. Ivkov, and J. C. Bischof, "The impact of data selection and fitting on SAR estimation for magnetic nanoparticle heating," (in eng), *Int J Hyperthermia,* vol. 37, no. 3, pp. 100-107, Dec 2020, doi: 10.1080/02656736.2020.1810332.

[101] S. Siami, C. Joubert, and C. Glaize, "High frequency model for power electronics capacitors," *IEEE Transactions on Power Electronics,* vol. 16, no. 2, pp. 157-166, 2001, doi: 10.1109/63.911139.

[102] M. Chari and Z. Csendes, "Finite element analysis of the skin effect in current carrying conductors," *IEEE Transactions on Magnetics,* vol. 13, no. 5, pp. 1125-1127, 1977, doi: 10.1109/TMAG.1977.1059545.

[103] G. W. Ludwig and S. A. El-Hamamsy, "Coupled inductance and reluctance models of magnetic components," *IEEE Transactions on Power Electronics,* vol. 6, no. 2, pp. 240-250, 1991, doi: 10.1109/63.76810.

[104] J. Penttonen, M. Shafiq, and M. Lehtonen, "Reluctance Network Analysis for Complex Coupled Inductors," *Journal of Power and Energy Engineering,* vol. 05, pp. 1-14, 01/01 2017, doi: 10.4236/jpee.2017.51001.

[105] M. V. C. C. James M. Fiore, *DC Electrical Circuit Analysis: A Practical Approach*. 2020.

[106] R. E. Best, *Phase-Locked Loops Design, Simulation, and Applications, Sixth Ed*. McGraw-Hill, 2004.

[107] S. Goldman, *Phase-Locked Loops Engineering Handbook for Integrated Circuits*. Norwood. MA: Artech House, 2007.

[108] A. J. Giustini, A. A. Petryk, S. M. Cassim, J. A. Tate, I. Baker, and P. J. Hoopes, "MAGNETIC NANOPARTICLE HYPERTHERMIA IN CANCER TREATMENT," (in

eng), *Nano Life,* vol. 1, no. 1n02, Mar 2010, doi: 10.1142/s1793984410000067.

[109] T. J. Gutiérrez and V. A. Alvarez, "Chapter 31 - Nanoparticles for Hyperthermia Applications," in *Handbook of Nanomaterials for Industrial Applications*, C. Mustansar Hussain Ed.: Elsevier, 2018, pp. 563-576.

[110] S. S. Kelkar and T. M. Reineke, "Theranostics: Combining Imaging and Therapy," *Bioconjugate Chemistry,* vol. 22, no. 10, pp. 1879-1903, 2011/10/19 2011, doi: 10.1021/bc200151q.

[111] J. R. McCarthy, "The future of theranostic nanoagents," vol. 4, no. 7, pp. 693-695, 2009, doi: 10.2217/nnm.09.58.

[112] B. Siddhardha and P. Parasuraman, "Chapter 3 - Theranostics application of nanomedicine in cancer detection and treatment," in *Nanomaterials for Drug Delivery and Therapy*, A. M. Grumezescu Ed.: William Andrew Publishing, 2019, pp. 59-89.

[113] A. Sharma, E. Cressman, A. Attaluri, D. L. Kraitchman, and R. Ivkov, "Current Challenges in Image-Guided Magnetic Hyperthermia Therapy for Liver Cancer," (in eng), *Nanomaterials (Basel),* vol. 12, no. 16, Aug 12 2022, doi: 10.3390/nano12162768.

[114] J. Wells *et al.*, "Challenges and recommendations for magnetic hyperthermia characterization measurements," *International Journal of Hyperthermia,* vol. 38, no. 1, pp. 447-460, 2021/01/01 2021, doi: 10.1080/02656736.2021.1892837.

[115] H. F. Rodrigues, G. Capistrano, and A. F. Bakuzis, "In vivo magnetic nanoparticle hyperthermia: a review on preclinical studies, low-field nano-heaters, noninvasive thermometry and computer simulations for treatment planning," *International Journal of Hyperthermia,* vol. 37, no. 3, pp. 76-99, 2020/12/15 2020, doi: 10.1080/02656736.2020.1800831.

[116] M. Ma, Y. Zhang, and N. Gu, "Estimation the tumor temperature in magnetic nanoparticle hyperthermia by infrared thermography: Phantom and numerical studies," *Journal of Thermal Biology,* vol. 76, pp. 89-94, 2018/08/01/ 2018, doi: https://doi.org/10.1016/j.jtherbio.2018.07.004.

[117] H.-L. Liu, M.-L. Li, P.-H. Tsui, M.-S. Lin, S.-M. Huang, and J. Bai, "A unified approach to combine temperature estimation and elastography for thermal lesion determination in focused ultrasound thermal therapy," *Physics in Medicine & Biology,* vol. 56, no. 1, p. 169, 2010/12/08 2011, doi: 10.1088/0031-9155/56/1/011.

[118] J. H. Uliana, D. R. T. Sampaio, A. A. O. Carneiro, and T. Z. Pavan, "Photoacoustic-based thermal image formation and optimization using an evolutionary genetic algorithm," *Research on Biomedical Engineering,* vol. 34, 2018.

[119] Y. Liu, P. Bhattarai, Z. Dai, and X. Chen, "Photothermal therapy and photoacoustic imaging via nanotheranostics in fighting cancer," (in eng), *Chem Soc Rev,* vol. 48, no. 7, pp. 2053-2108, Apr 1 2019, doi: 10.1039/c8cs00618k.

[120] C. H. Seo, Y. Shi, S. W. Huang, K. Kim, and M. O'Donnell, "Thermal strain imaging: a review," (in eng), *Interface Focus,* vol. 1, no. 4, pp. 649-64, Aug 6 2011, doi:

10.1098/rsfs.2011.0010.

[121] U. Techavipoo, T. Varghese, Q. Chen, T. A. Stiles, J. A. Zagzebski, and G. R. Frank, "Temperature dependence of ultrasonic propagation speed and attenuation in excised canine liver tissue measured using transmitted and reflected pulses," (in eng), *J Acoust Soc Am,* vol. 115, no. 6, pp. 2859-65, Jun 2004, doi: 10.1121/1.1738453.

[122] K. Kim, C. G. Jeong, and S. J. Hollister, "Non-invasive monitoring of tissue scaffold degradation using ultrasound elasticity imaging," *Acta Biomaterialia,* vol. 4, no. 4, pp. 783-790, 2008/07/01/ 2008, doi: https://doi.org/10.1016/j.actbio.2008.02.010.

[123] A. Avasthi, C. Caro, E. Pozo-Torres, M. P. Leal, and M. L. García-Martín, "Magnetic Nanoparticles as MRI Contrast Agents," (in eng), *Top Curr Chem (Cham),* vol. 378, no. 3, p. 40, May 7 2020, doi: 10.1007/s41061-020-00302-w.

[124] F. Ludwig *et al.*, "Characterization of magnetic nanoparticle systems with respect to their magnetic particle imaging performance," vol. 58, no. 6, pp. 535-545, 2013, doi: doi:10.1515/bmt-2013-0013.

[125] X. L. Liu and H. M. Fan, "Innovative magnetic nanoparticle platform for magnetic resonance imaging and magnetic fluid hyperthermia applications," *Current Opinion in Chemical Engineering,* vol. 4, pp. 38-46, 2014/05/01/ 2014, doi: https://doi.org/10.1016/j.coche.2013.12.010.

[126] M. Wabler *et al.*, "Magnetic resonance imaging contrast of iron oxide nanoparticles developed for hyperthermia is dominated by iron content," *International Journal of Hyperthermia,* vol. 30, no. 3, pp. 192-200, 2014/05/01 2014, doi: 10.3109/02656736.2014.913321.

[127] J. Stelzner *et al.*, "Implementation and imaging with a versatile 180 mm magnetic-particle-imaging field-generator," *Journal of Magnetism and Magnetic Materials,* vol. 559, p. 169509, 2022/10/01/ 2022, doi: https://doi.org/10.1016/j.jmmm.2022.169509.

[128] A. Tomitaka, S. Ota, K. Nishimoto, H. Arami, Y. Takemura, and M. Nair, "Dynamic magnetic characterization and magnetic particle imaging enhancement of magnetic-gold core-shell nanoparticles," (in eng), *Nanoscale,* vol. 11, no. 13, pp. 6489-6496, Mar 28 2019, doi: 10.1039/c9nr00242a.

[129] Z. W. Tay *et al.*, "Magnetic Particle Imaging-Guided Heating in Vivo Using Gradient Fields for Arbitrary Localization of Magnetic Hyperthermia Therapy," (in eng), *ACS Nano,* vol. 12, no. 4, pp. 3699-3713, Apr 24 2018, doi: 10.1021/acsnano.8b00893.

[130] T. C. Kranemann, T. Ersepke, and G. Schmitz, "Real-Time Magnetomotive Ultrasound Imaging Using a Recursive Estimator," in *2018 IEEE International Ultrasonics Symposium (IUS)*, 22-25 Oct. 2018 2018, pp. 1-4, doi: 10.1109/ULTSYM.2018.8579643.

[131] M. Fink, S. J. Rupitsch, S. Lyer, C. Alexiou, and H. Ermert, "An Enhanced Magnetomotive Ultrasound Algorithm to Quantitatively Estimate the Concentration of Iron-Oxide Nanoparticles in Perfused Tissue for Magnetic Drug Targeting," in *2019 IEEE International Ultrasonics Symposium (IUS)*, 6-9 Oct. 2019 2019, pp. 1407-1409, doi:

10.1109/ULTSYM.2019.8925977.

[132] E. Vlaisavljevich, Z. Xu, A. Arvidson, L. Jin, W. Roberts, and C. Cain, "Effects of Thermal Preconditioning on Tissue Susceptibility to Histotripsy," (in eng), *Ultrasound Med Biol,* vol. 41, no. 11, pp. 2938-54, Nov 2015, doi: 10.1016/j.ultrasmedbio.2015.07.016.

Supplementary material

1. Voltage-current sensor circuit

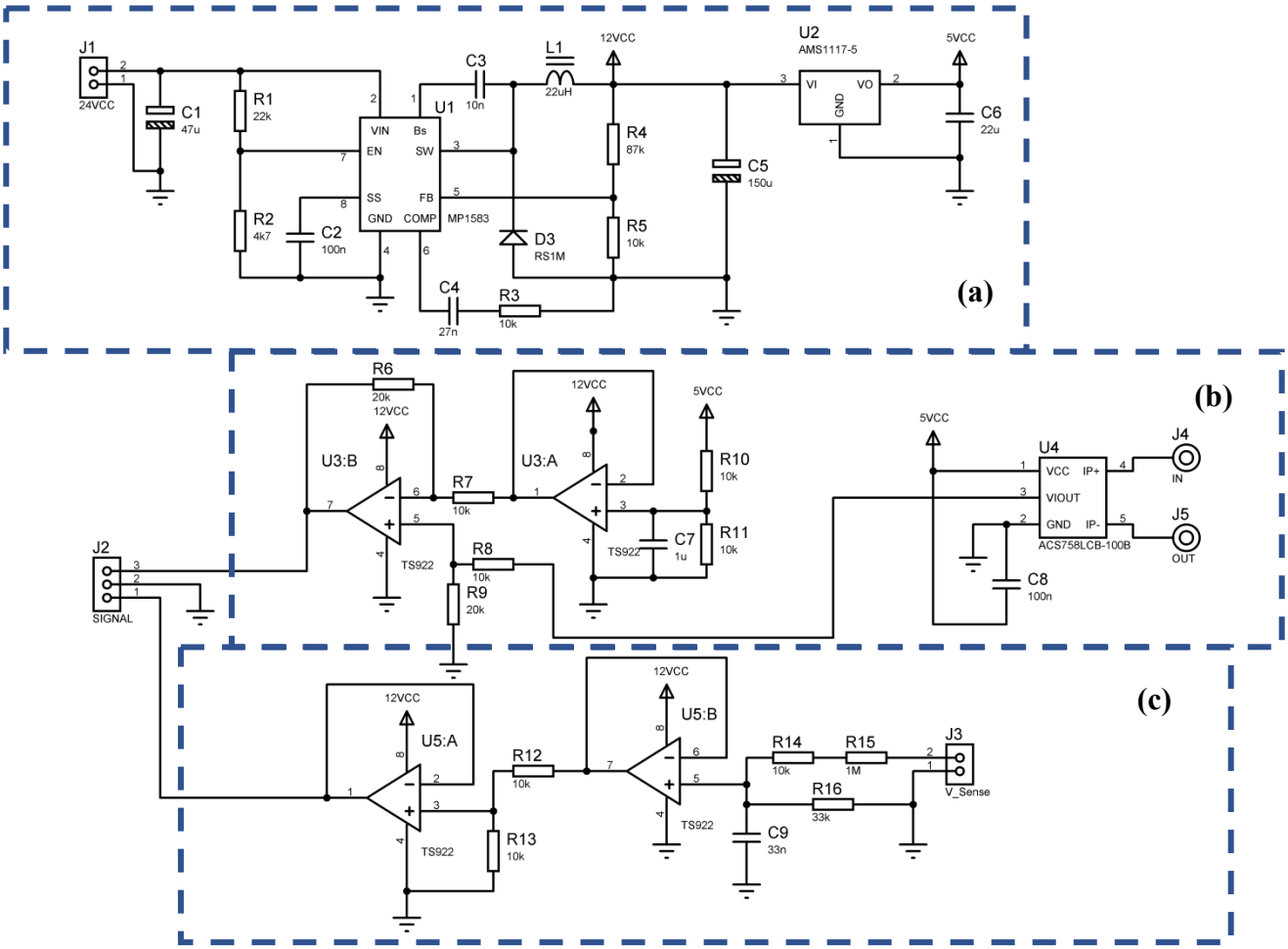

This sensor module utilizes three prince circuits to ensure stable functionality within an operating range from DC to 30 kHz. Box (A) contains a regulated power supply circuit based on a Step-Down converter, providing a voltage range of 15VDC to 25VDC to power the sensor. Box (B) incorporates a current sensor that uses Hall effect technology. This bipolar sensor, tailored for this application, employs operational amplifiers to convert its signal into a unipolar range of 0V to 5V. Finally, the circuit responsible for voltage sensitivity is a simple voltage divider designed to operate within an input range of 0V to 350V and produce an output range of 0V to 5V.

2. High-power MPPT Synchronous Boost/buck Driver Board V4.2

The seller provided the picture.

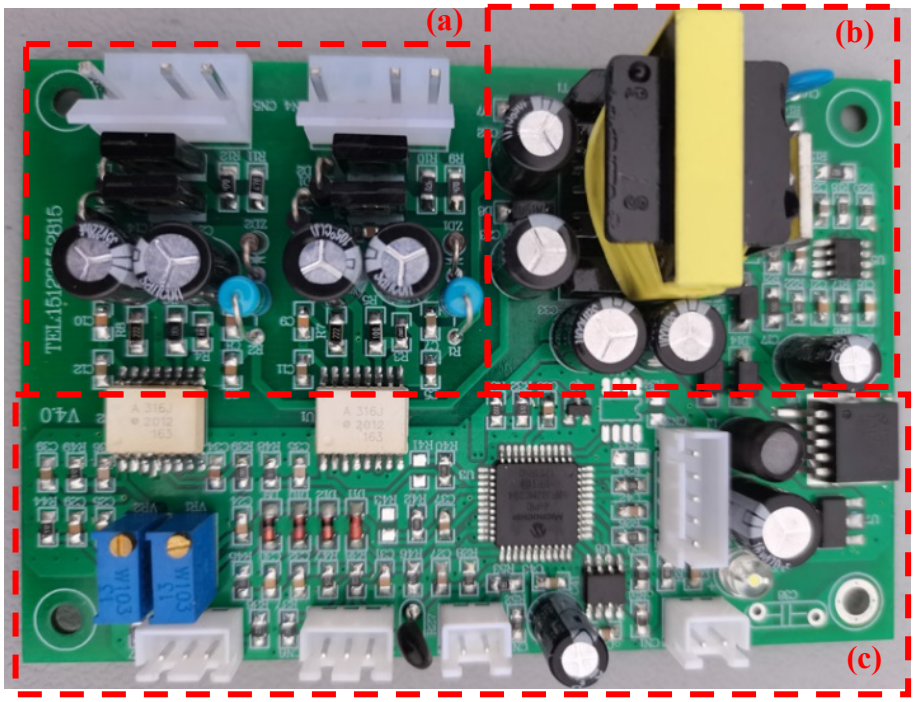

This synchronous control module is designed for high-power Step-Down applications, providing an efficient solution for developing an automatically regulated intelligent current-voltage source. The module comprises three essential components:

(a) An optimized driver for IGBT modules up to 450A, employing a Totem-Pole type topology with optical isolation using a pair of optical couplers. This circuit serves as an adaptation for IGBT activation and enables precise control.

(b) A switched source that supplies power to Section (A). Its operation is based on a Flyback circuit configuration, ensuring reliable power delivery.

(c) It is a circuit that houses a DSP microcontroller, which is responsible for managing the activation of the IGBT module based on feedback signals. This crucial part effectively administers the IGBT module's operation, ensuring precise control and regulation."

3. Full-bridge control

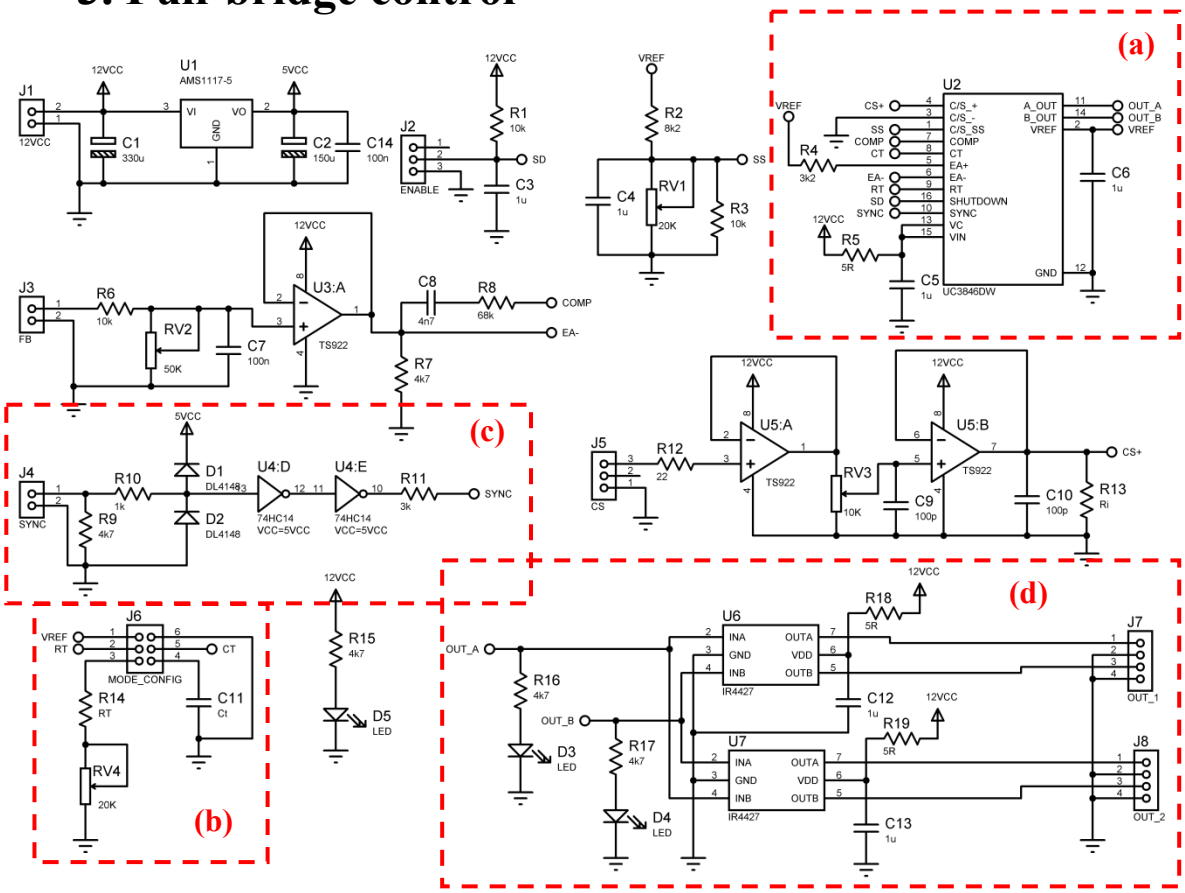

The inverter control system for the full H bridge utilizes the IC UC3846 as its core component (a). This system boasts an impressive synchronization capacity with external signals. However, specific configuration jumpers in the sub-circuit shown in the box (b) must be modified to achieve this synchronization. Once these changes are implemented, the coupling sub-circuit in the box (c) comes into action, connecting the impedances between the external signal and the pins of the UC3846. In addition, box (d) houses a set of MOSFET drivers responsible for current amplification at the IC output. These drivers ensure that the signals emitted experience minimal delays, thus maintaining their integrity. Finally, we have the external signal coupling circuits observed in other sub-circuits. These circuits play a crucial role in establishing communication between the IC and the feedback signals.

4. STM32F407ZGT6 industrial control board PLC industrial control board STM32 F4 development board Cortex-m4

The seller provided the picture.

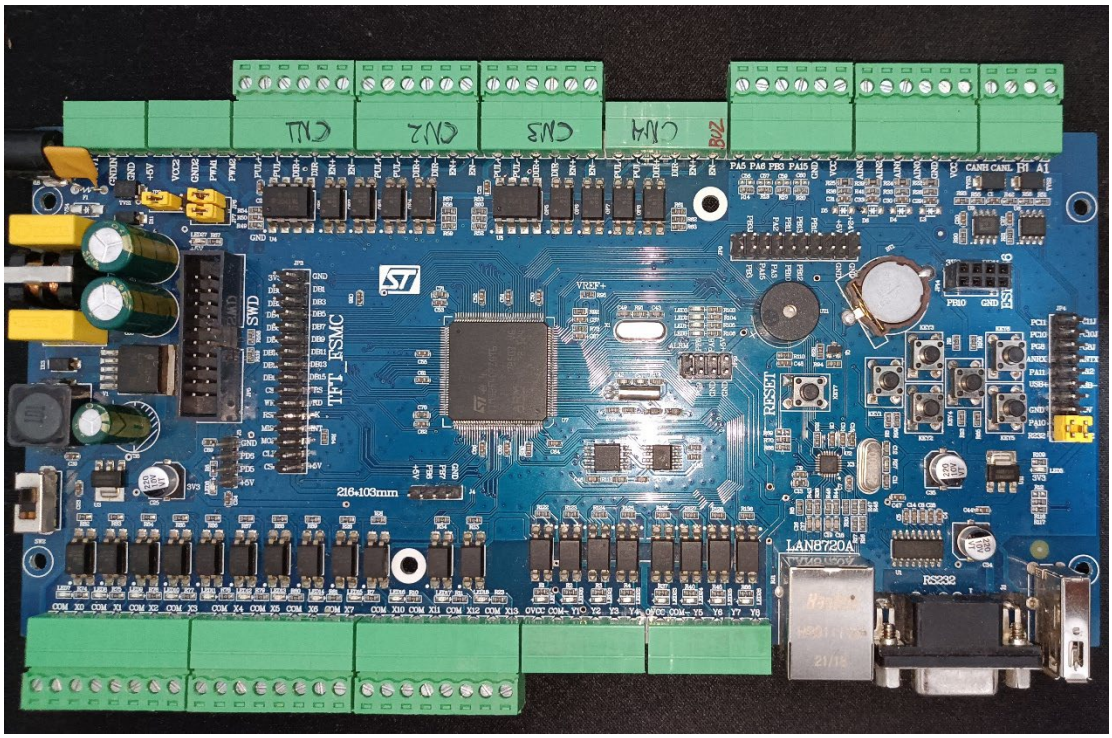

This development board is a ready industrial application for STM32F407ZGT6, a power 32 bits microcontroller. Its principal features are based on optocoupler IO pins. In addition, some bus modules were incorporated, such as ethernet, RS232, RS485, CAN, USB, and four fully stepper motor interfaces, which made a simple task to implement automatic control on timeline processes.